University of California
Santa Barbara

Optical trapping and single molecule measurement technologies for the investigation of biomolecular forces and motion

A dissertation submitted in partial satisfaction
of the requirements for the degree

Doctor of Philosophy
in
Mechanical Engineering

by

Jamianne C. Wilcox

Committee in charge:

Professor Megan T. Valentine, Chair
Professor Otger Campàs
Professor Omar A. Saleh
Professor Kimberly L. Foster

January 2018

The Dissertation of Jamianne C. Wilcox is approved.

Professor Otger Campàs

Professor Omar A. Saleh

Professor Kimberly L. Foster

Professor Megan T. Valentine, Committee Chair

December 2017

Optical trapping and single molecule measurement technologies for the investigation of biomolecular forces and motion

by

Jamianne C. Wilcox

To Doniese Wilcox for my earliest science training.

To Jim Wilcox for teaching me to question everything.

To Steven Brown for believing in me,
and for insisting that I believe in myself.

Acknowledgements

I am extremely grateful to the people who have made this thesis possible. Much appreciation is given to Professor Megan Valentine and Professor Otger Campàs for financial support and invaluable research guidance. I would also like to thank my other committee members, Professor Kimberly Foster and Professor Omar Saleh, for their helpful suggestions throughout my time at UCSB.

I am thankful for the National Science Foundation, which provided funding, and to the Materials Research Laboratory for the use of their Shared Equipment Facilities. The technical staff of Physik Instrumente and IntraAction helped us navigate the complexities of our optical trapping components.

I would like to thank Professor Stu Feinstein, who generously provided the use of his lab facilities, and Dr. Nikki LaPointe, who helped me with microtubule troubleshooting and all things biology.

My lab members provided exceptional support and advice. Dr. Dezhi Yu taught me how to pipette and make microtubules. Dr. Benjamin Lopez patiently trained me on the operation of his beautiful optical trap, and provided the EB1 experimental data for our diffusion studies. Dr. Bugra Kaytanli and Dr. Emmanouela Filippidi helped me to think critically about my work and see the big picture. Future Doctors Marcela Areyano, Aimal Khankhel, and Nick Zacchia provided emotional support, lab hijinks, and a sense of community. Dennis Huang assisted in gathering tensiometer data for our biomimetic droplets. The members of the Campàs group supplied infinite wisdom and an unstoppable groove. Adam Lucio helped me understand surface tension and microfluidics. Elijah Shelton, Payam Rowghanian, Alessandro Mongera, and Friedhelm Serwane were always willing to talk out physics and equipment problems. David Kealhofer shared and alleviated my LabVIEW woes. The members of the Saleh group always had helpful

suggestions on biophysics and instrumentation, and Dr. Bob Lansdorp shared his power spectrum wizardry.

I owe special thanks to Dave Bothman, Greg Dahlen, Bob Hanson, Paul Weakliem, and the MRL staff, who were a fountain of technological support and inspiration. The CNSI and ME staff were also superbly kind and helpful.

I am grateful for numerous other lovely people I met at UCSB, all of whom I do not have the space to name here, but without whose support I could not have completed this thesis.

Finally, I owe a huge debt of gratitude to my parents Jim and Doniese Wilcox, to all of my family for encouraging my curiosity and my love of science, and to Dr. Steven Brown for his unceasing love and support.

Curriculum Vitæ

Jamianne C. Wilcox

Education

2017	Ph.D. in Mechanical Engineering (Expected), University of California, Santa Barbara.
2012	Bachelor of Mechanical Engineering, University of Minnesota, Twin Cities.

Teaching

fall 2016	Course Designer and Instructor, School for Scientific Thought
fall 2016	Teaching Assistant, Computer Aided Design and Manufacturing
spring 2016	Teaching Assistant, Computer Aided Design and Manufacturing
fall 2014	Teaching Assistant, Molecular and Cellular Biomechanics
fall 2013	Teaching Assistant, Mechanical Engineering Design I
spring 2013	Teaching Assistant, Control Systems Design
winter 2013	Teaching Assistant, Control Systems Design
fall 2012	Teaching Assistant, Mechanical Engineering Design I

Outreach

2014	Volunteer, NanoDays
2016	Volunteer, Tech Trek

Leadership

2016	Founder, UCSB Education and Pedagogy Discussion Group
2015-2016	Member, The ME Graduate-Student-Invited Seminar Organizing Committee

Mentorship Trained and mentored undergraduate researchers throughout my time at UCSB including Tim Thomas, Kuang Wei, and Dennis Huang.

Awards

- Best Poster, *Duncan and Suzanne Mellichamp Poster Session*, Santa Barbara, CA (April 4, 2016)

Publications

- **Jamianne C. Wilcox, Benjamin J. Lopez, Otger Camps, and Megan T. Valentine,** "Improved calibration of the nonlinear regime of a single-beam gradient optical trap," *Opt. Lett.* **41**, 2386—2389 (2016)

Presentations

- **Jamianne C. Wilcox, Benjamin J. Lopez, Otger Camps, Megan T. Valentine,** Optical tweezers: Improved calibration method for the nonlinear range, *Duncan and Suzanne Mellichamp Poster Session*, Santa Barbara, CA (April 4, 2016)
- **Jamianne C. Wilcox, Benjamin J. Lopez, Otger Camps, Megan T. Valentine,** Improved Calibration Method for the Nonlinear Regime of a Single-Beam Optical Trap, *Biophysical Society 60th Annual Meeting*, Los Angeles, CA (March 1, 2016)
- **Jamianne C. Wilcox, Benjamin J. Lopez, Otger Camps, Megan T. Valentine,** Optical Tweezers: Using light to probe biological machinery, *UCSB International Year of Light Symposium*, Santa Barbara, CA, (October 8, 2015)
- **Jamianne C. Wilcox, Benjamin J. Lopez, Otger Camps, Megan T. Valentine,** "A new method for calibrating the nonlinear range of a single-beam optical trap", Proc. SPIE 9548, Optical Trapping and Optical Micromanipulation XII, 95480Y (August 28, 2015); doi:10.1117/12.2190397.

Abstract

Optical trapping and single molecule measurement technologies for the investigation of biomolecular forces and motion

by

Jamianne C. Wilcox

Intracellular transport along microtubules is a process critical to cell health, and one whose breakdown is associated with neurodegenerative disorders. In this thesis, we describe new technologies that will enable and improve investigations of multiple types of intracellular transport on microtubules.

Although the single molecule properties of many motor proteins have been well characterized, their behavior when transporting biological cargoes as a group of motors is still not well understood due to measurement challenges, as well as a lack of a model system for systematically studying collective motor behavior in vitro. In this work, we discuss the construction of an optical trapping setup capable of applying and measuring forces with 2 pN accuracy. We report our design of a biomimetic droplet system that reproduces the relevant surface properties of biological cargoes while allowing the droplets to be used as optical trapping probes. We also present a new optical trapping calibration technique that allows experimenters to utilize the nonlinear range of the trapping force profile, and thereby measure the high forces developed by groups of motor proteins.

Finally, we investigate the distributions of diffusion coefficients found for Microtubule Associated Proteins diffusing on microtubules through Monte Carlo simulations, and examine the subtleties of interpreting and reporting single molecule diffusion data.

Contents

Chapter 1

Introduction

1.1 Background

1.1.1 Molecular Motor Transport in Cells

Cells are busy, crowded places[1], with cargoes of filaments, organelles, vesicles, and more, being shuttled back and forth constantly. A critical segment of this transport is completed using a class of molecules called motor proteins, which have the ability to apply force and create motion. These proteins attach to cargo surfaces either directly or through trans-membrane proteins[2] [3] [4], and take discrete steps along cytoskeletal filaments to produce directed motion through the cell.

The breakdown of intracellular transport in neurons has been implicated in several neurodegenerative disorders, including Alzheimer's disease[5] [6] [7]]. A better understanding of the processes involved in transport would facilitate the development of diagnostic and treatment tools for these disorders[8] [9].

1.1.2 Kinesins

Kinesins are a family of motor proteins that step processively along microtubules, pulling cargo from one end of the cell to another. They are the truckers of the cellular world, and can transport many different types of cargo, including vesicles, organelles, and in particular, neurotransmitters and neruofilaments in neurons[7]. In a typical neuron, microtubules radiate out from the cell nucleus and continue along the axon, forming a highway along which cargoes can be carried[10]. Because neurons are so long, an efficient mechanism for directed transport is critical to reliably move cargoes all the way along the axon to the axon terminal.

Thanks to modern single molecule techniques, much is known about the properties of single kinesins[11] [12] [13] [14] [15] [16] [17] [18]. Kinesin (specifically Kinesin-1, or conventional kinesin [19]) was first identified by Vale et al. in 1985[20]. Aptly named after the Greek word *kinein* (to move), kinesin has two motor domains which bind to and take discrete, 8-nm steps along microtubules[21] in a hand-over-hand motion[12], and is notable for its high processivity, taking on the order of 100 steps before unbinding from its microtubule track[22] [21]. Each motor domain has a binding site for ATP, which when bound produces a conformational change that results in a step[22]. Kinesins can bind to various cargoes including neurofilaments, vesicles, organelles, and RNA granules, either directly or using adaptor proteins[7]. When not bound to a cargo, kinesin folds over onto itself and an inhibitory interaction between the tail domain and motor domains prevents ATP from binding, immobilizing the motor[23] [24]. This folding enhances the energy efficiency of kinesin transport by preventing useless stepping. A single Kinesin-1 motor can apply a maximum force of about 6 pN [25], and travels at a speed of about 800 nm/s under negligible loads and ATP saturation[14]. Although many different motor proteins are involved in intracellular transport, we have focused our investigations on Kinesin-1

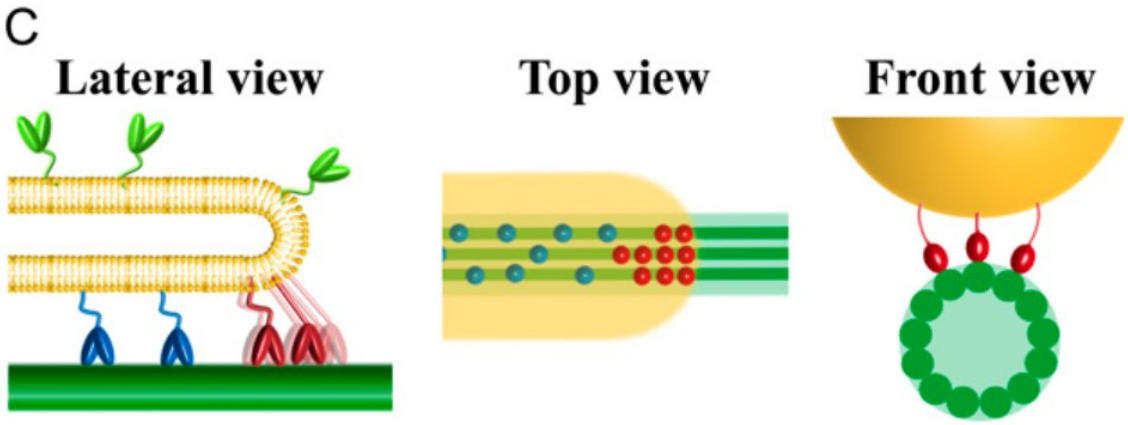

Figure 1.1: Campàs et al. 2008[26]. Lateral view: multiple kinesins pulling membrane tubes do not share the force of pulling equally; only the leading motors transmit a force to the tube while motors further back only cause the lipids that they are attached to slide within the 2D membrane. Top view: Campàs et al. determined that about nine motors on three protofilaments could share the force of pulling the tube. Front view: the length and flexibility of the motors, as well as the curvature of the microtubule, determine the number of protofilaments from which kinesins can pull. Reprinted from Biophysical Journal, Vol. 94 Issue 12, Otger Campàs, Cécile Leduc, Patricia Bassereau, Jean-François Joanny, and Jacques Prost, Coordination of Kinesin Motors Pulling on Fluid Membranes, 5009-5017, Copyright 2008, with permission from Elsevier.

because of its prevalence in the literature and its usefulness as a model system.

1.1.3 Collective Motor Transport

Although much is known about single motor properties, the details of how multiple motors work together to move cargo efficiently remain unclear. A better understanding of how motors work in groups will be key to piecing together a full picture of intracellular transport.

It has long been speculated that multiple motors engage in the transport of lipid cargoes in vitro, and evidence for this is slowly accumulating. In motor-assisted membrane tube formation, multiple motors are necessary to supply the ∼30 pN tube extraction force

[26] [27]. Sims and Xie measured kinesin forces on endogenous lipid droplets in human lung cancer cells, and found that these forces exceeded the single kinesin maximum force of 6 pN[28]. Increased motor number is known to increase cargo processivity in vitro [29] [30]. Shubeita et al. found that multiple motors engaged on lipid droplets in drosophila embryos, but did not see enhancement of either travel distances nor velocities due to higher motor number[31]; they provide a possible explanation for this discrepancy from in vitro studies by proposing the existence of a switch mechanism that could actively terminate the motor run in vivo[32]. In vivo obstacles or drag forces could also play a role in these differences.

A great majority of in vitro collective kinesin studies have been performed using cargoes such as silica or polystyrene beads[33] [11] [15] [12]. We call these cargoes "solid-surface" cargoes, or "solid cargoes" for short, for the simple reason that their surfaces are a single solid, continuous structure. In contrast, many biological cargoes, such as organelles and vesicles, are encased in a lipid membrane. We refer to these cargoes as "fluid-surface cargoes" (or "fluid cargoes") because the lipids comprise a two-dimensional fluid on the surface of the cargo.

The surface properties of fluid-surface cargoes differ from those of solid-surface cargoes in an important way. Solid cargoes form a single rigid body and can support in-plane shear—each additional kinesin that attaches to the cargo can transmit a force to the cargo as a whole, and can share the load of moving the cargo. In contrast, the lipids in the membranes of fluid cargoes are not rigidly attached to each other, but instead can diffuse freely within the plane of the membrane[34]. It takes very little energy to slide a lipid past its neighbors, but it does require great energy to pull a lipid out of the membrane[35]; for this reason, the membrane can resist out-of-plane forces, but has very little resistance to in-plane shear. As the left panel of Figure 1.1 shows, only the kinesins at the leading edge of the cargo can apply a force perpendicular to the lipid membrane

and transmit their force to the cargo body. Kinesins pulling on lipids further behind will simply slide those lipids along within the membrane, and will not contribute to the overall force on the cargo. We predict that this puts an upper limit on the number of kinesins that can share the force of pulling a fluid cargo.

A few studies have been made regarding the behavior of fluid cargoes. In 2006, Campàs et al. theoretically described collective transport of motors pulling fluid cargoes with interactions between motors and unequal force sharing[36]. They calculated and simulated force-velocity curves for the motors and found that they varied significantly from the curves found in the theoretical description of motors pulling solid cargoes described by Klumpp et al. in 2005[37]. Campàs et al. performed another study in 2008 investigating the mechanics of membrane tube formation by kinesins through experiments and simulations[26]. They deduced that up to nine motors spread over three microtubule "lanes" (protofilaments) could share the force of pulling the tube (Figure 1.1.)

In addition to cargo studies, other aspects of collective kinesin transport have been investigated. Some observations have been made on how motors behave at the intersections of two filament tracks; Vershinin et al. found the intriguing result that adding a small amount of the microtubule-associated protein (MAP) tau significantly increased the frequency of kinesin switching tracks at microtuble-microtubule intersections without noticeable microtubule deformations, implying that tau prevents kinesins from engaging in a "tug of war" at intersections[29]. Ross et al. discovered that multiple kinesins pulling on cargoes tend to switch tracks more frequently than single motors[38].

1.1.4 Diffusive Transport on Microtubules

Further discoveries have been made about the nature of MAPs themselves: most notably that some proteins (including tau), which were once thought to be stationary

road blocks on microtubules, have recently been shown to diffuse along microtubules[39]. In 2014, McVicker et al. reported that tau proteins appear as both stationary and diffusing populations on taxol- and GMPCPP-stabilized microtubules, and can transition from one state to the other, although the proportion of states depended strongly on both the microtubule structure tau isoform. Lopez et al. investigated the dynamics of EB1 molecules diffusing on microtubules in 2015[40]. Diffusion of molecules on microtubules introduces a new possible mode of intracellular transport, as well as complicates the picture of MAPs as road blocks for molecular motor transport.

1.2 Technological Advancements are Needed for Transport Studies

Although collective motor behavior and molecular diffusion on microtubules offer exciting new perspectives on intracellular transport, experimental investigations remain challenging. In Sections 1.2.1, 1.2.2, and 1.2.3, we outline three major technologies used to study molecular motors and MAPs, and we discuss their advantages as well as limitations for investigating motor protein and MAP behaviors.

1.2.1 Total Internal Reflection Fluorescence Microscopy

Total Internal Reflection Fluorescence (TIRF) microscopy is a technique in which fluorescence excitation is confined to a thin region near the glass-water interface in order to illuminate only a localized region of a sample. To achieve this, a laser is aimed at a glancing angle, above the critical angle for total internal reflection, onto a glass coverslip such that the laser light totally internally reflects within the thin glass layer. This generates an evanescent field constrained close to the surface of the glass, which

will excite any labeled particles on or in the near vicinity of the surface[41]. The primary advantage of the confined field is that the evanescent field decays exponentially from the surface so any particles suspended or diffusing above the glass surface will not be excited, and thus will remain dark. This minimizes the background fluorescence signal and reduces the likelihood of photobleaching molecules that are not actively engaged at the glass surface (see Section 3.5 for descriptions of sample chambers used in typical experiments). For a typical TIRF experiment, the penetration depth, which is defined as the decay length of the exponentially decaying light field intensity, is in the range of 50-100 nm. Thus, TIRF is especially advantageous for studying microtubules (and other surface-immobilized filaments) and their associated proteins because the microtubules' size places them and any attached proteins within the evanescent excitation field when they are adhered to the glass surface.

Electron-Multiplying Charge-Coupled Device (EMCCD) cameras are typically used in single-molecule studies for their superior ability to detect single photon events[42]. Though frame rates of 500 frames per second (fps) are possible with severely cropped fields of view[43], frame rates on the order of 20 to 50 fps are more typical. This poses a challenge for observing the most minute motions of molecules diffusing on microtubules. Photobleaching and blinking of fluorophores add uncertainty to longer measurements of molecule trajectories. The high technological performance requirements of these experiments limits the amount of data that can be obtained, making interpretation of the results difficult.

1.2.2 Optical Trapping

Optical traps, or optical tweezers, are a tool which act as a tractor beam for small particles, allowing them to be grabbed, held, and moved in three dimensions. They have been

used for a variety of applications, including measuring forces, positions, and velocities[25] [14], applying constant forces or displacements[14] [44], stretching molecules[45], or simply manipulating particles in space[46].

An optical trap is formed by tightly focusing a high-powered laser beam, typically with a high numerical aperture objective lens, to produce a large intensity gradient[47]. If a particle has a higher index of refraction than the surrounding media, and if the particle's size is close to the wavelength of the laser light, then the momentum transfer by photons to the particle will result in a restoring force toward the laser focal point. This phenomenon was first demonstrated by Arthur Ashkin in 1986[48]. Optical tweezers are ideally suited for small molecule experiments because of their superior spatial and temporal resolution, and the ability to couple the force manipulation optics with high-resolution microscopy.

Despite their flexibility, optical traps are just starting to be applied to studies of collective kinesin transport, due to technological limitations. Optical traps are frequently claimed to be able to apply up to 100 pN of force easily [47] [49] [50] [51], but this benchmark is not so straightforward to achieve in practice. In section 1.2.3 we describe situations in which optical trapping forces on the order of 100 pN are necessary for the investigation of collective kinesin behavior, and in Section 4.2 we describe a new method for calibrating the nonlinear force range of an optical trap in order to measure these high forces.

1.2.3 Use of Optically Trapped Particles for Molecular Motor Research

A ubiquitous way of studying the properties of molecular motors involves using an optical trap on a micron-sized particle, such as a glass or polystyrene bead, that has

been coated with motors (see Figure 1.2). The bead is trapped and moved close to a sample chamber surface that has been lined with microtubules, so that motors attach and start stepping. In a common scheme, the optical trap, which behaves as a spring, is held at a fixed position, and the restoring force applied to the bead increases the farther the motors pull their bead cargo from the trap center. The motors continue to step until their pulling force balances the spring force, causing the particle to stop or stall when equilibrium is reached (this force is known as the motors' stall force). The trap is calibrated beforehand, so that the forces corresponding to each displacement are known, and the particle's displacement is measured with an additional laser beam (see sections 2.3.5 and 2.3.6 for an overview of how these measurements and calibrations are accomplished.)

Despite the interest in understanding collective motor behavior on biological cargoes, no model system has been produced for the systematic study of collective motor behavior in vitro. Polystyrene and glass beads do not capture the relevant surface properties of many biological cargoes, including lipid vesicles and organelles, which are encased in a lipid bilayer membrane. As we described in Section 1.1.3, these fluid cargo surfaces are distinctly different from the surfaces of solid beads.

By using optical trapping methods to measure the forces and velocities of the kinesin system with both solid and fluid cargoes, the two cargo types could be compared to confirm whether the mechanics are indeed different, and how they deviate. We predict that the two cargoes would approximately display the force behavior shown in Figure 1.3, in which solid cargoes can support much higher forces than fluid cargoes because of the kinesins' ability to transmit forces to the entire solid body from any position along the microtubule. The stall forces of the kinesins can be found by measuring how far the kinesins can pull each cargo type out of the trap.

In order to make such a comparison possible, an appropriate model system for fluid

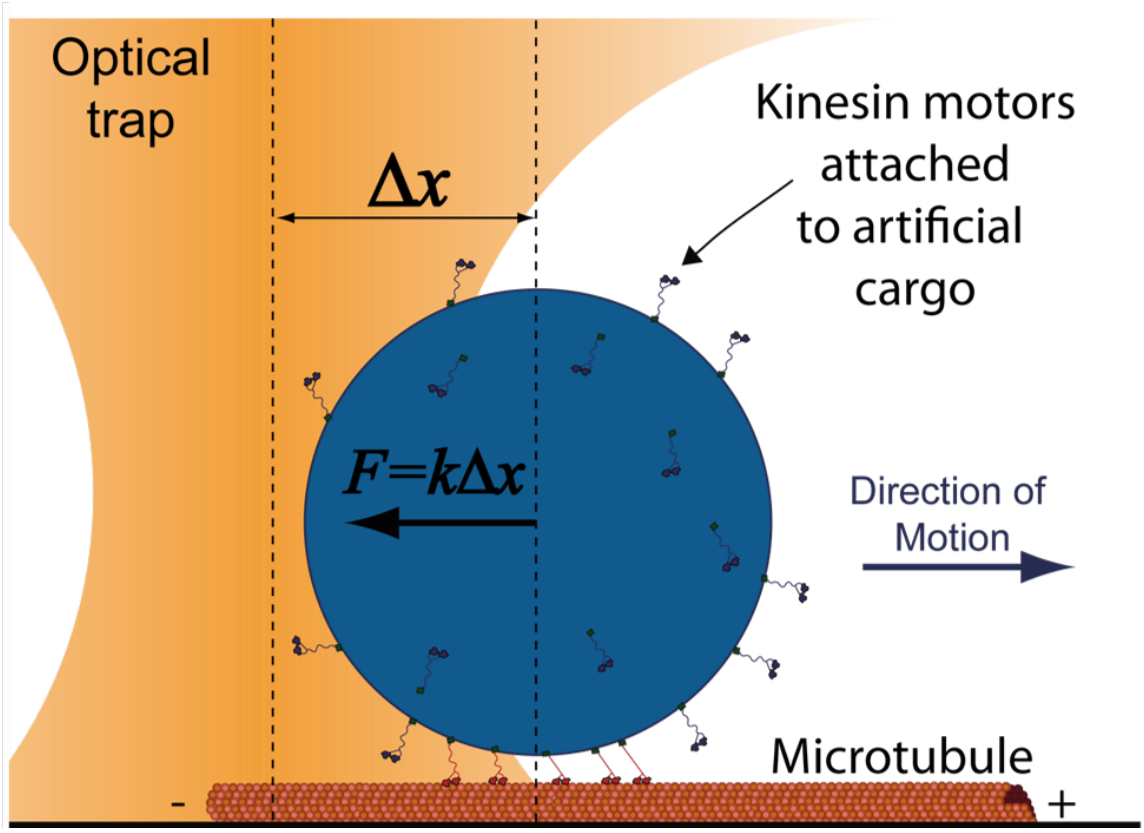

Figure 1.2: *In vitro* experiment to measure the forces produced by multiple kinesins. Microtubules are applied to the surface of a sample chamber and kinesin-coated cargoes are added to the chamber. The cargo is trapped and brought close to the microtubules, so that the kinesins may attach and begin to step. The displacement of the trapped cargo from the center of the calibrated optical tweezers reveals the force applied to the cargo by the kinesins.

cargoes would need to be created. In addition, the cumulative forces that can be developed by groups of kinesins pose a significant challenge to typical optical trapping force capabilities. Higher forces than are typically applied using optical traps would be needed to detect the force differential between the predicted ∼30 pN force of kinesins on a fluid cargo and the >60 pN force on a rigid cargo. Developing solutions to these two problems will be a major focus of this thesis.

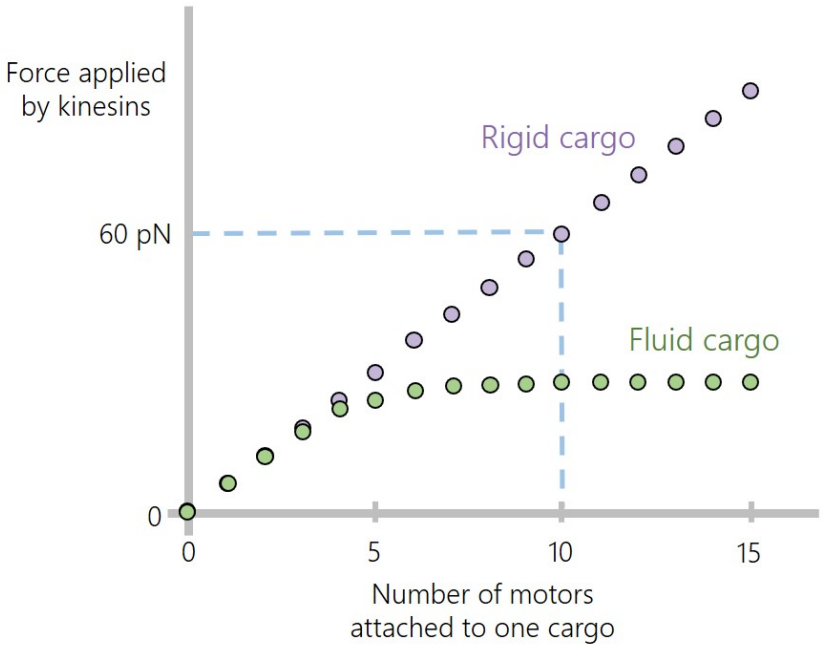

Figure 1.3: Hypothesized stall forces for groups of kinesins on solid and fluid cargoes: For a solid cargo, each added kinesin can pull on the cargo with a force of up to 6 pN. For fluid cargoes, only the leading motors can transmit a force to the cargo body. Campàs et al. determined that about 9 motors can share the force of pulling on a fluid cargo (but they do not share the force equally.) This plot is an approximate prediction of the difference between solid and fluid cargoes that we expect to measure in our experiments.

1.3 Thesis Overview

In Chapter 2, I will discuss our optical trapping and TIRF microscopy setup, and the technological changes and additions we made to expand its experimental capabilities. In Chapter 3, I describe biomimetic cargoes that we designed as a model system for the future study of collective motor transport. Chapter 4 describes a new method that we developed for calibrating the nonlinear range of an optical trap that requires fewer assumptions and technological requirements than any previous nonlinear calibration method, and also discusses an expansion of that method that allows it to be applied more easily to in vivo studies of motor proteins. In Chapter 5 I outline our findings

for improving the interpretation of single molecule diffusion studies on microtubules. I conclude with Chapter 6 in which I discuss future directions for this work.

Chapter 2

Optical Trapping and Microscopy Technology Development

2.1 Introduction

There were many obstacles to overcome in order to develop the technology necessary to perform these experiments. We added hardware, performed calibrations, and wrote software. This chapter describes our optical trapping and microscopy setups, the techniques we used in measurements and calibrations, and the most critical technology and techniques that we developed to allow for future explorations of collective motor protein behavior.

2.2 Optical Trap Design

2.2.1 Overview

Our optical trapping setup includes numerous optical, mechanical, and electronic components that together form a unified measurement system. We can manipulate particles

with nm precision, measure particle motion with nm accuracy, and apply and measure forces with 2 pN accuracy using our optical trapping and detection lasers. Our two piezo stages allow us to control the motion of our sample chamber with two levels of speed and precision. Our high-resolution, high-precision stage has a maximum speed of 350 nm/s with nm precision over a travel range of 100 nm in the horizontal x and y planes and 20 nm along the vertical axis (z-direction, along the optical axis of the microscope.) A second, long travel distance substage move at higher speeds, up to 100 mm/s with 300 nm precision over a total travel range of 20 mm. For imaging of samples, we are able to perform both brightfield and Total Internal Reflection microscopy measurements, and we have two laser colors for fluorescence excitation. A majority of our components are controllable through custom LabVIEW GUIs. Figure 2.1 shows the optical equipment of our setup.

2.3 Microscopy Design

2.3.1 Total Internal Reflection Fluorescence Microscopy

We included a blue (488 nm) and a green (532 nm) laser in our microscopy setup for the application of Total Internal Reflection Fluorescence (TIRF) microscopy. Each laser has its own telescoping lens pair for adjusting the beam widths. The beams are focused at the back focal plane of our Nikon high numerical aperture objective lens, and they strike the lens at an off-center position. This allows a collimated beam to enter the sample chamber at an angle above the critical angle for total internal reflection.

Photons released by fluorophores excited by TIRF exit the sample through the objective lens, and are directed onto an Electron-Multiplying Charge-Coupled Device (EMCCD) camera. A holographic notch filter and a 745 nm edge filter from Semrock are

used to block trapping laser and detection laser light from entering the cameras. This is critical for protecting the sensitive cameras from the high intensity light of the lasers.

In order to view both microtubules and fluorescent cargoes in the same fluorescence image, we had to hand tune the emission level of the cargoes. Commercial fluorescent particles are too bright and wash out the microtubules, so we instead used biotinylated particles which we mixed with an admixture of fluorescent and unlabeled streptavidin. We found that a 1:1000 ratio of fluorescent to unlabeled streptavidin produced an appropriate level of fluorescence to be able to view both microtubules and particles in the same image.

2.3.2 Brightfield Microscopy

We used a mercury arc lamp to provide the illumination source for brightfield imaging. The lamp light enters the sample from the condenser lens, and exits through the objective, and is then directed onto a Charge-Coupled Device (CCD) from Point Grey Research. An electronically controlled flipper mirror switches the optics pathway between the CCD and EMCCD cameras.

2.3.3 Trapping Laser Pathway

Our single-beam gradient optical trap is formed using a 1064 nm, 5 W maximum power Nd:YAG laser from Spectra-Physics. An adjustable half wave plate and beam splitting cube allow a portion of the laser to be diverted into a beam dump, which facilitates alignment and low-power experiments. The beam is directed through an IntraAction Acousto-Optic Deflector (AOD), which is placed in a plane conjucate to the objective lens back focal plane (BFP). The AOD consists of two crystals to which controlled sound waves are applied by a PCI-based frequency generating card. The vibrations set up

phonon waves within the crystals that allow them to behave as a diffraction grating for incoming photons, with an effective grating spacing that can be dynamically controlled by the frequency of the waves, and a conversion efficiency that is dictated by the acoustic wave amplitude. Since the AOD is placed in a plane conjugate to the objective lens BFP, angular deflections of the trapping beam at the AOD are transformed into pure displacements, or position deflections, in the sample plane, or in the plane of the trap focus.

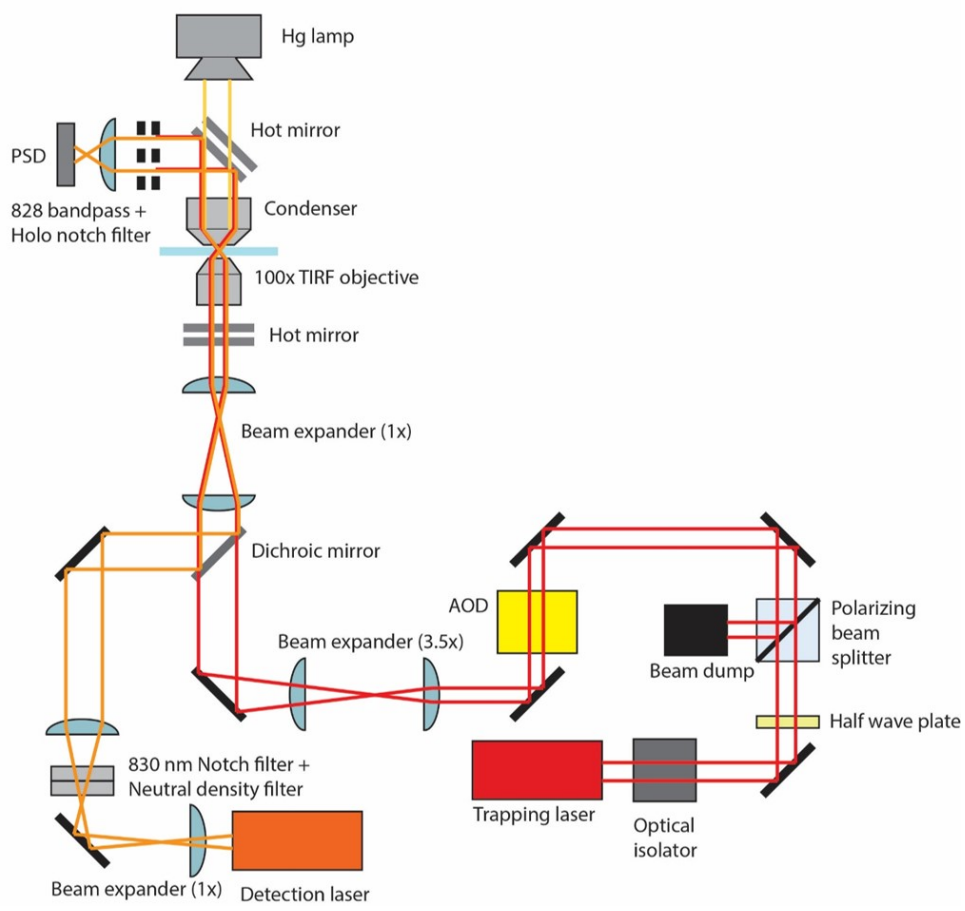

Figure 2.1: Optical trapping and detection laser pathways for our optical trapping setup.

After exiting the AOD, the laser beam is passed through one pair of beam expanding lenses that adjusts the beam waist size to ensure that the beam slightly overfills the back

of the objective lens. A second pair of lenses forms a 1:1 telescope that is used to image the AOD position onto the BFP of the objective lens. The high NA objective (NA = 1.49, Nikon TIRF lens) tightly focuses the beam in the sample chamber, forming the large intensity gradient that produces the restoring force region of the optical trap.

After the trapping beam leaves the sample, it is blocked from further travel with a holographic notch filter. An electronic shutter is also included slightly upstream to the objective so that the experimenter can quickly turn the trap off and on in the sample chamber.

2.3.4 Positioning and Motion Control

We first constructed our optical trapping setup with an electronic piezo stage with a closed loop range of 100 x 100 x 20 µm (P-517.3CD stage with E-725.3CD Digital Multi-Channel Piezo Controller) secured on top of a mechanical substage with a range of 50 x 50 mm (Märzhäuser Wetzlar MT 50 x 50), which was movable in two dimensions via manual micrometer screws.

To improve our range of motion, we replaced the manual substage with a PILine piezo stage (M-686 PILine stage with C-867.260 controller), which has both a larger range (25 x 25 mm) and higher velocities (up to 100 mm/s).

The smaller stage is used to obtain calibration factors for measuring particle motion in the trap (see Section 2.3.5), and both stages can be utilized to calibrate trapping forces (Section 2.3.6).

2.3.5 Measuring the Motion of Trapped Particles

Particle position measurements are accomplished using a separate, 100 mW, 830 nm laser from Melles Griot and a Position Sensitive Detector (PSD) from Pacific Silicon

Sensors Inc. This detection laser travels through one dedicated beam expanding lens pair, and shares the second beam expanding lens pair of the trapping laser. From there it is injected into the objective lens, where it has been aligned to be coaxial with the trapping laser, with a focal distance that is slightly displaced from the focus of the trapping laser to ensure that the detection laser is well-centered on the trapped particle, which tends to sit slightly downstream of the trapping laser focus due to the force balance between the radiation pressure and gradient force from the beam. We used a neutral density filter to reduce the detection laser power to about 30 W–a level which created appropriately sized voltage signals from the PSD.

After leaving the sample chamber and passing through the condenser lens, the detection laser terminates on the PSD. Inside the sample chamber, the detection laser focus lines up with the center of an undeflected, trapped particle. The detection laser beam is refracted by the particle, but is refracted symmetrically when the particle is at the exact center of the trap. When the particle is displaced from the center of the trap, for example from thermal forces or the force of a microtubule-attached kinesin pulling on the particle, the detection beam refracts more to one side, which manifests on the PSD as a light spot that has moved off-center. The PSD converts the asymmetry of the light spot into a voltage signal, which is proportional to the displacement of the particle from the trap center.

The PSD outputs two signals for each of the two dimensions of the plane: one 'sum' signal which reflects the total intensity of light on the PSD, and one 'differential' signal, which is proportional to the amount the light spot is displaced to one side. These signals are fed into an electronics box which performs analog operations to normalize the differential signals by the sum signals. The resulting 'normalized' signals are sent through a Krohn-Hite programmable filter to remove high frequency noise, and the filtered signals are read with a National Instruments Data Acquisition device.

In order to map the voltages of the PSD to particle displacements in nm, three calibration routines are performed. First, we attach polystyrene beads onto a sample chamber surface and use the piezo stage to move the entire surface, including the attached beads, at a constant velocity. The positions of the particles are tracked through LabVIEW using the CCD camera, and the commanded stage positions (in nm) are plotted against the measured particle positions (in pixels, px). The slope of this plotted line gives us a nm/px conversion factor. For the next calibration, we trap a particle using the optical tweezers and scan the AOD over a range of frequencies (in MHz) to move the trapped particle through a range of positions in the sample plane. These particles are also tracked using the CCD camera, allowing us to obtain a px/MHz calibration factor from the slope of AOD frequency vs. camera pixels plot. The ratio of these two calibration constants provide a conversion between the MHz frequency that drives the AODs and the translated distance of a trapped bead within the sample plane. These calibration factors remain satisfactorily constant as long as the optical pathways are not changed, and the calibration constants were measured to be close enough in value in the x and y directions to be considered isotropic.

Finally, we trap a particle and use the AOD to raster scan the trapped particle over the stationary focal spot of the detection laser. We set the AOD frequencies to be applied during the scan, and measure the resulting PSD voltage outputs that are produced as the moving bead transits through the detection laser spot. Within a particle displacement radius of about 300 nm from the detection laser center, the voltage response to particle displacement is linear. A LabVIEW algorithm calculates separate conversion factors for the x and y directions of the image plane, with units of V/nm. These calibration factors can change somewhat with each new particle due to variations in bead size or shape, and must be remeasured whenever a new particle is trapped to ensure the most accurate calibrations and results.

By combining these three calibration factors, we produce a single nm/V calibration factor that we use to map PSD voltages to particle displacements in nm.

2.3.6 Calibrating Trap Forces

There are several ways in which the optical trapping forces can be calibrated. By force calibration, we refer to the mapping of the force vs. particle displacement curve, so that we can relate the measurement of a particle's displacement from the trap center to a particular restoring force applied by the optical trap. All of the calibration methods listed in this section are described in detail in Chapter 4.

For a radius of around 100 nm from its focus, the trap acts as a linear spring. In the regions beyond this radius, however, the trap stiffens and has a nonlinear force vs. displacement curve.

There are three main methods used to calibrate the linear region of the force curve[47]. In the Equipartition Method, a trapped particle's displacements are recorded using the detection laser and PSD while the particle fluctuates under thermal forces near the center of the trap. By modeling the trap as a harmonic well, the magnitude of these fluctuations can be related to the linear stiffness. In the Power Spectrum method, the same data from the Equipartition Method are used to plot a power spectrum, and the stiffness is extracted as a Lorentzian fit parameter. In the Stokes' Drag Method, the piezo stage is used to move the sample chamber at a controlled, constant velocity, and drags the surrounding fluid past a trapped particle. Because the flow is laminar, the drag force is proportional to the stage velocity and a force vs. displacement curve can be built by moving the stage at a variety of constant velocities and measuring the resulting particle displacements; the slope of the line is proportional to the linear stiffness. See section 4.1.1 for a detailed description of these calibration methods.

To calibrate the nonlinear range of the trap, we developed a new method in which we combine the Equipartition and Stokes' Drag Methods, which is described in Section 4.2. Although the Stokes' Drag Method can theoretically be used to calibrate the nonlinear region as well, this is rarely done due to challenges discussed in Section 4.1.2. Many traditional studies also use the Stokes' Drag Method to determine the displacement range over which the linear stiffness is valid. High-velocity stages are particularly useful for these calibration methods.

2.4 Hardware Modifications

2.4.1 Improvements in Signal Processing to Allow Collection of High Frequency Particle Fluctuation Data

In Chapter 4, we describe two approaches which we compared for obtaining optical trap stiffnesses: one established method and one new method. Both methods involve moving the piezo stage at a constant velocity so that the fluid in the sample chamber is dragged past a trapped particle, applying a constant drag force to the particle and displacing it by a fixed amount from the center of the trap. The drag force is calculated from the drag coefficient of the fluid-particle system and the known stage velocity, and plotted against the average displacement of the particle under constant force. This method is typically called the 'Stokes' Drag' method. Although it is not trivial to calculate the drag coefficient due to (often unknown) variations in particle size, and the presence of a bounding wall at the coverslip surface, this approach can be effective, and moreover, can provide information about the nonlinear regimes of the trapping potential, which are not accessible using the thermal motion of a trapped particle only.

The stiffnesses can alternatively be found from the variance of a histogram of the

positions of the displaced particle (which fluctuates due to thermal forces). This so-called 'Fluctuations' method has the advantage that the experimenter does not need to know the drag coefficient, but requires that the experimenter obtain a high signal to noise ratio when measuring particle fluctuations, and requires the accurate measurement of high-frequency position fluctuations. We can differentiate the force curve found with the Stokes' Drag Method to obtain a plot of stiffness vs. displacement with which to compare to our stiffnesses found using our Fluctuations Method, which is presented in detail in Section 4.2.

As we were testing the new method for measuring the nonlinear range of the optical trap, we discovered that the trap stiffnesses calculated using the Stokes' Drag method did not match with the stiffnesses calculated from the Fluctuations method, as shown in Figure 2.2. We hypothesized that this mismatch might be caused by aliasing, a phenomenon where high frequencies are mistaken for low frequencies when the sampling rate is too low; the power spectrum's higher frequency values get folded back into the lower frequencies because it is only possible to correctly identify frequencies up to half the sampling rate (the Nyquist frequency). To definitively test whether aliasing was the cause of our problem, we inserted a simple RC filter (Figure 2.3 into our signal pathway (see Figure 2.4).

First, we used a 10 nF capacitor and a 4 kOhm resistor to set the RC filter's corner frequency to 4 Hz, then measured the background noise produced by sending the detection laser through a sample chamber filled with only water, at various sampling rates (Figure 2.5). We chose to set the rolloff frequency to 40% of the sampling rate, in order to start the rolloff a little bit below the Nyquist frequency, as a safety margin to ensure that the high frequency noise would be sufficiently attenuated. Including a safety margin is a common practice when using RC filters, because the rolloff slope is not as steep as in commercial filters. In Figure 2.5, the power spectra measured at sampling rates

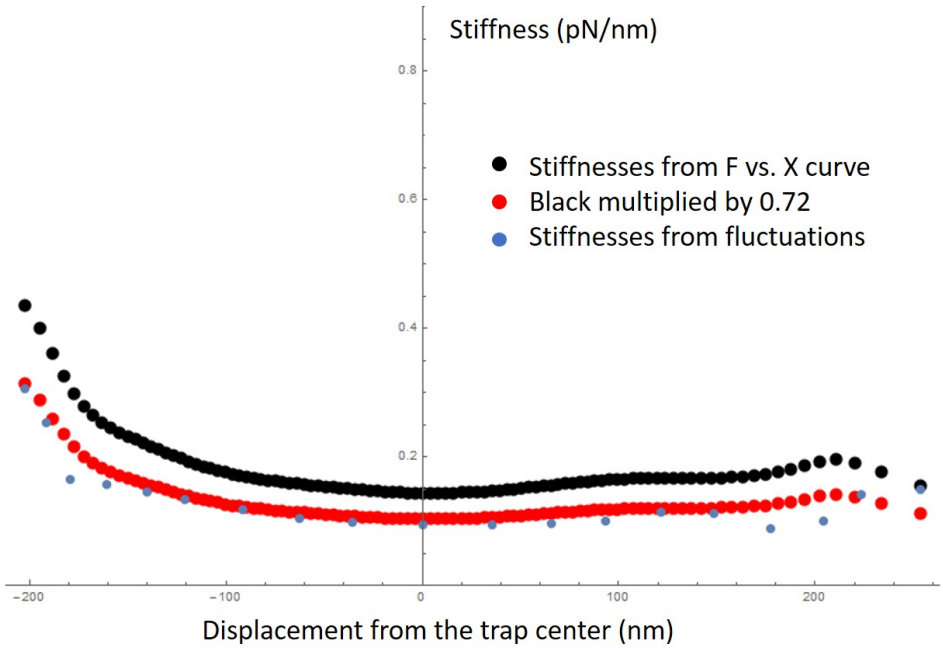

Figure 2.2: Stiffnesses calculated using two different measurement methods. In the Stokes' Drag method, the force vs. average particle displacement data is differentiated to obtain stiffnesses (black). In the Fluctuations method, the variance of a histogram of displaced particle positions (blue). The stiffnesses obtained from the two methods did not match up, but appeared to be proportionally related.

above the corner frequency showed the characteristic shape of the filter itself (Figure 2.6), with its characteristic rolloff. The power spectra sampled below the corner frequency in Figure 2.5 began to increase in magnitude, suggesting that the frequencies higher than the sampling rate but lower than the corner frequency were getting folded back into the measurement, misidentified as lower frequencies.

Next, we split the signal and fed one cable into the filter and the other cable fed directly to the NI Data Acquisition box (DAQ). We measured both the filtered and unfiltered versions of the same signal simultaneously so that we could directly compare the two (Figures 2.7 and 2.8). Measurements of these signals at various sampling rates supported the aliasing theory, showing that as we lowered the sampling rate the unfiltered power spectra magnitudes increased (Figure 2.7). We used the same 10 nF capacitor

with resistors of 40, 400, 4k, 40k, and 400k Ohm to produce characteristic frequencies of 400k, 40k, 4k, 400, and 40 Hz, respectively. The filtered power spectra, however, remained nearly constant, showing that the filter was preventing the higher frequencies from significantly adding to the power spectra at lower frequencies, by attenuating the higher frequency signals.

These investigations confirmed the presence of aliasing within our signals. We were then able to solve the problem by installing a Krohn-Hite Model 3940 Programmable Filter with a 24 dB/decade attenuation rate, which can attenuate signals much more sharply than an RC filter. We typically used the filter's 4-pole Butterworth setting with the rolloff frequency set to 50 kHz, while sampling at 100 kHz for our experiments. After adding the filter, the stiffnesses measured using the two techniques matched (Figure 2.9), because our measurements were no longer being altered by aliasing. This allowed us to continue with the verification of the Fluctuations Method as described in Chapter4.

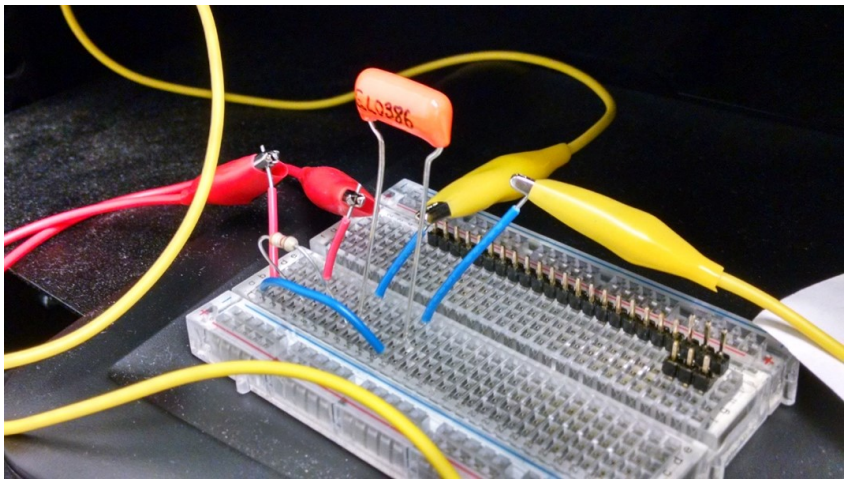

Figure 2.3: Image of our homemade RC filter. The corner frequency of the filter was adjusted by swapping out different resistors. A 10 nF capacitor was used. Resistors of 40, 400, 4k, 40k, and 400k Ohms were used to produce characteristic frequencies of 400k, 40k, 4k, 400, and 40 Hz, respectively.

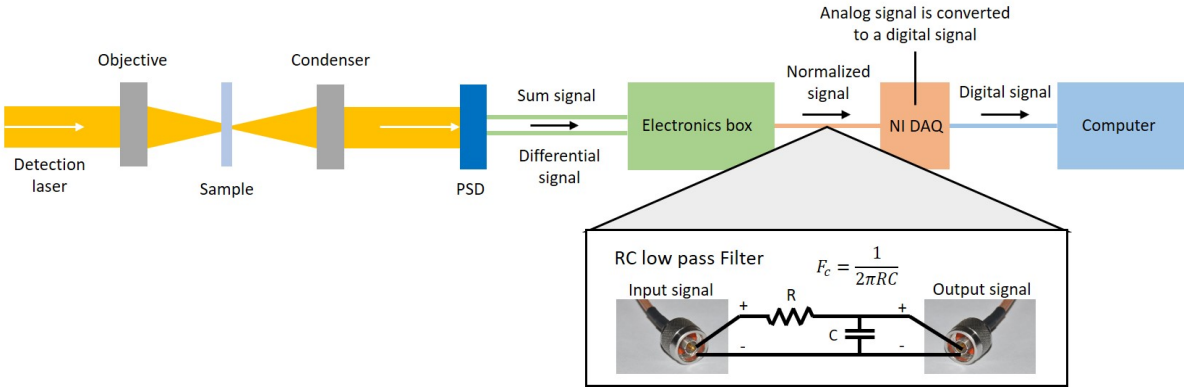

Figure 2.4: Flow diagram of the detection laser signal pathway. Light from the detection laser (left, yellow) passes through the microscope objective and is focused onto the sample; refracted light leaves the sample, passes through the condenser lens, and hits the Position Sensitive Detector (PSD). The PSD (dark blue) converts the light signal into two electronic signals: a sum signal, which is proportional to total light intensity, and a differential signal, which is linearly related to the position of the light spot on the sensor. These two signals are carried to an electronics box (green), where the differential signal is normalized by dividing it by the sum signal. The normalized signal is sent to the National Instruments Data Acquisition (DAQ) box (orange), where it is digitized and read into the computer (light blue). To test whether aliasing was biasing our power spectra measurements, we inserted a homemade RC low-pass filter (white box) between the electronics box and the DAQ.

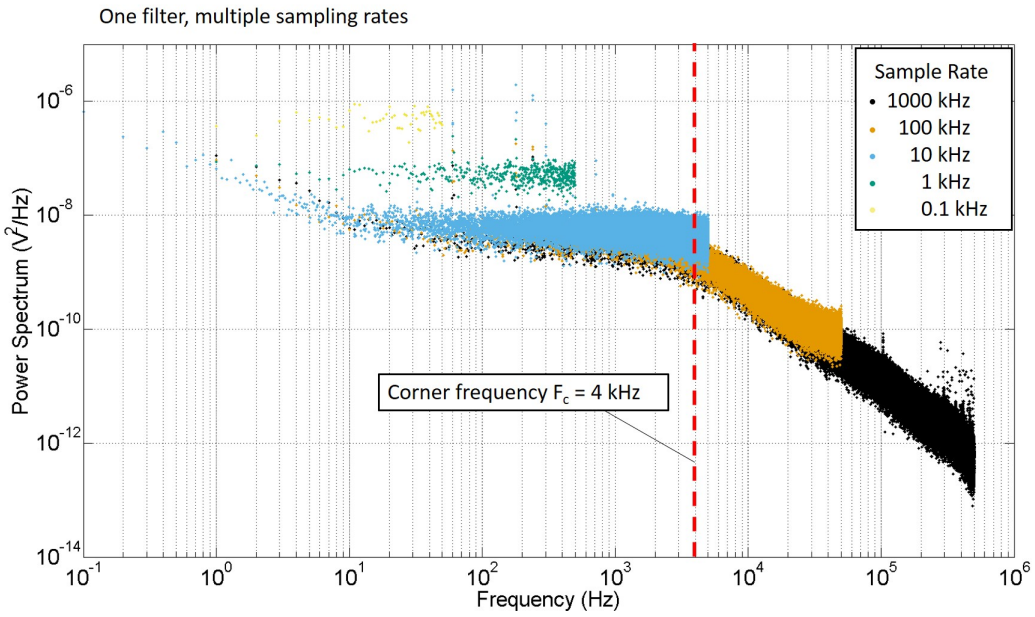

Figure 2.5: Power spectra of background noise after filtering with a homemade RC filter at a constant frequency. When our sample rate is higher than the characteristic frequency of the filter, we see the rolloff of the approximately white background noise imposed by the filter (black and orange data).When we sample at below the characteristic frequency, the high frequency signals are mistaken for lower frequency signals, which increases the computed magnitude of the power spectra (green and yellow data). The data from the higher sampling rates overlap each other because the RC filter sufficiently attenuates the higher frequencies; these components are still aliased into the lower frequencies, but because their attenuated magnitudes are small the effect is minimized.

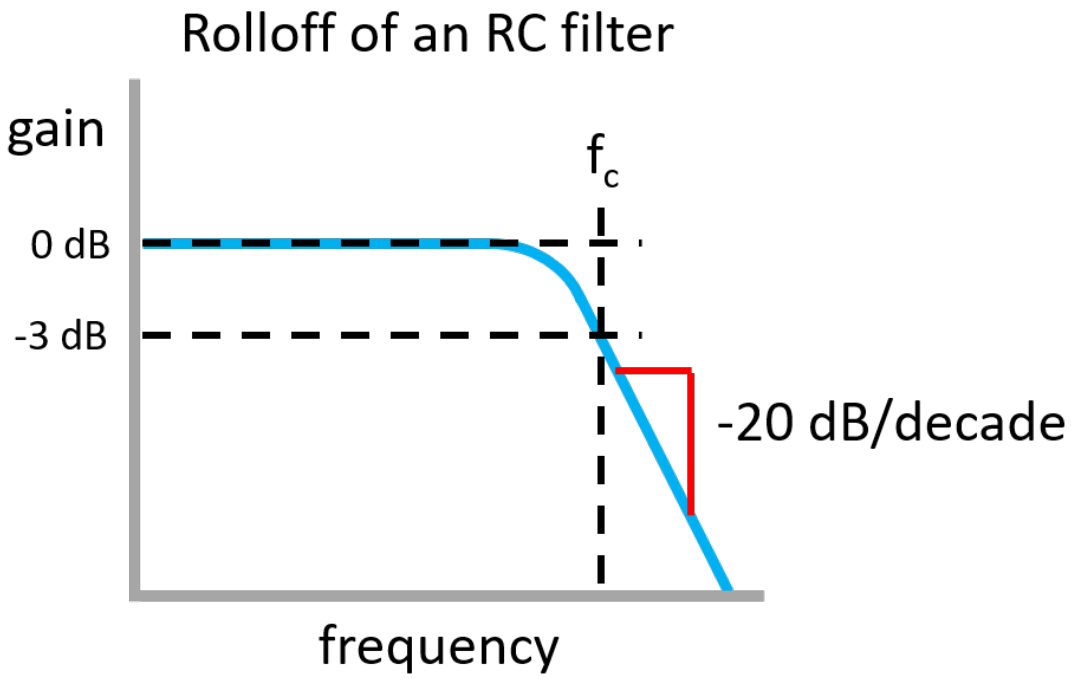

Figure 2.6: Characteristic frequency response of an RC low-pass filter [52]. The corner frequency f_c describes the frequency location at which the filter begins to attenuate a white noise signal. We expect to see a shape similar to this when filtering the background noise in our setup.

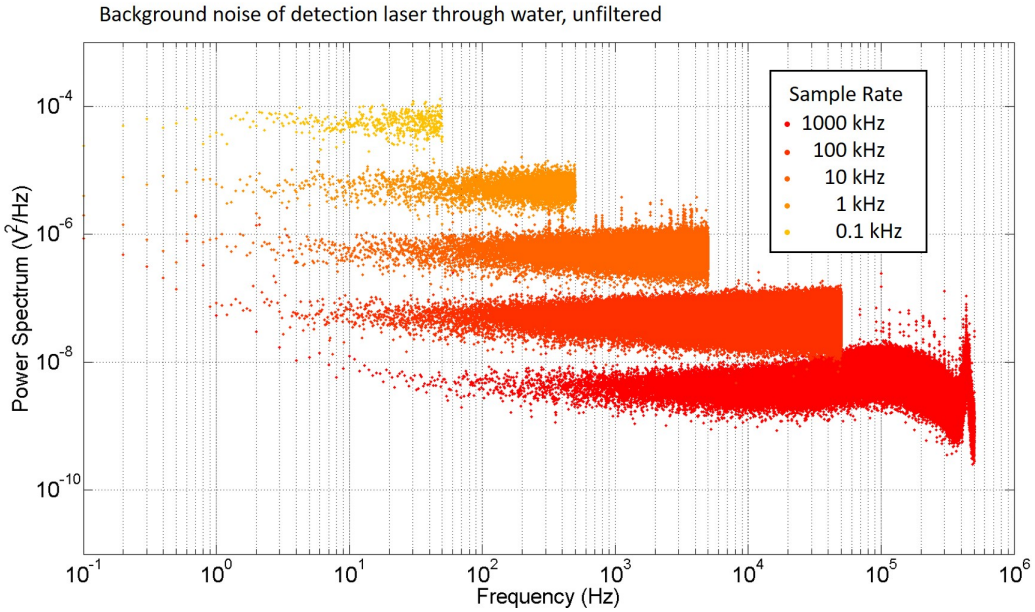

Figure 2.7: Background noise measured when the sample chamber was filled with water and no particles. The detection laser spot hits the PSD and any signal changes are due to mechanical vibrations or electronic noise.

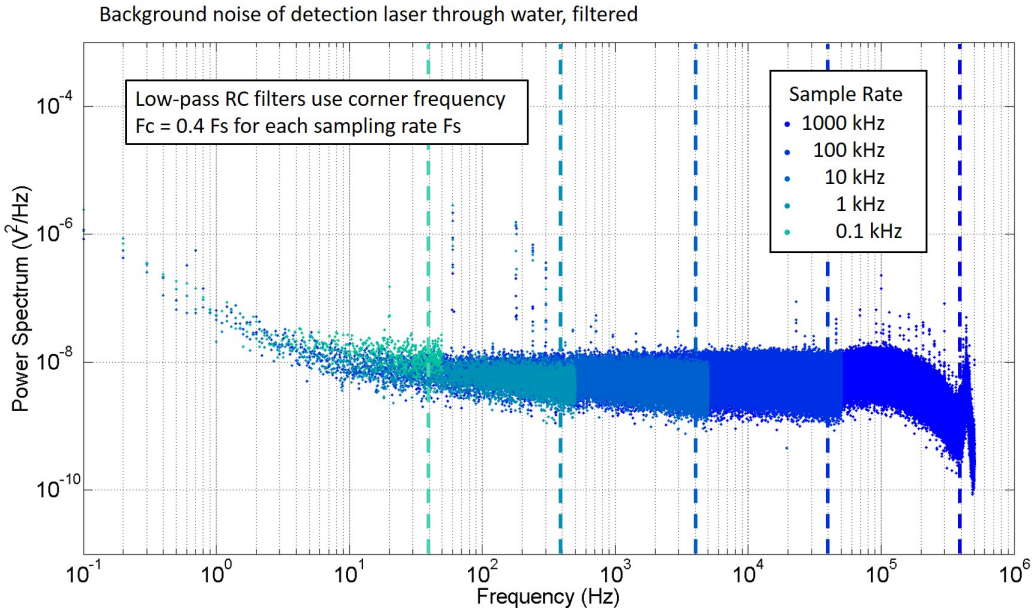

Figure 2.8: Power spectra of background noise after filtering with homemade RC filters with corner frequencies of 0.4 times the sampling rate. These signals are the same signals shown in Figure 2.7, after being passed through an RC filter. Filtering the signals at slightly below the Nyquist frequencies for each sampling rate reveals the true shape of the background noise power spectrum.

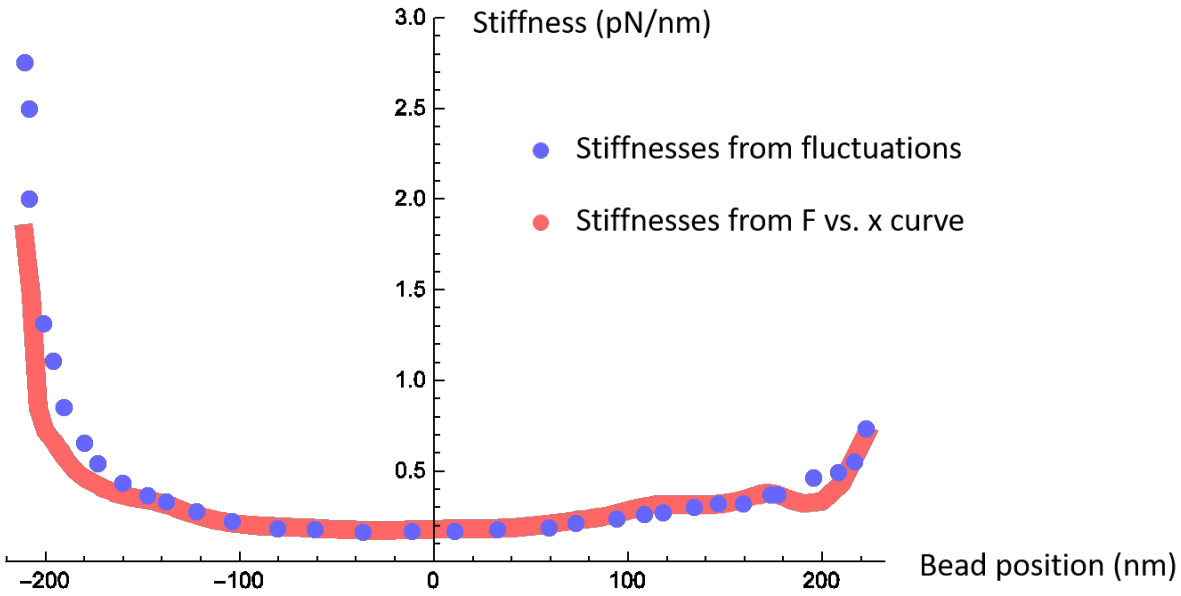

Figure 2.9: After the addition of the Krohn-Hite filter, the stiffnesses calculated from the Stokes' Drag method (red) matched the stiffnesses calculated from the Fluctuations Method (blue).

2.4.2 Improvements to Trapping Efficiency and Motion Dexterity through the Addition of a Large-Range Electronic Substage and a Joystick

Trapping a 1 micron particle can be extremely tricky. The diffusing particle's motion is erratic, unpredictable, and fast compared to a human's reflexes. In addition, there are regions of the trapping beam near its focal point in which the scattering and gradient forces will strongly repel a particle. To successfully trap a particle, the experimenter must either deftly route the particle so that it enters the trap through the restorative force regions of the beam, or shutter the beam, position the particle near the trap focus, and then immediately open the shutter to secure the particle.

The experimenter also requires sufficient range of motion to be able to find particles to trap. There are many ways to construct a sample chamber, but a chamber that is too densely filled with particles produces the problem of unwanted particles diffusing through the measurement laser path, or falling into the trapping laser focus. Therefore, our assays call for either dilute solutions of particles to be added to the chamber, so that there may be only one particle within tens of cubic microns, or for a reservoir of particles (see section 3.5. Either way, the experimenter needs to move hundreds to thousands of microns to find sufficient particles to complete the experiments.

The combination of a small pizeo stage and manual substage allowed us to perform many useful tasks, but trapping particles and moving through a sample chamber was tedious and time consuming. We used the manual substage for its range and relative dexterity (compared to the simple motion control GUIs we had in place for the piezo stage at the time) to trap particles, and then we switched back to running the piezo stage through predefined routines in LabVIEW, for example to calibrate the PSD or to apply a drag force to a particle by moving the stage. The physical separation of the computer and

microscope created a layer of complexity that slowed experiments obstructed workflow. Besides this, any navigational use of the P-517 stage for finer position adjustments would quickly accumulate until the stage reached the edge of its range. The only ways to reset the stage to its center position were to move it back electronically and lose the current field of view, or to move the substage by hand but at far greater speeds and far less precision than desired.

We replaced the manual substage with a PILine stage with a larger range and higher velocities to improve our range of motion and allow us to survey a larger area to find particles to trap. Although the PILine stage has a lower motion resolution and speed accuracy compared to the P-517 stage, routines that require finer control can still be performed by the P-517, but without the worry that the stage will become stuck at the edge of its range.

To improve trapping efficiency, we installed a joystick (Logitech 963290-0403 Extreme 3D Pro Joystick for Windows). The intuitive interface of a joystick significantly improved our ability to trap particles, and narrowed the lag between trapping and data collection. It also pairs well with our LabVIEW-driven keyboard controls, allowing us to shutter the trap, position a particle, open the shutter to trap the particle, switch between microscopy modes, and collect images and data, all within seconds (see Section 2.6.1).

With the additions of the PILine stage and the joystick, we can now instantly switch between two orders of magnitude of motion with both manual and computer control. This has greatly improved experimental efficiency and will benefit future investigations.

A finely controlled and accurate range of motion is critical for particle position and trap force calibrations (see Sections 2.3.5 and 2.3.6). Our smaller piezo stage has been invaluable in performing these delicate operations. The PILine stage has the advantage of much higher velocities, which can develop the larger drag forces necessary for the optical trap force calibrations described in Section 4.2, and for the force scaling validations in

Section 4.3.

2.4.3 Addition of Vision Aids

Though simpler and more fun than typical hardware modifications, the addition of phosphorescent adhesive labels was enormously helpful to the trapping workflow. The necessary use of a computer, even with brightness turned down, prevents the eyes from adjusting to the dark space of an optics room, and makes the surrounding equipment appear too dark to distinguish various components. Glow-in-the-dark stickers were placed in strategic locations including the microscope focusing knob, on small movable items such as laser cards and flashlights, and on the floor to mark out pathways of cables that had to be routed across walking paths. We also placed and labeled stickers onto keyboard keys designated through LabVIEW VIs for high-level functions, such as switching microscopy modes and toggling the trapping laser's shutter. These modifications improved experimental efficiency as well as safety, both for the experimenter groping in the darkness and for sensitive equipment reliant on the experimenter's steady hand.

2.5 Investigating the Accuracy of Piezo Stage Velocity

For the measurements described in Chapter 4, it was important for us to understand the accuracy of the pizeo stage velocity. For both of our piezo stages, we measured the velocity accuracy and precision by commanding the stage to move at various constant velocities, then querying the stage's own position sensors at constant time intervals.

For the smaller-range P517 stage, the velocity measurements were only performed in the "x" direction, the direction in which experiments were performed. Measurements in

both directions were performed for the larger-range M686 stage.

The measured vs. commanded velocities of the stages are shown in Figures 2.10–2.15. The P517 errors ranged from 1 to 4 percent with a maximum absolute uncertainty of 6 microns/s for the highest velocity tested, 400 microns/s. The M686 stage also showed errors from 1 to 4 percent, with a maximum absolute error of 0.1 mm/s at 11 mm/s. The precision found for both stages by either taking the standard error of the mean of many velocity measurements, or by taking 95% confidence intervals on the slope of displacement vs. time plots, was smaller than the measurement resolution, which was about 3 nm/s for the P517 stage, and 3 microns/s for the M686 stage.

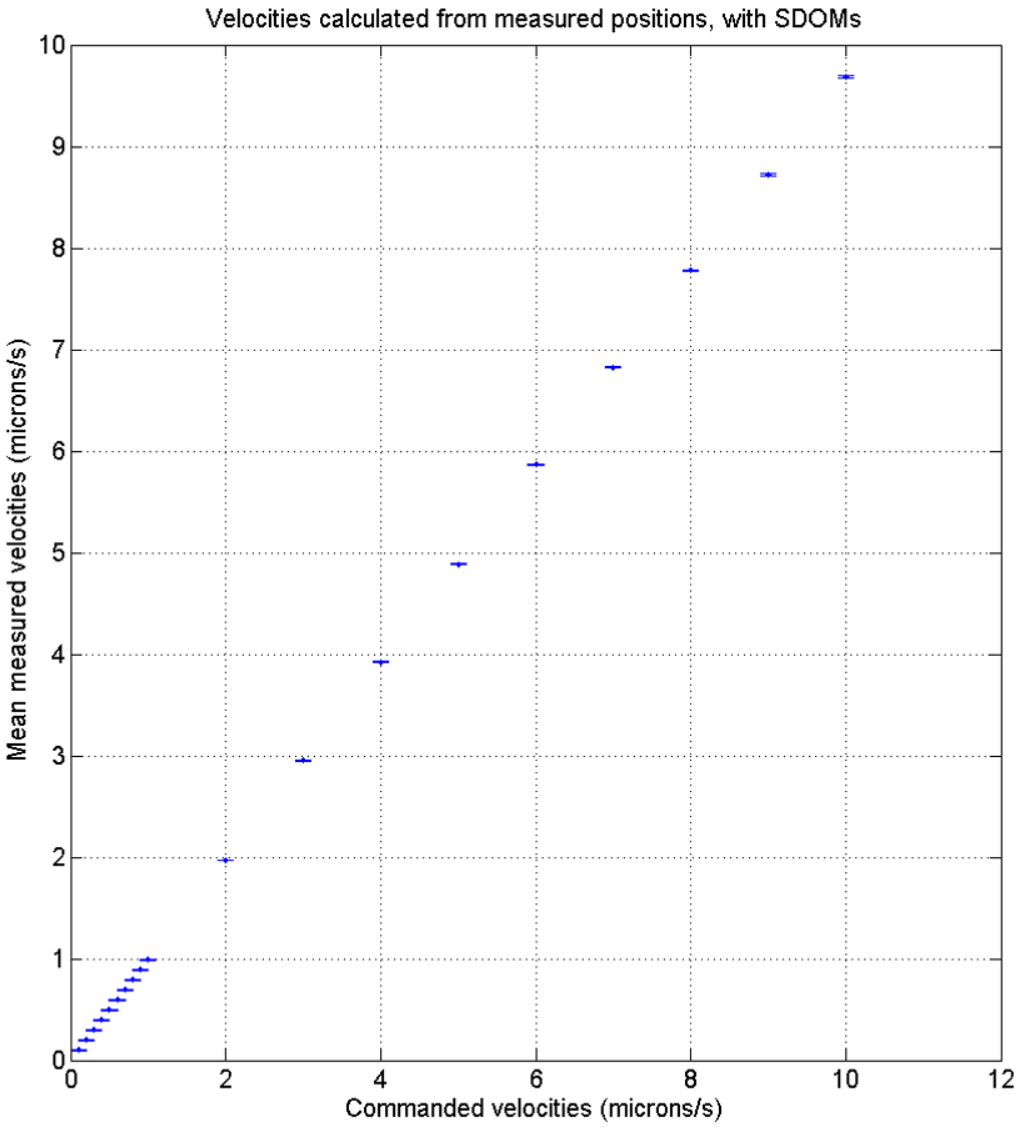

Figure 2.10: Velocity measurements for the P517 Stage. The stage was commanded to move at a constant velocity and its positions over time were read out from the stage's own sensor.

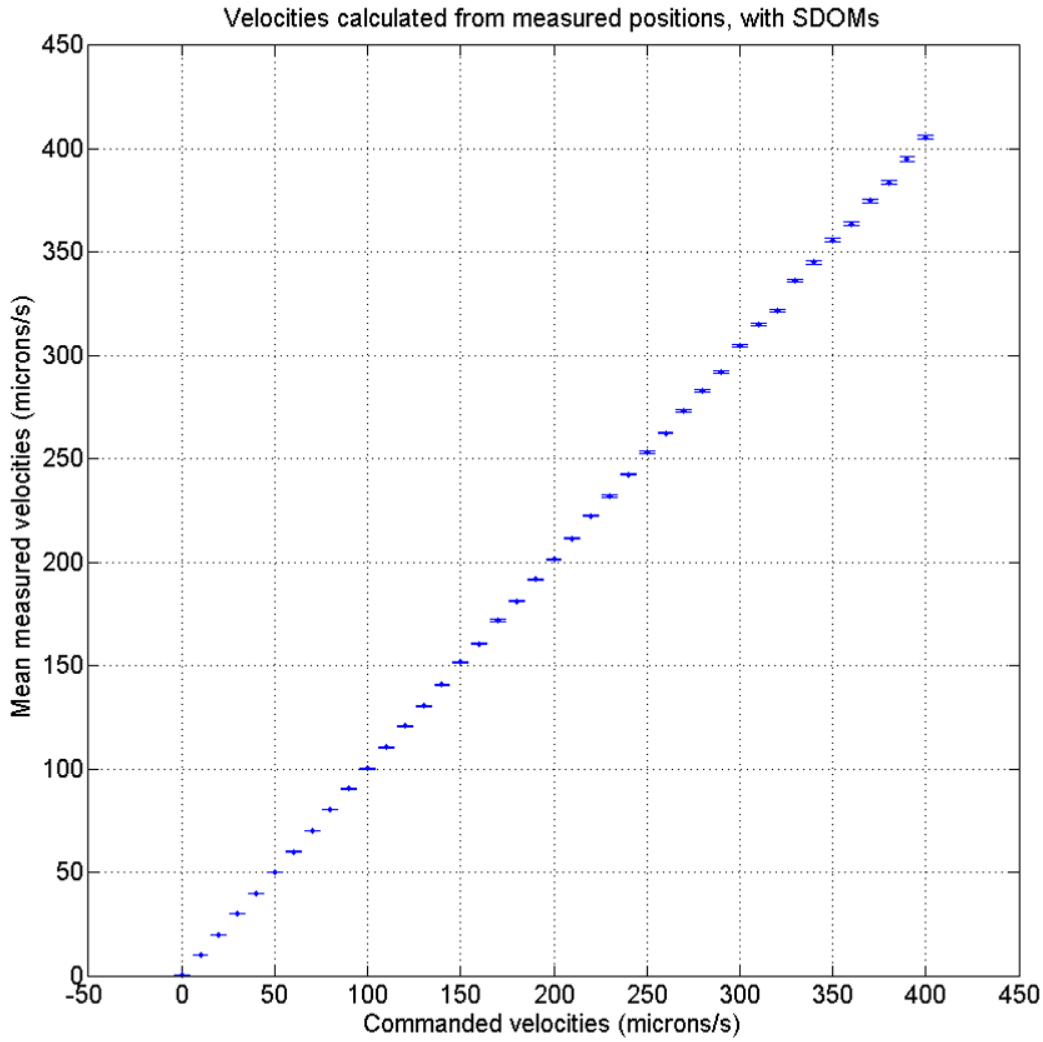

Figure 2.11: Velocity measurements for the P517 Stage. The stage was commanded to move at a constant velocity and its positions over time were read out from the stage's own sensor.

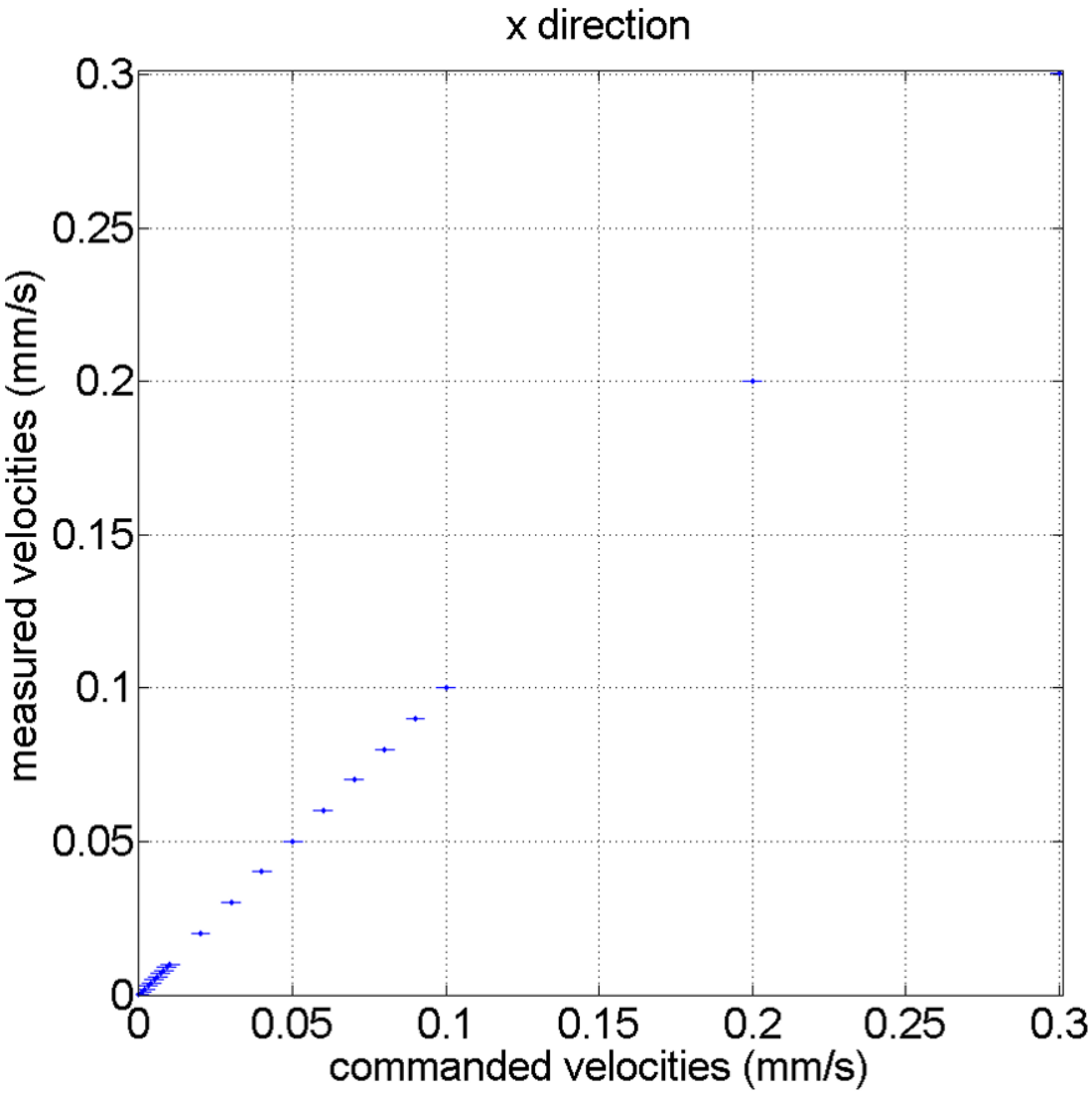

Figure 2.12: Velocity measurements for the M686 Stage, in the x direction. The stage was commanded to move at a constant velocity and its positions over time were read out from the stage's own sensor.

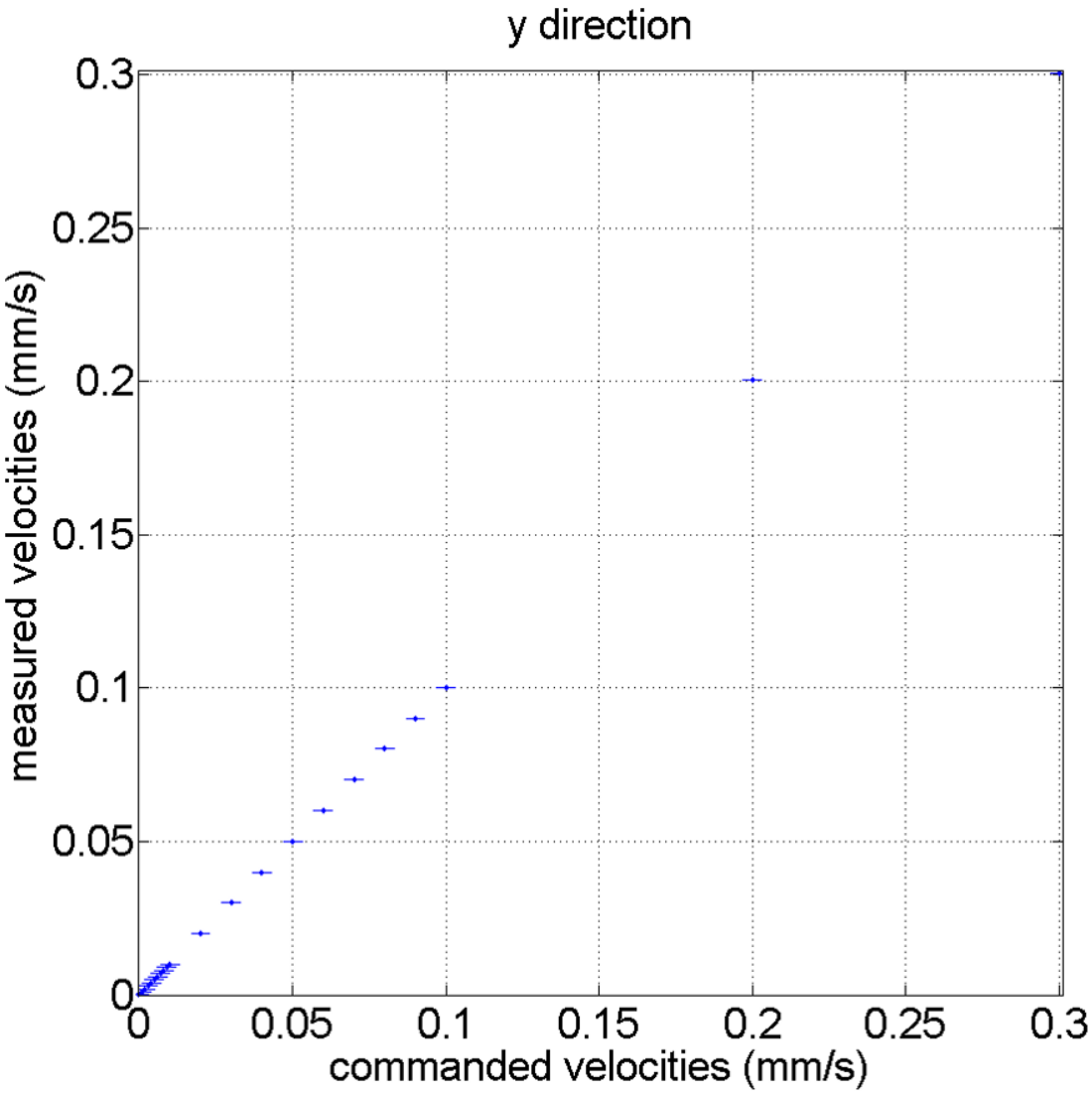

Figure 2.13: Velocity measurements for the M686 Stage, in the y direction. The stage was commanded to move at a constant velocity and its positions over time were read out from the stage's own sensor.

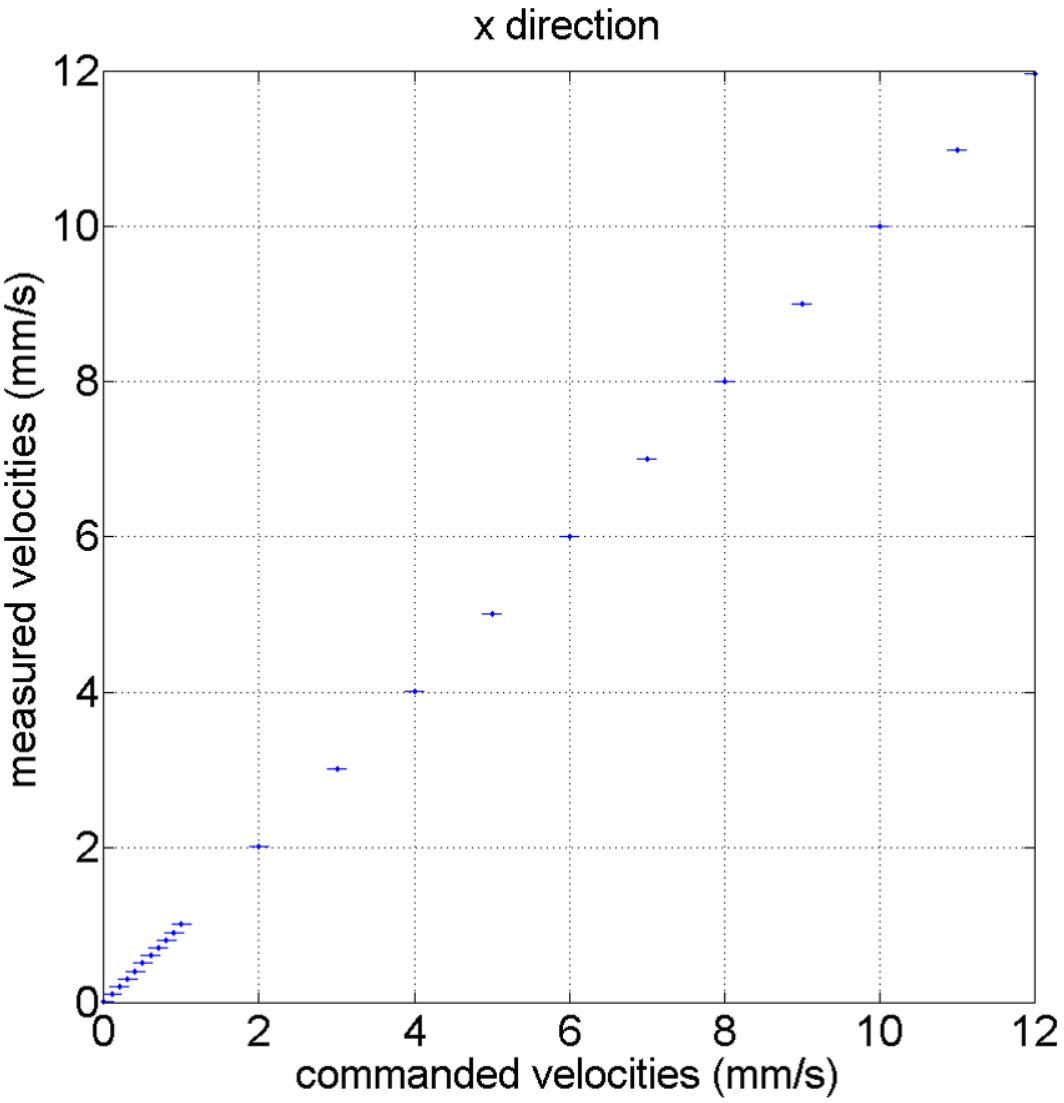

Figure 2.14: Velocity measurements for the M686 Stage, in the x direction. The stage was commanded to move at a constant velocity and its positions over time were read out from the stage's own sensor.

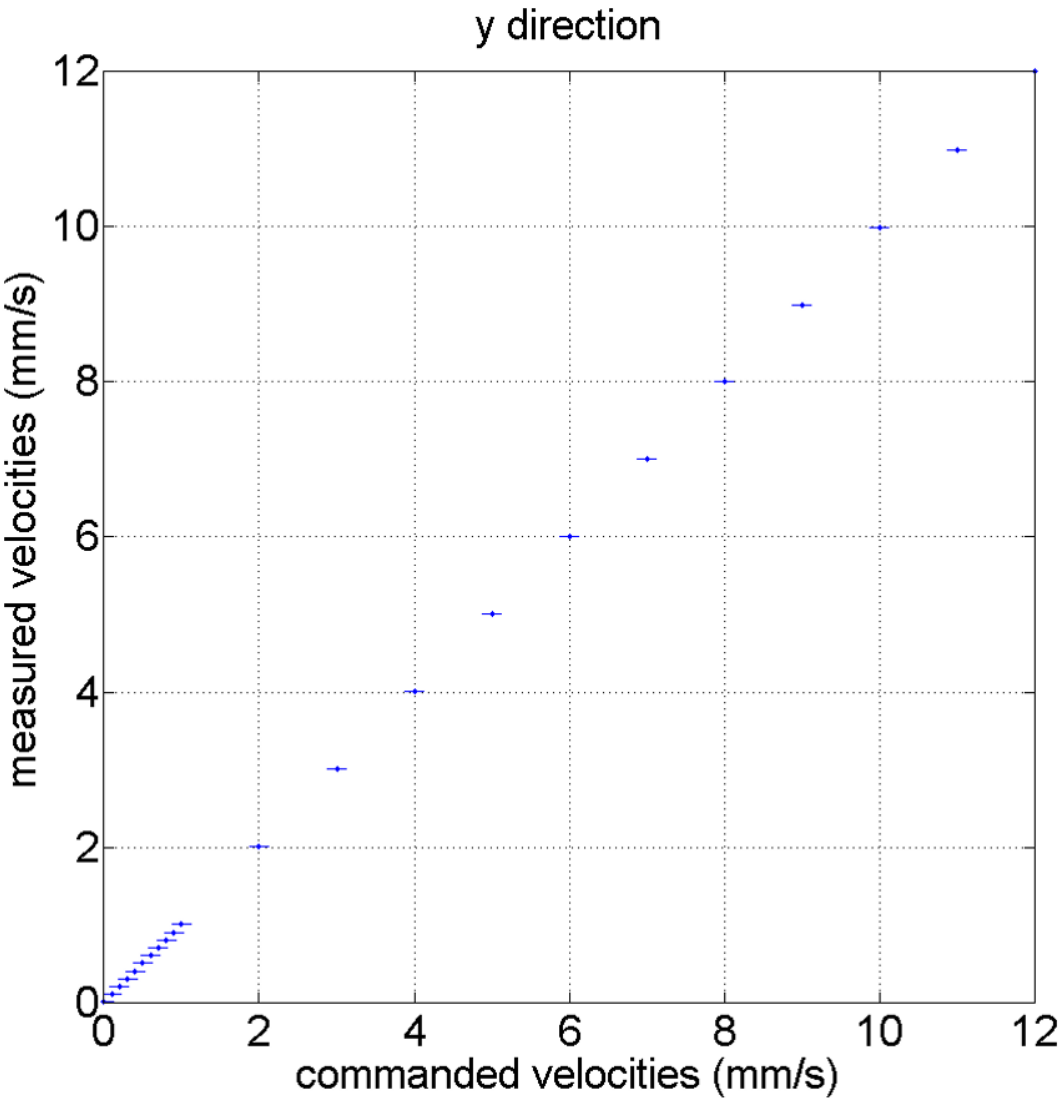

Figure 2.15: Velocity measurements for the M686 Stage, in the y direction. The stage was commanded to move at a constant velocity and its positions over time were read out from the stage's own sensor.

2.6 Software

2.6.1 Equipment Operations and Routines in LabVIEW

We wrote many LabVIEW Virtual Instrument programs to run the optical trapping equipment. Here we describe three of the most important VIs. These programs were written to optimize experimentation ease, allowing the experimenter to obtain data at a moment's notice and avoid mistakes. More VIs are described in Appendix A.

Cameras_JCW_15.vi

This VI runs both the small PGR CCD camera (with USB connection to the computer) and the Andor EMCCD camera (connected through a PCI card, plugs into the back of the computer) at the same time. It controls a temperature loop to appropriately cool the EMCCD camera, and allows acquisition and saving of images from each camera.

The user can change the camera settings and enforce an approximate frame rate for camera sampling. The Transfer Andor ROI to CCD Camera will take the Andor ROI (click on the Andor image to create an ROI) and transform it to map it onto the CCD camera image. This is useful for, for example, trying to keep track of the location of microtubules between TIRF and brightfield. The VI allows the user to collect either a set number of finite frames from the Andor EMCCD, or to continuously save images.

EscapeExperiments17_JCW.vi

This VI controls the Brightfield Lamp shutter, Camera Mirror, Detection Laser shutter, Trapping Laser shutter, Green Laser shutter, Blue Laser shutter, M686 PI Stage, P517 PI Stage, and DAQ sampling. Several keyboard shortcuts facilitate optical trapping workflow: the control key toggles the trapping laser shutter open and closed. Enter starts data colletion. The arrow keys control the motion of the M686 stage, and Shift

stops it. The user can adjust the stage velocity values in the VI. Arrow buttons on the VI control the P517 stage.

StokesDrag7JW.vi

This VI was used to perform the Stokes Drag measurements. It automatically sweeps the stage and its fluid past a trapped bead and records the bead's displacements from the stationary trap center over time. The measurement uses the PSD voltages and volts per nm calibration factors to determine the bead's displacement. This version only moves the stage at one velocity, but it performs multiple trials at the same velocity.

2.6.2 Analyses in MATLAB

We also wrote many routines and functions in MATLAB to analyze data. Below are two of the most important analysis files.

ProcessPS2.m

This function imports particle position data and calculates power spectra, and stiffnesses using two methods. The first method for obtaining stiffnesses is called the Equipartition method and is described in Section 4.1.1. The second method is called the Power Spectrum method, and is also described in Section 4.1.1. In the code, we fit a Lorentzian to the power spectrum to extract two parameters with confidence intervals. This function takes these parameters from many different trials and averages them together.

findSDRampUpStart2.m

This function takes in particle position vs. time data, collected from trapped particles under a constant drag force. The data typically shows the particle fluctuating about an

average displacement, and includes the particle's return to the trap center as the stage velocity returns to zero. This function isolates the particle positions under constant force by smoothing the data, then fitting a piecewise function to it to find the cutoff point where the particle begins its return to the trap center.

Chapter 3

Biomimetic Droplets

3.1 Introduction

As described in Section 1.1.3, most collective kinesin studies have been performed using solid cargoes[33] [11] [15] [12]; however, we predict that the surface properties of cargoes can affect collective kinesin behavior. It is possible to use in vivo vesicles to investigate collective kinesin behavior[31], but such studies pose a number of challenges: the researcher must deal with cells and coax them to express the desired vesicles and proteins, and must also accept the highly variable conditions within living cells. The researcher may not even know what protein complexes exist within the membranes of endogenous lipid droplets. These limitations obstruct the systematic variation of experimental parameters necessary for a complete understanding of the effects of cargo surface properties on collective kinesin transport.

To more efficiently probe collective kinesin transport on fluid cargoes, a model system is needed to capture the relevant surface properties of cellular lipid vesicles and organelles. Namely, the model system should have a surface covered in freely diffusing elements that mimic the two-dimensional fluid surface of a lipid vesicle. To form a truly fluid surface,

the surface elements should be completely unattached from their neighbors so that they will slide past each other when an in-plane force is applied, but they should resist forces normal to the surface in order to maintain the shape and structural integrity of the cargo.

The surface elements must be functionalizable so that kinesins may be attached to the them, and the density of kinesins on the surface controlled. Ideally, the cargo surface could be fine-tuned to control its surface tension, overall solidity, and the mobility of the surface components within the 2D membrane. It would also be useful to have a modular surface chemistry, so that other motors besides kinesins could potentially be attached, allowing the cargoes to be used as a flexible model system that can be applied in many different studies.

In order to be able to probe the forces created by a group of kinesins acting on one cargo, the cargo must be trappable with an optical tweezer. The ray optics approximation for the trapping force reads:

$$F_{trap} = \frac{2\pi}{c} r^3 \left(\frac{m^2 - 1}{m^2 + 2} \right) \Delta I(x)$$

$$m = \frac{n_{particle}}{n_{medium}}$$

where r is the radius of the trapped particle, $\Delta I(x)$ is the intensity gradient of the laser, and $n_{particle}$ and n_{medium} are the indices of refraction of the particle and the surrounding medium, respectively. The cargo body must have a higher index of refraction than the medium in order to produce a trapping force. Additionally, the higher the index of refraction of the particle the larger the restoring trap force becomes, giving an incentive for finding a cargo body material with a high index of refraction so that higher forces may be applied to it. The particle size must also be close to the wavelength of the trapping laser, and the particle must not be absorbing at that wavelength.

The creation of such a model system for biomimetic cargoes will greatly benefit studies of molecular transport as it will allow for more accessible, systematic investigation of collective motor behavior.

3.2 Droplet Design

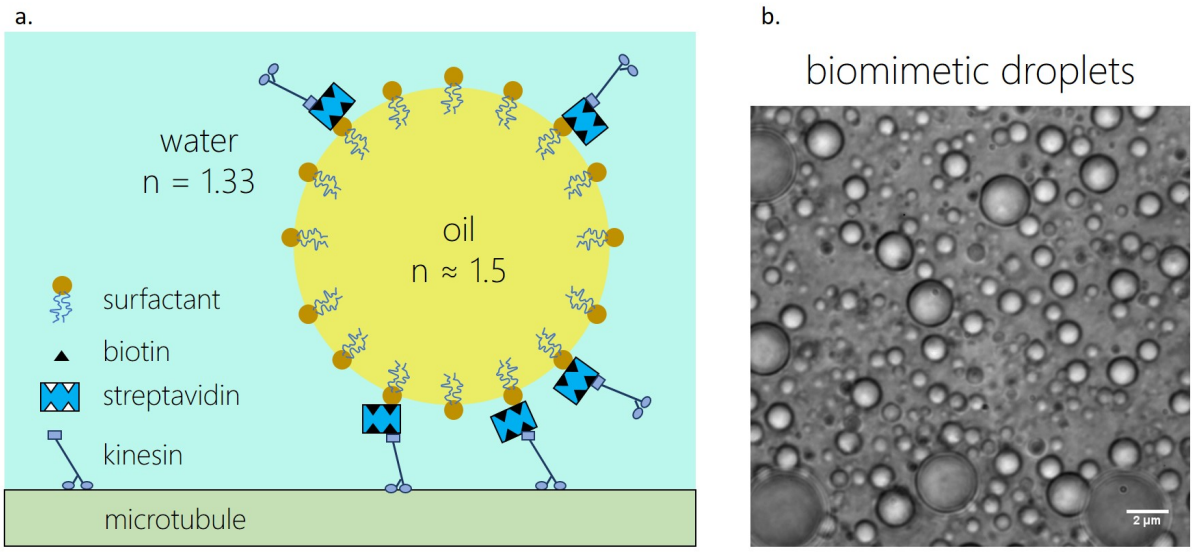

Figure 3.1: a. Designed biomimetic droplet system (not to scale). A sunflower oil droplet is coated with two types of surfactants–one surfactant type is biotinylated and one is not. Streptavidin is used to attach biotinylated kinesins to the biotinylated surfactants. b. Image of droplets.

The system we developed to match these constraints, shown in Figure 3.1 is to use oil droplets stabilized by surfactants; the surfactants are amphiphilic molecules that locate to the surface of the droplets and are freely diffusible within that surface. We use food-grade sunflower oil, which has an index of refraction of 1.5 [53], which exceeds that of water, which is 1.33 [54]. This difference allows the cargo to be trapped with optical tweezers, although the trapping forces will be smaller compared to commonly used polystyrene spheres (refractive index of 1.6 [47]) for particles of a similar diameter.

To link the motors to the droplets, we leverage a recently-developed system[55] in which two different surfactants are used: C16 PEG2000 Ceramide and DSPE-PEG(2000) Biotin. Both surfactants have small lipid tails which orient toward the oil phase of the emulsion, and large poly(ethylene glycol) (PEG)-based heads which orient toward the water phase—the large PEG heads have a stronger affinity for water than the small hydrophilic heads of the oil lipids, causing the surfactants to localize at the interface between the droplets and the water. The latter surfactant is conjugated with biotin, which allows biotinylated kinesins to be attached via a streptavidin link, providing near-covalent bond energies and supplying an efficiently permanent linkage. By controlling the ratio of the two surfactants, we can control the fraction of biotin groups on the droplet surface, and therefore we control the fraction of the surface to which kinesin is attached (by providing excess kinesin to ensure that every biotin has a kinesin attached.)

It should be noted that many biological cargoes are wrapped with a lipid bilayer, with water-based fluids on either side of the membrane. Such cargoes would be impossible to optically trap as there is no difference in the index of refraction between the cargo and surrounding fluid. While our biomimetic cargoes deviate from biological cargoes in this way, we expect to have captured the relevant mechanical properties of the lipid surface. The differences between biological cargoes and our biomimetic droplets are illustrated in Figure 3.2.

Our designed cargo fulfills all the desired qualities of a biomimetic droplet system, and can be used to probe the behavior of collective motor transport.

3.3 Oil Selection

As described in Section 3.1, a cargo with a high index of refraction is desirable to enhance the force of the optical trap, and at the very least the refractive index must

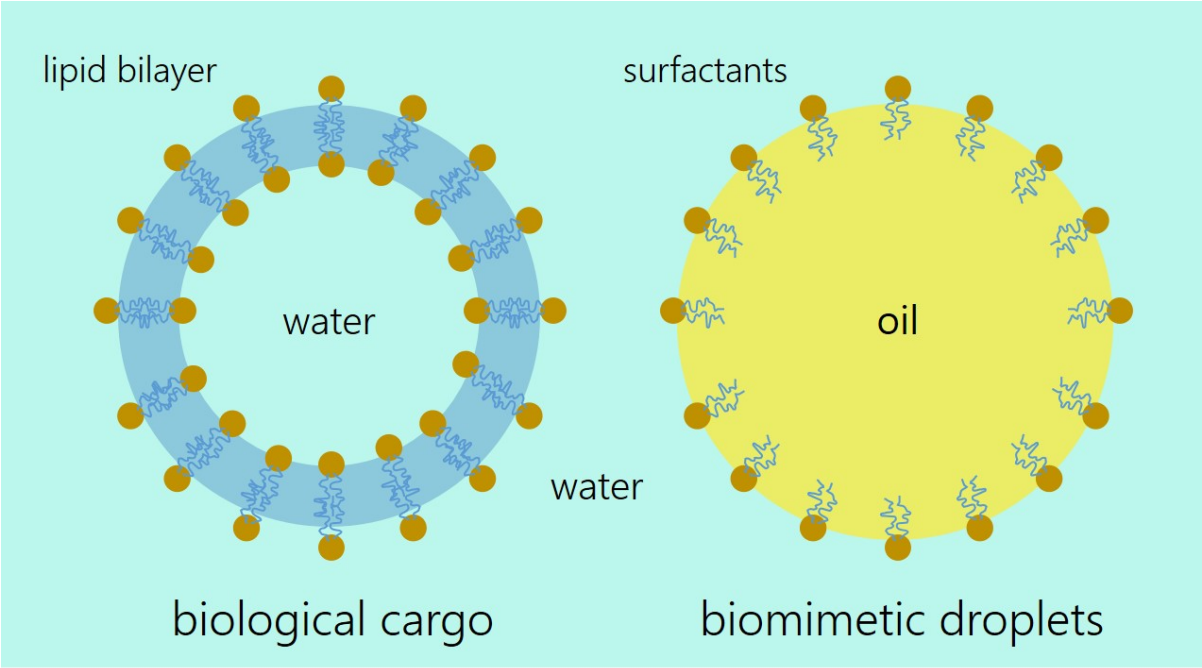

Figure 3.2: Biological cargo compared to biomimetic droplets: Many biological cargoes are contained within a lipid bilayer, with water both outside and inside the lipid membrane. These cargo are impossible to trap with optical tweezers because there is no change in index of refraction between the cargo and the surrounding medium. We avoid this issue with our biomimetic droplets because the droplets themselves are made of an oil, stabilized by a layer of functionalizable surfactants.

be higher than that of water (1.33) otherwise the trap will not be able to exert a force at all. When constructing a lipid droplet, the oil composing the droplet body should not have too high a viscosity, as this could increase the drag on the surface elements and restrict the fluidity of the surface membrane[56]. Finally, it is preferable that the droplet have a density higher than water, so that the droplets will sink to the bottom of the sample chamber where the optical trap can be focused, rather than rising to the top of the chamber out of reach of the trap. All of these criteria must be taken into consideration when selecting an oil for the main body of the biomimetic droplets.

Table 3.1 shows the typical properties of a few main types of oils. Fluorocarbon oils are denser than water, but they typically have low indices of refraction. Vegetable, mineral, and silicone oils have indices of refraction larger than water, but these have similar or lower density than water.

Table 3.1: Typical Oil Properties

Oil	**Density (g/mL)**	**Refractive Index**	**Viscosity (cP)**
Vegetable[57] [58] [59]	0.90–1.05	1.46–1.48	40 to 60
Mineral[60] [61] [62] [63]	0.84–0.87	1.46–1.48	around 15
Silicone[64] [65][66] [67]	0.93–1.05	1.4–1.5	45–60 000
Fluorocarbon[68] [69] [70]	around 1.8	around 1.3	large range

Table 3.2 shows a selection of specific oils that were considered and their properties. Silicone oils can have comparatively high indices of refraction, but typically these oils also have undesirably high viscosities. For comparison, water has a density of 1 g/mL, an index of refraction of 1.33, and a viscosity of 1 cP.

Ultimately, sunflower oil was chosen due to its fairly high index of refraction (about 1.47), and its reasonable viscosity (65 to 75 cP)[59]. Unfortunately, sunflower oil is less dense than water, meaning that sunflower oil droplets will rise in a chamber filled with water. In Section 3.5, two special chamber designs are described for alleviating this problem.

Table 3.2: Specific Oil Properties

Oil	Density (g/mL)	Refractive Index	Viscosity (cP)
Sunflower oil[59]	0.918 at 25°C	1.47	65 to 75 at room temp
Silicone oil, for melting point and boiling point apparatuses, Acros Organics (Fisher) [63148-62-9][64]	0.96	1.4030 to 1.4060	500 at room temp
Silicone oil, high temperature, Acros Organics (Fisher) [63148-58-3] Poly(methylphenylsiloxane)[65][66] at 25°C	1.0500	1.4940 to 1.5010	95 to 143
Mineral oil, BioReagent, for molecular biology, light oil, Sigma-Aldrich 8042-47-5[60]	0.84 at 25°C	1.467	74 to 86 at 40°C
Mineral oil, pure, Acros Organics (Fisher) 8042-47-5[61]	0.877	1.4760 to 1.4830 at 20°C	65 to 75 cSt at 40°C
Fluorinert FC-70[68] at room temp	1940 kg/m^3 at 25°C	1.303	24

3.4 Droplet Recipe

The biomimetic droplets are produced by combining 50 μL C16 PEG2000 Ceramide surfactants, 50 μL DSPE-PEG(2000) Biotin surfactants, 150 μL sunflower oil, and 900 μL water, then sonicating the mixture for 10 seconds to emulsify. Streptavidin is then added, and the mixture is vortexed for 10 seconds to coat the droplets. The largest droplets will float quickly to the top of the vial, and the remaining droplets will segregate along the gravity axis according to their size, due to differences in buoyant force under gravity. For optical trapping experiments, droplets are selected from the center of the droplet plug to avoid obtaining extremely large or small droplets. During experiments droplets of an appropriate size for trapping (about 1 micron in diameter) can be manually selected by visual inspection under a microscope using the imaging features of the optical trapping microscope.

3.5 Special Sample Chambers for Trapping Droplets

To observe biomimetic cargoes and measure their forces, a sample chamber must be constructed to hold the cargoes and place them in the vicinity of the optical trap. Figure 3.3 shows the assembly of a standard sample chamber made with a glass slide, double-sided adhesive tape, and a glass coverslip. The sample chamber is flipped upside down to meet the coverglass with the microscope objective on our inverted microscope setup. A high-numerical-aperture oil-immersion objective lens with high-infrared light throughput is used to tightly focus the trapping laser to create the trap, but this lens can only be focused within about 10 microns of the coverslip surface inside the chamber. Oil droplets less dense than water will quickly float out of reach of the trapping laser's focal point, which poses a significant challenge for performing experiments with the oil droplet-based cargoes.

One way to minimize the probability of droplets floating out of reach is to make sample chambers with a thinner material in place of the double-sided adhesive tape. PDMS can be spun onto square glass coverslips to a desired thickness by adjusting the spin time and speed[71]. Although a glass coverslip will seal on top of the PDMS, we found that it can be difficult to get the PDMS layer flat and clean enough to create a good seal, making this method difficult to employ.

To develop an alternative approach that to circumvents the problem of the buoyant droplets floating out of the depth of focus of the microscope objective, we created a chamber with a reservoir for storing the oil droplet cargoes. Figure 3.4 shows the construction of parafilm chambers, in which a main chamber is filled using the typical experimental assay, while a high-density solution of cargoes are added to a wedge-shaped reservoir at the end of the assay. Keeping the cargoes separate from the main chamber allows the experimenter to use stage controls to pick up a cargo at any time, and having the

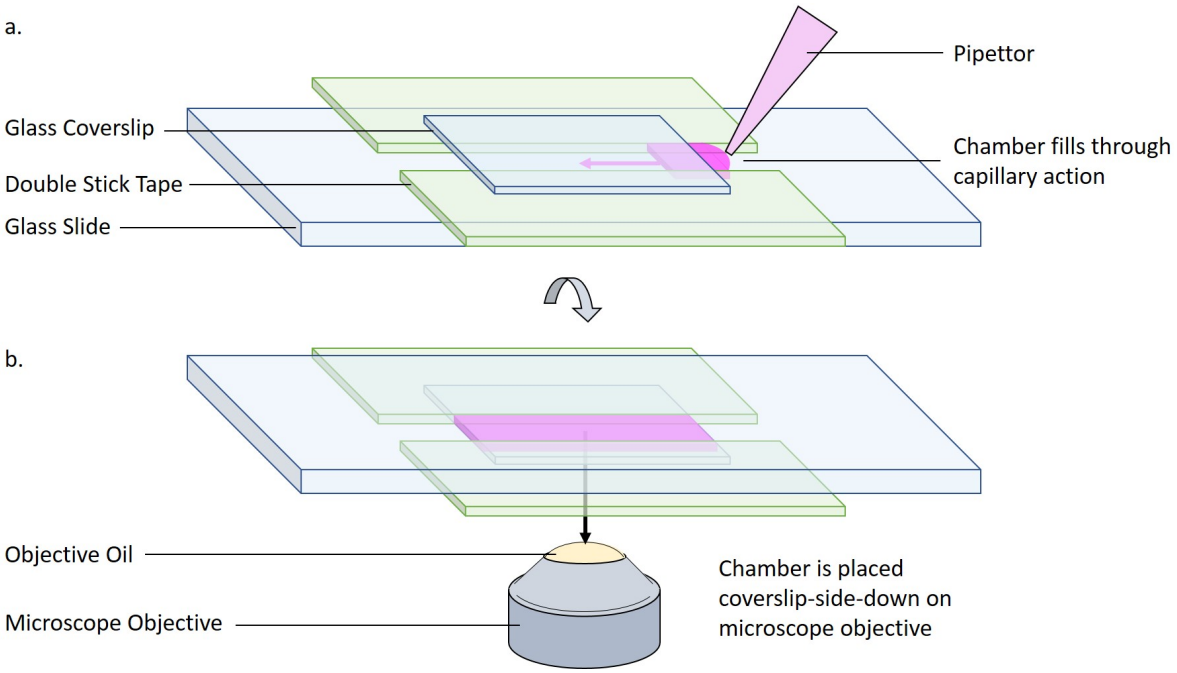

Figure 3.3: a. Assembly of a standard sample chamber. Two pieces of double-sided adhesive tape are placed about 5 apart on a glass slide, and a glass coverslip is set on top of the tape over the gap. The coverslip is pressed down with a pipette tip to create a seal between the glass and the tape, and the sample fluid can be pipetted into the empty space between the two glass surfaces–the fluid is pipetted at the chamber opening and capillary action pulls it through. b. In our inverted microscope setup, the microscope objective sits under the stage, and the chamber is flipped so that the coverslip can be placed in contact with the oil on the objective. (Glass and tape thicknesses are exaggerated for clarity, other dimensions are roughly to scale.)

reservoir densely-packed with cargoes ensures that there will be cargoes near enough to the coverslip to catch with the trap at all times. Parafilm can be finicky to work with, and it is essential to completely soften the parafilm so that a good seal may form, but to not over-heat the parafilm to the point where cracks form.

3.6 Using Interfacial Tension to Estimate Surfactant Surface Coverage

It is necessary for the experimenter to measure how many binding sites are available for kinesins on the biomimetic droplets. This can be achieved by measuring the interfacial tension between the droplet and the surrounding water. As described in Hsu et al. 1997[72] and Menger et al. 2011[73], the Langmuir adsorption isotherm can be used to calculate the surface fraction as follows:

$$\gamma - \gamma_0 = \Gamma_\infty RTln\,(1-x)$$

where γ is the interfacial tension of the surfactant and water system with an oil interface, γ_0 is the interfacial tension of a pure water-oil interface, R is the gas constant, T is temperature, Γ_∞ is the maximum possible surface concentration of surfactants, and x is the surfactant surface fraction in the system.

We can estimate the maximum surface concentration Γ_∞ by approximating the physical area taken up by a single surfactant as $a \sim 10nm^2$, which results in a value of $0.1 molecules/nm^2$, or $1.7 \times 10^{-7} mol/m^2$. The gas constant and temperature are known quantities, but γ and γ_0 must be measured for the experimental interfaces. Once the surface fraction is calculated, the droplet size and ratio of biotinylated to non-biotinylated surfactants can be used to approximate the number of binding sites available for attaching

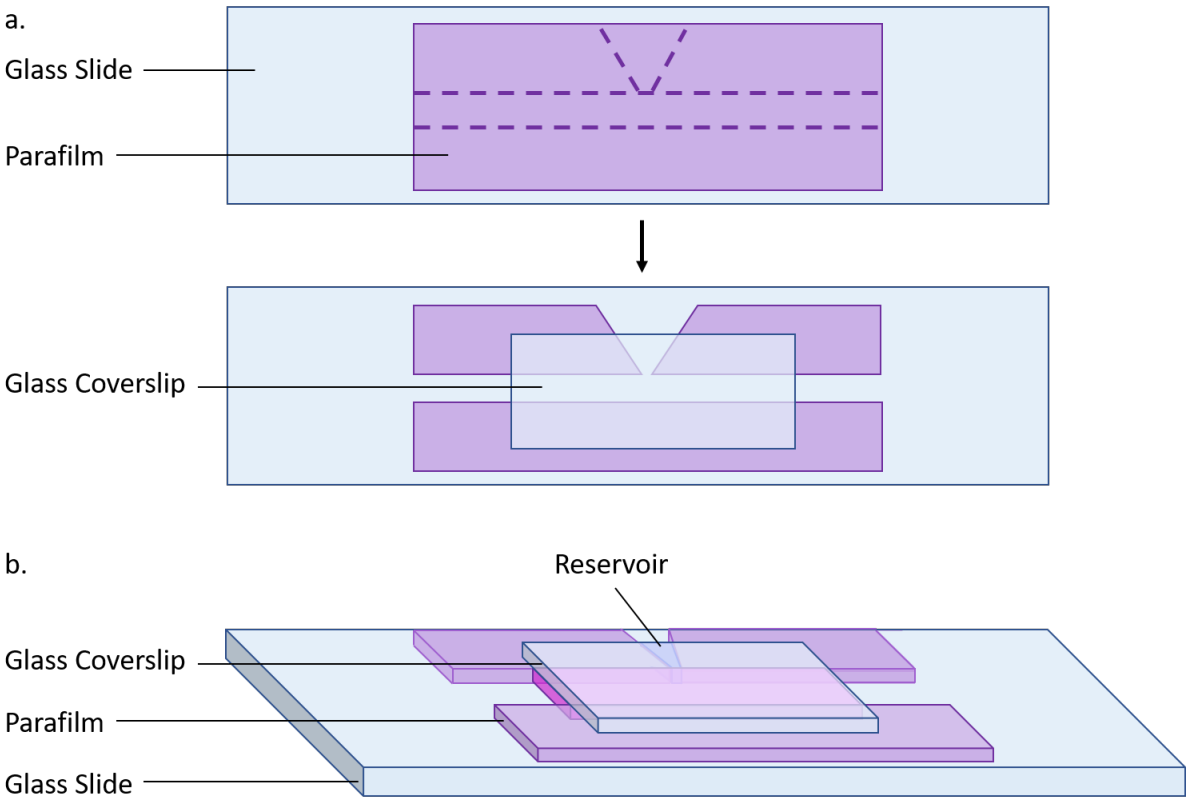

Figure 3.4: a. Top view of parafilm chamber construction. A strip of parafilm is cut to size and placed on top of a glass slide. A long rectangle is cut and peeled away to form the main chamber, and a wedge is also cut out perpendicular to the main chamber. The glass can be heated on a hotplate at 80 to 100 degrees C for a few minutes until the parafilm softens, and a glass coverslip should be immediately placed on top and gently rubbed with a pipette tip to seal the glass to the parafilm. b. 3D view of the parafilm chamber. The chamber can be filled like a standard chamber using capillary action. On the first filling, all the empty spaces including the main chamber and the reservoir will fill with liquid, and subsequent fluids can be pulled through the main chamber by using a kimwipe at the chamber exit to soak up the fluid. All of the steps in the assay that are to be performed in the main chamber should be completed first (attaching microtubules to the surface, blocking the surface, etc.), and the reservoir should be filled with cargoes afterwards, by pipetting the cargo solution at the reservoir entrance and using a kimwipe at the main chamber exit. Care should be taken to pull the fluid through slowly so that it does not migrate into the main chamber, and it is wise to fill the reservoir about 2/3 of the way and to let diffusion distribute the cargoes closer to the point where the reservoir meets the main chamber. (Glass and parafilm thicknesses are exaggerated for clarity, other dimensions are roughly to scale.)

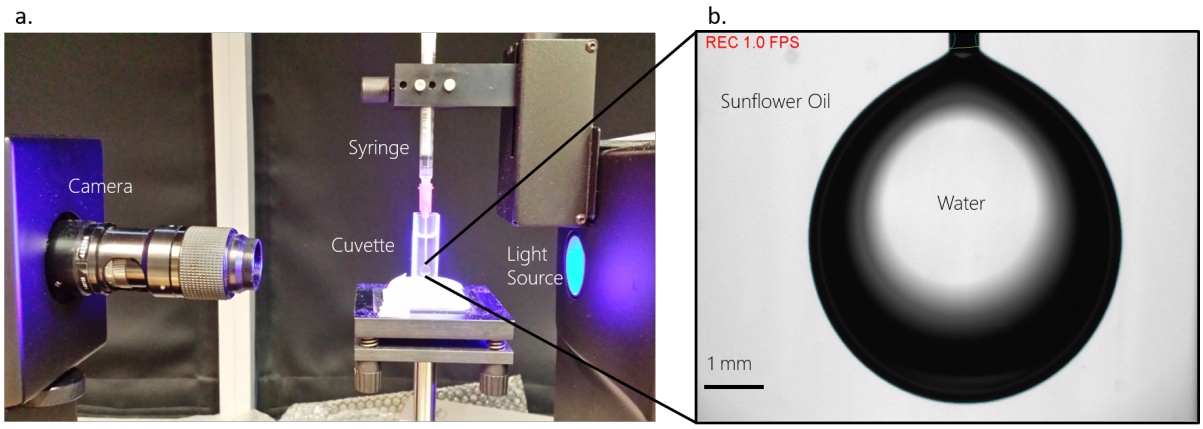

Figure 3.5: a. Attension Theta tensiometer setup. A droplet is suspended from a needle into a clear cuvette, which is backlit by a light source. A camera collects the image and proprietary software fits the droplet curve and calculates the interfacial tension. b. Closeup of droplet. We suspended a water droplet into sunflower oil. The PEGylated surfactants can be dissolved into the water phase, and over time they locate to the oil-water interface, reducing the interfacial tension until an equilibrium value is reached.

kinesins to the droplet.

To measure interfacial tension, we used a pendant droplet Attension Theta tensiometer. This apparatus contains a platform for holding a cuvette filled with fluid in which a droplet is suspended on the tip of a syringe needle (see Figure 3.5). In order to have a suspended droplet, the less dense liquid phase must fill the cuvette and the denser liquid phase must be suspended from the needle into the cuvette–in our case this means filling the cuvette with sunflower oil and suspending a water droplet into the cuvette. (Although floating droplet geometries are possible to measure, they are difficult to construct due to leakage issues.) Our surfactants' large PEG groups make them miscible in water, so we add the surfactants into the water phase and assume that they locate to their energetically favorable positions in the oil-water interface over time.

A camera records the droplet, and software fits the droplet surface curve and calculates the interfacial tension[74], which is measured as a function of time. The interfacial

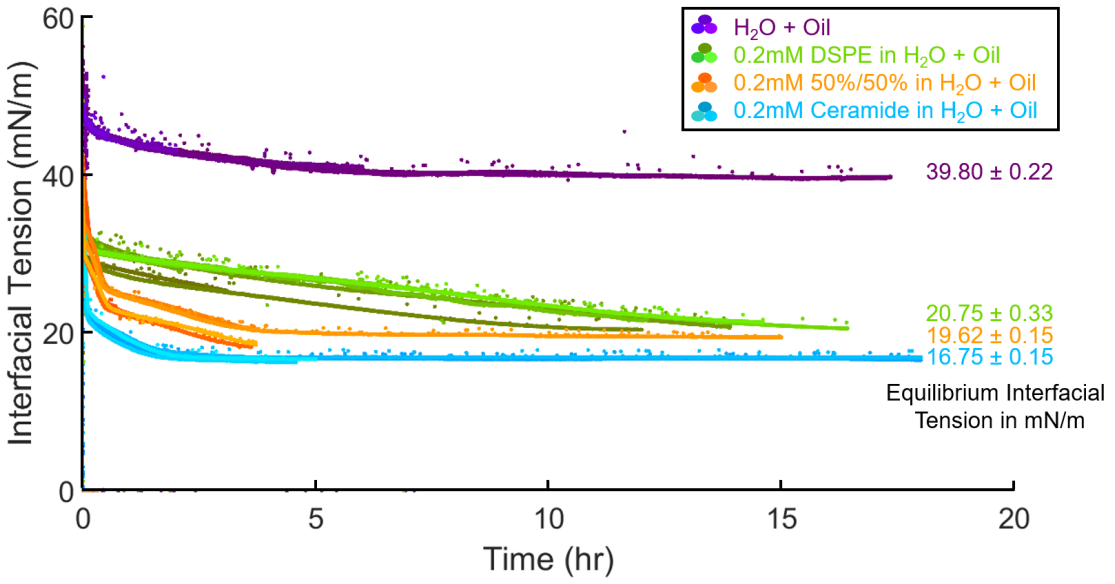

Figure 3.6: Comparison of the interfacial tension vs. time curves of different surfactant systems in an oil-water interface. The maximum interfacial tension is given by a pure water droplet in oil. Multiple trials measuring the interfacial tension over time of each system were performed.

tension can take many hours to come to an equilibrium value.

Figures 3.6 and 3.7 show interfacial tension vs. time for a number of tested systems. We fitted a power function to the curves to determine the equilibrium interfacial tension values. Figure 3.6 compares the interfacial tension curves of several different surfactant systems. Both Ceramide and a 50%/50% mix of Ceramide and DSPE surfactants reached an equilibrium interfacial tension relatively quickly, but DSPE alone produced an unusual, nearly linear decrease in the interfacial tension over time.

Figure 3.7 shows the interfacial tension curves of a Ceramide system of varying surfactant concentrations in powers of 100. As expected, increasing concentrations of the surfactant increasingly lower the equilibrium interfacial tension.

When we use the Langmuir adsorption isotherm equation to calculate the surfactant surface coverage, we obtain values of 100% coverage for all but 0.02 µM Ceramide, which

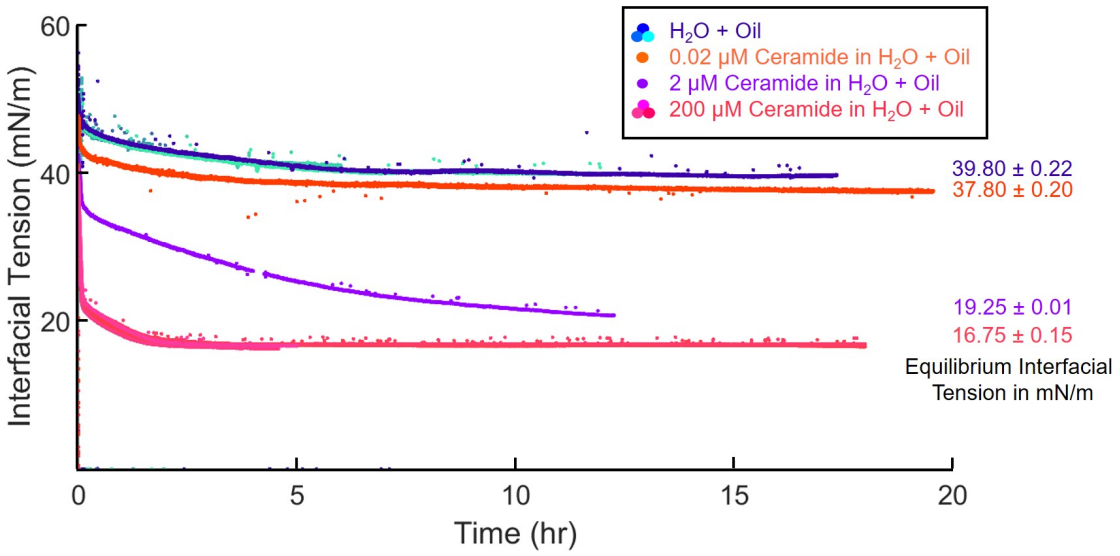

Figure 3.7: Comparison of the interfacial tension vs. time curves of different Ceramide concentrations in an oil-water interface. Multiple trials at each concentration were performed.

produces a value of 99% coverage. This indicates that even at what we consider to be low surfactant concentrations, the interface is saturated with surfactants.

3.7 Future Work: Adjusting Biomimetic Cargo Surface Properties Using Cholesterol

As an expansion to the biomimetic cargo system it would be interesting to adjust the surface properties of the cargoes to be somewhere between completely rigid and completely fluid. Cargoes of intermediate rigidity may be a better model for true biological cargoes, because biological membranes contain a diverse collection of lipids and proteins, resulting in more complicated surface properties. These cargoes could be used to investigate whether intermediate rigidity has a significant impact on kinesin behavior and transport. For example, cholesterol is known to increase cell membrane rigidity by induc-

ing the formation of lipid rafts (lipids in a liquid-ordered phase[75].) The lipid mobility of cargoes with incorporated cholesterol or other biological membrane components can be measured using established techniques such as fluorescence recovery after photobleaching (FRAP.)

Chapter 4

Optical Trap Force Calibration Improvements

4.1 Traditional Trap Force Calibration Methods

There are several established methods of calibrating an optical tweezers, most of which focus on obtaining the linear spring constant κ_L which can then be multiplied by the displacement of the particle from the trap center to obtain the force. The linear regime typically extends only about 100 nm on either side of the trap center, which is about a third of the useful range of the optical trap (useful range being defined as the range for which an increase in displacement produces an increase in the restoring force).

4.1.1 Linear Calibration Techniques

There are several ways to obtain a linear stiffness for an optical trap. In the Power Spectrum calibration method, the particle is allowed to diffuse under no external force about the center of the trap, and the power spectrum of the particle's position in the trap is calculated and fitted to a Lorentzian[47] (Figure 4.1). Two parameters are extracted

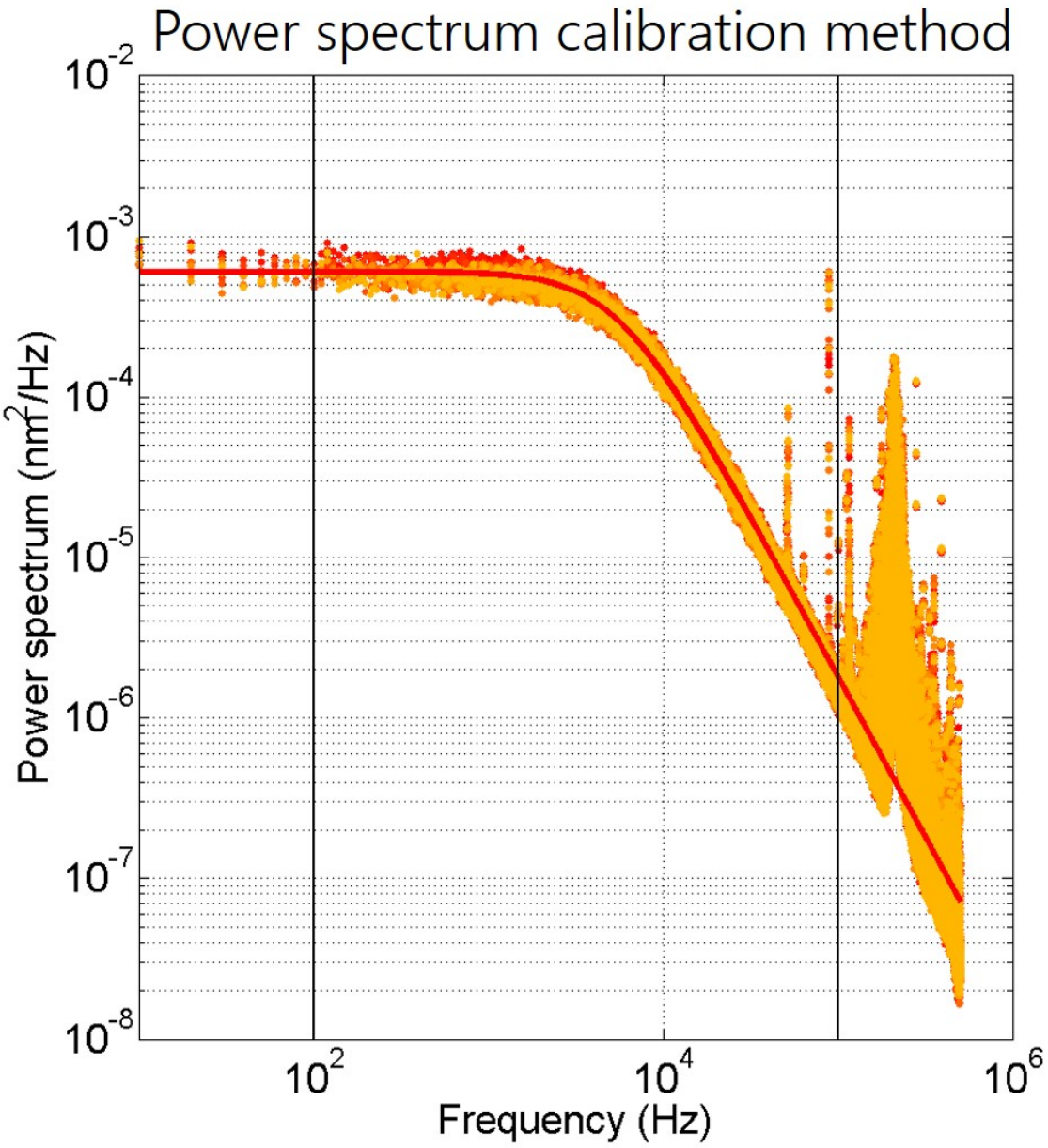

Figure 4.1: Power spectrum calibration method: A particle is allowed to diffuse within the optical tweezers under no external force. The position fluctuations of the particle are recorded over time, and the power spectrum of those fluctuations is taken and fit to a Lorentzian. The linear stiffness of the optical trap and the fluid drag coefficient are extracted from the fit.

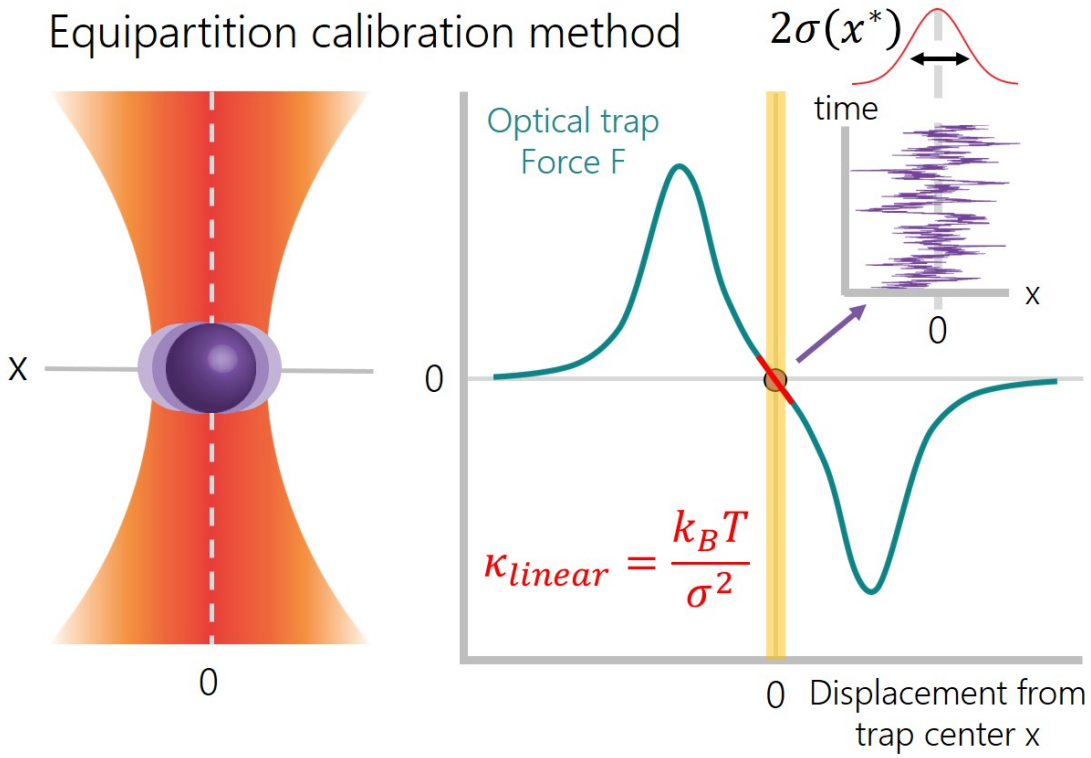

Figure 4.2: Equipartition calibration method: A particle is allowed to diffuse within the optical tweezers under no external force. The position fluctuations of the particle are recorded over time, and the linear stiffness of the optical tweezers is calculated from the variance of those fluctuations. A soft trap allows the particle to wiggle widely from the trap center, while a stiff trap holds the particle closer to its center.

from the fit: the linear stiffness, and the drag coefficient. For stiff traps, the thermal energy is weak compared to the trapping energy, and so the particle can only explore a very small region of the trap close to its center. For this reason, the stiffness found from the fit is assumed to be the linear stiffness of the trap, and is only valid within the linear region of the trap (about 100 nm on either side of the trap center.)

The Equipartition calibration method is similar to the Power Spectrum method in that the particle's position fluctuations under just the thermal forces are measured[47] (Figure 4.2). By equating the thermal energy to the energy of a linear spring, an expression for the linear stiffness can be obtained:

$$\frac{1}{2}k_BT = \frac{1}{2}\kappa_L \left\langle x^2 \right\rangle = \frac{1}{2}\kappa_L \sigma^2$$

$$\kappa_L = \frac{k_BT}{\sigma^2}$$

This method also depends on the assumption that the particle's explorations are small, probing only a small part of the linear range of the trap, and valid only for the linear range.

The Stokes' Drag calibration method differs from the Equipartition and Power Spectrum methods in that an external force is applied to the trapped particle[47] (Figure 4.3.) For this calibration the optical trap is held stationary while a piezo stage is moved at a very precise, constant velocity. The moving stage effectively moves the fluid in the chamber past the trapped particle, applying a drag force given by Stokes law, $F_{drag} = 6\pi\eta r v$, where η is the fluid viscosity, r is the spherical particle's radius, and v is the velocity of the stage. The quantity $6\pi\eta r$ is known as the drag coefficient, and as mentioned before, can be found by fitting the power spectrum of the particle's fluctuations about the trap center. The stage is moved at a few velocities, and the resulting average displacement of the particle is measured and plotted against the corresponding drag force. The slope of the force vs. displacement curve near the center of the trap is taken as the linear stiffness.

Even with an extremely high numerical aperture objective lens (NA = 1.49) and a 5 W laser, we found that we could only produce a force of about 40 pN at the extremes of the linear regime of our optical trap. Since the factors which could increase the maximum linear force are already maximized for our setup, we decided to expand our calibration into the nonlinear range to allow us to accurately measure the forces in a multiple kinesin system.

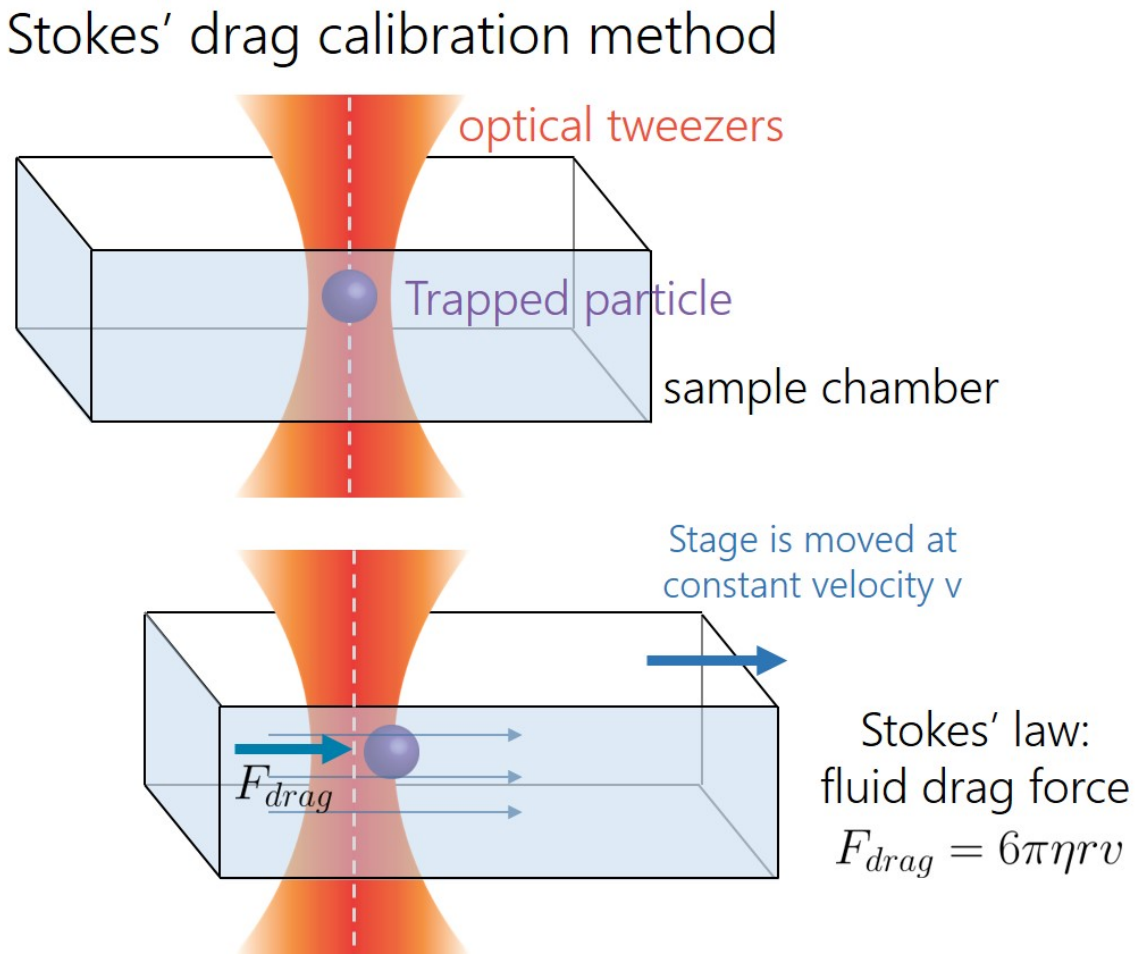

Figure 4.3: Stokes' drag calibration method: A fluid drag force is used to displace the particle from the trap center, and the resulting average particle displacement is measured.

4.1.2 Nonlinear Calibration Techniques

There are a few established methods for calibrating the nonlinear range of the optical trap. If the trapping energy is small compared to the thermal energy, the distribution of the particle's positions in the trap can be used to measure the nonlinear force vs. displacement curve [76]; this technique however is not useful for stiff traps and high trapping forces because the thermal energy alone will not allow the particle to explore the nonlinear range in such traps. Other methods involve the use of two optical traps, either in a dumbbell configuration [44] or directly overlapping the two laser spots [77]. In the two-trap methods, one high-power, stiff trap is used in its linear regime to pull a particle into the nonlinear regime of a separate, softer trap. Since the stiff trap is used only in its linear regime, this method does not provide a way to calibrate the nonlinear forces of a high power trap.

The Stokes' Drag method can allow the particle to explore the nonlinear range of the trap if the drag forces are large enough, but this method requires precise knowledge of the drag coefficient as well as special equipment (a precisely movable stage); for these reasons the Stokes' Drag method is typically used to check the linear stiffness found by the Equipartition and Power Spectrum methods, as opposed to precisely calibrating the nonlinear range. If the drag coefficient is to be calculated using Stokes' law, the fluid viscosity, particle radius, and particle's height above the chamber surface must be well characterized, and all of these quantities can be difficult to measure. Fitting the drag coefficient from the power spectrum invokes the assumption that the drag coefficient is constant with respect to the particle's displacement from the trap center. This assumption may not be true, as local heating from the beam could create areas of differing temperature and therefore regions of varying viscosity.

The fact that the trapping force is a result of the interaction between the light and

the trapped particle means that the force vs. displacement relationship can change significantly with each new particle, requiring recalibration. Any simplification that can be done to speed up the calibration is useful.

4.2 Improved calibration of the nonlinear regime of a single-beam gradient optical trap*

*Originally published in Optics Letters **41**(10):2386-2389 (May 2016), by Jamianne C. Wilcox, Benjamin J. Lopez, Otger Campàs, and Megan T. Valentine[78]. Reprinted with permission from [78], Optics Letters.

4.2.1 Abstract

We report an improved method for calibrating the nonlinear region of a single-beam gradient optical trap. Through analysis of the position fluctuations of a trapped object that is displaced from the trap center by controlled flow we measure the local trap stiffness in both the linear and nonlinear regimes without knowledge of the magnitude of the applied external forces. This approach requires only knowledge of the system temperature, and is especially useful for measurements involving trapped objects of unknown size, or objects in a fluid of unknown viscosity.

4.2.2 Introduction

Optical traps allow the precise application of forces to soft and biological materials [47]. A large number of biophysics applications, including most single-molecule measurements of motor proteins and biopolymers, require forces in the range of one to a few tens of pN of force, which is easily achieved using a standard single-beam gradient optical

trap. However, higher forces are often desired, for example to study collective behavior of multiple motor proteins [26, 36, 37], activate mechanotransduction pathways in cells [79], or probe the viscoelastic properties of cytoskeletal networks and other stiff polymeric materials [80]. In principle, it is possible to increase force by increasing the laser power, objective lens numerical aperture, or index of refraction of the trapped object. In practice, even after these inputs are optimized, the application of forces > 100 pN remains challenging.

An alternate way to increase the applied force is to increase the offset distance between the center of the trapped object and the center of the focused laser beam. Experimenters often limit this distance to <100 nm to ensure that the particle remains within the linear range of the optical trap, where the trapping potential can be reasonably approximated as a harmonic well. In this regime, a single value of the trap stiffness (linear stiffness) is used to relate offset distance and applied force, and numerous well-established calibration methods exist to determine its value [47]. However, by expanding the calibration into the nonlinear range of the trap, a substantial force increase can be achieved without the need to alter the existing instrumentation or to use exotic particle types [81].

Several prior nonlinear trap calibration techniques have been reported [49, 44, 77]. One approach used a dual beam optical trapping system to hold two particles connected via a polymer tether between a stiff trap, which had a well-known linear stiffness, and a soft trap, whose full nonlinear force profile could be determined [44]. A second method also employed a dual beam trap, again with one calibrated stiff trap and a second, weaker trap which was raster scanned over the interaction area of the trapped microsphere and the strong laser. This allowed a single particle to interact with both traps, permitting the nonlinear regime of the weaker trap to be explored [77]. In both approaches, only the soft trap was fully calibrated, while the stiff trap was operated exclusively in its linear regime in order to apply controlled forces. This prevents the experimenter from directly

measuring the highest possible forces using the available lasers.

An alternate method for probing the nonlinear range of the optical trap is to impose an external drag force on the trapped particle by moving the microscope stage (and therefore the fluid surrounding the particle) at constant speed. If the particle drag coefficient is known, it is possible to estimate the drag force and establish the force profile of the optical trap; this is commonly referred to as the "Stokes drag method" of calibration [82]. Although in principle the particle can be displaced into the nonlinear region of the optical trap by flow, calibration of this regime is not typically performed due to challenges in quantifying the external drag force, which depends on a number of factors through the particle's drag coefficient, including the exact particle size, the height of the particle above the sample chamber surface, and the viscosity of the surrounding media, which are difficult to measure accurately. Rather, the Stoke's drag method is used to approximate the spatial extent of the linear region of the optical trap, and to provide an independent confirmation of the linear stiffness, which is then compared to that measured by other established methods that rely on the thermal fluctuations of the particle only [47]. All existing nonlinear calibration methods have the drawback that they require the application of controlled, pre-determined forces.

In this Letter, we report an improved method that allows calibration of the full non-linear range of the optical trap without knowledge of the magnitude of the applied external forces. By analyzing the position fluctuations of a trapped particle while its average position is displaced from the center by an (unknown) external force, we obtain the local value of the trap stiffness at that displaced position. Repeating this procedure for different positions covering the full range of the trap, we obtain the full, non-linear trap force profile. To verify the accuracy of this approach, we compare our results to those obtained using the Stokes drag method and show that we can properly calibrate the stable nonlinear range without the need for a second optical trap, and without knowledge

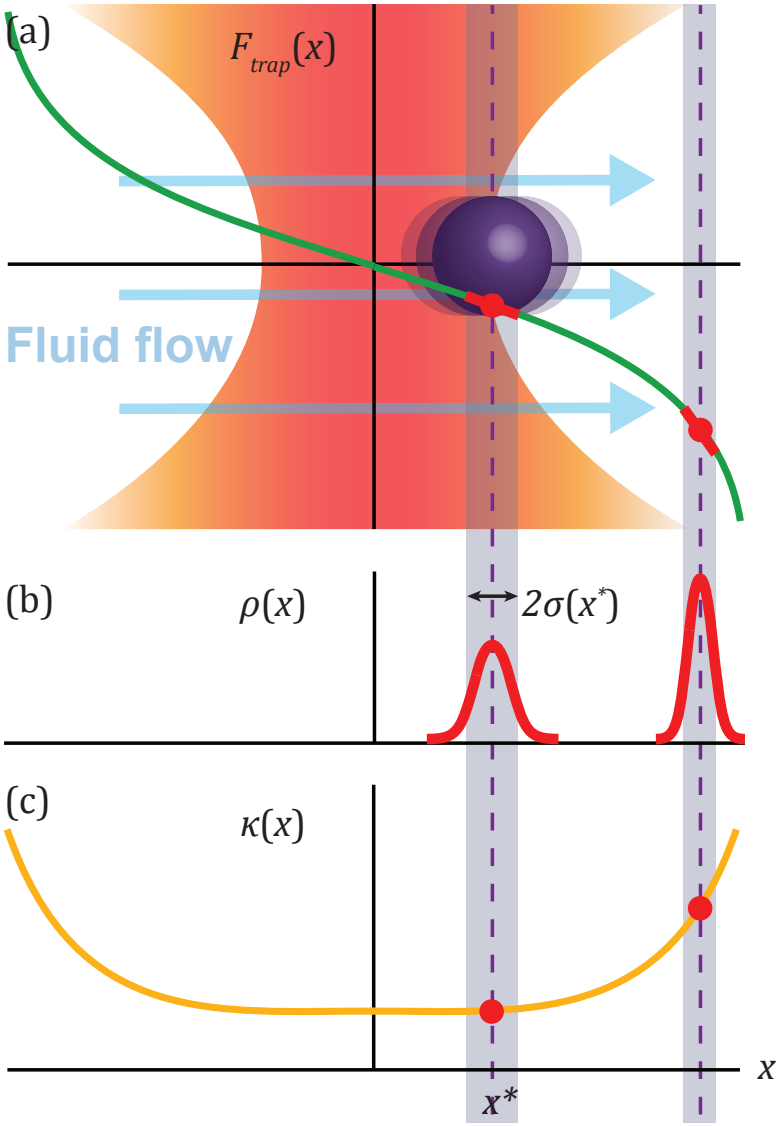

Figure 4.4: (a) Optical trapping force F (green solid line) as a function of the trapped particle position, x. When a constant external force (e.g. fluid drag force) is applied, the particle is displaced from the trap center to a location where the restoring trap force and external force balance. The local trap stiffness $\kappa\,(x^*)$ is equal to the slope of F vs. x (red line segment) at the displaced position x^*. A typical optical trap contains a harmonic potential near the trap center with an approximately constant κ; beyond this linear force region the trap stiffens. (b) Distributions of thermally-driven particle fluctuations $\rho\,(x)$ about the displaced position x^* (red solid lines.) By measuring the variance of these fluctuations $\sigma\,(x^*)^2$, the local trap stiffness can be determined as a function of x with a resolution of $2\sigma\,(x^*)$ (purple bars). (c) Local trap stiffness $\kappa\,(x^*)$ as a function of x (yellow solid line). The local stiffness of the trap is given by the derivative of its force vs. position profile. Reprinted with permission from [78], Optics Letters.

of the applied external force.

4.2.3 Theory

The key concept of our approach is to shift the average position of the particle in the trap using a constant external force (e.g. a fluid drag force) and then record the fluctuations of the particle around this position [Fig. 4.4(a)]. It is well-known that the thermal fluctuations of a particle in the center of the trap provide a direct readout of the linear trap stiffness [47]. By a similar principle, if the amplitude of a particles fluctuations about its shifted position is small compared to the spatial extent of the stable trapping range, then these local fluctuations provide a measurement of the local trap stiffness at that position [Figs. 4.4(b) and 4.4(c)]. The spatial resolution of the measurement of local stiffness is determined by the standard deviation of the distribution of particle displacements at that position. For applications requiring large trap forces and therefore stiff traps, so the typical amplitude of the fluctuations around an equilibrium position is $\sim$ 5 to 10 nm. In this case, we measure the trap stiffness with a spatial resolution of $\sim$ 10 to 20 nm, much smaller than the typical trap range of $\sim$ 300 nm. Because the stiffnesses are measured directly from the distribution of the particles positions, it is not necessary to know the magnitude of the constant external force that is applied. This is particularly useful when constant fluid flow is used to displace the particle since the exact drag coefficient need not be determined.

In order to describe the distribution of the particle's fluctuations when its position is shifted by an external force, we write the Fokker-Planck equation for the probability distribution $\rho(x,t)$ of finding the particle at position x at time t, namely $\partial_t \rho + \partial_x J = 0$. The probability flux J is given by $J = \dot{x}\,\rho(x,t) - D\,\partial_x \rho(x,t)$, where D is the diffusion constant of the particle and $\dot{x}$ is the net particle velocity caused by the external forces

applied on the particle. Although it is possible to use a variety of methods to apply forces on the particle and shift its position, in our particular experimental set-up we apply a drag force on the particle by moving a feedback-controlled nanopositioning stage at constant velocity $\vec{v} = v_x \hat{x}$. The net motion of the particle is determined by the balance of forces acting on it. Given that the particles motion is overdamped, force balance on the particle reads

$$-\xi (\dot{x} - v_x) + F_{trap}(x) = 0 , \tag{4.1}$$

where ξ is the drag coefficient of the particle and $F_{trap}(x)$ is the position-dependent trap force.

At equilibrium, the net velocity of the particle vanishes and the trap force balances the drag force on the particle. The equilibrium average particle position, x^*, for which the average particle velocity vanishes is given implicitly by Eq. 4.1, namely $\xi v_x + F_{trap}(x^*) = 0$. Once the equilibrium particle position is known, we obtain the probability distribution of the particle position fluctuations around the equilibrium position by integrating the Fokker-Planck equation. If the amplitude of the fluctuations in the particle position around the average position x^* is small compared to the spatial range of the trap (Fig. 4.4), the trap force around x^* can be approximated by $F_{trap}(x) \approx F_{trap}(x^*) - \kappa(x^*)(x - x^*)$, where the local trap stiffness $\kappa(x^*)$ is defined positive and corresponds to the derivative of the trap force at $x = x^*$: $\kappa(x^*) \equiv -dF_{trap}/dx|_{(x=x^*)}$. Using the linear expansion of the trap force around the average particle position x^* as well as the Einstein relation $D = k_B T/\xi$, the equilibrium probability distribution of the particle position, $\rho_{\mathrm{eq}}(x)$, reads

$$\rho_{\mathrm{eq}}(x) = \sqrt{\frac{\kappa(x^*)}{2\pi k_B T}} \exp\left[-\frac{\kappa(x^*)}{2k_B T}(x - x^*)^2\right] . \tag{4.2}$$

The amplitude of the fluctuations around the equilibrium position x^* is given by the standard deviation $\sigma(x^*)$ of the equilibrium distribution (Eq. 4.2) and reads

$$\sigma(x^*)^2 = \frac{k_B T}{\kappa(x^*)}. \tag{4.3}$$

Therefore, the local trap stiffness $\kappa(x^*)$ at x^* can be directly obtained from the amplitude of the particle fluctuations around x^* (Eq. 4.3). It should then be possible to obtain the local stiffness $\kappa(x^*)$ at every point of the trap by simply shifting the equilibrium position of the particle and measuring the distribution of the particles position fluctuations around the shifted position. Once the local trap stiffnesses have been measured at several positions covering the full non-linear range of the trap, and knowing that the trap stiffness is defined by $dF_{trap}/dx \equiv -\kappa$, the full non-linear trap force profile, $F_{trap}(x)$, is given by

$$F_{trap}(x) = -\int_x \kappa(x')\,dx' + C, \tag{4.4}$$

where C is an integration constant set by the condition $F_{trap}(x = 0) = 0$.

4.2.4 Results and Discussion

To experimentally test this approach, a single-beam gradient optical trap was formed by focusing a 1064 nm, 5W Nd:YAG laser (Spectra-Physics) through a high numerical aperture objective lens (Nikon, NA=1.49). A separate, low-power, non-trapping 830 nm laser (Melles Griot) and a position sensitive detector (PSD) (Pacific Silicon Sensors Inc.) were used to detect the displacement of the trapped particle from the center of the detection beam [83]. The voltage signals from the PSD were normalized by total light intensity using custom-built electronics and were calibrated by raster-scanning the trapped particle over a matrix of known positions using a pair of acoustooptic deflectors

(IntraAction) [83]. The radius of the calibrated detection region was typically >300 nm. The output signals were sampled at 100 kHz and low-pass filtered using a programmable filter (Krohn-Hite) at the Nyquist frequency. A sample chamber was created by placing two strips of double-sided tape on a slide, and then securing a #1.5 coverslip on top. A high-viscosity mixture of glycerol, water, and polystyrene beads with a mean diameter of 1.1 ± 0.035 µm (Invitrogen), was flowed into the chamber, and the ends of the chamber were sealed with vacuum grease.

A constant fluid drag force was applied to a trapped bead by commanding a precision piezoelectric nanopositioning stage (Physik Instrumente) to execute a step change in the stage velocity from zero to a constant value, typically in the range 10 to 300 µm/s, which was then maintained for the full range of motion of 100 µm. Upon application of the drag force, the average bead displacement increased before reaching an asymptote at position x^*, where the drag force and restoring trap force balanced [Fig. 4.5(a)]. Typically 40,000 to 200,000 samples of the equilibrium position of the particle were recorded over time, and their equilibrium distribution $\rho_{\mathrm{eq}}(x)$ was fitted with a Gaussian function. The variance of the distribution, $\sigma(x^*)$, was then used to calculate the local trap stiffness, $\kappa(x^*)$, as given by Eq. 4.3. The experiment was repeated for a range of velocities, giving rise to the spatial profile $\kappa(x)$ [Fig. 4.5(b)]. The full non-linear trap profile, $F_{trap}(x)$, was then obtained by numerical integration of the measured spatial profile $\kappa(x)$ (Eq. 4.4) and is shown in Fig. 4.6.

To validate our approach and confirm the accuracy of this new method of calibration, we independently measured the force profile of the trap using the Stokes drag method. To do so, the same displacement data were used, but the fluid drag forces were directly calculated using Stokes law, $F_{drag} = \xi v_x$, and plotted against the mean positions of the bead under the constant external force, allowing us to obtain the spatial force profile directly. Force profiles obtained by the traditional Stokes drag method, and by our new

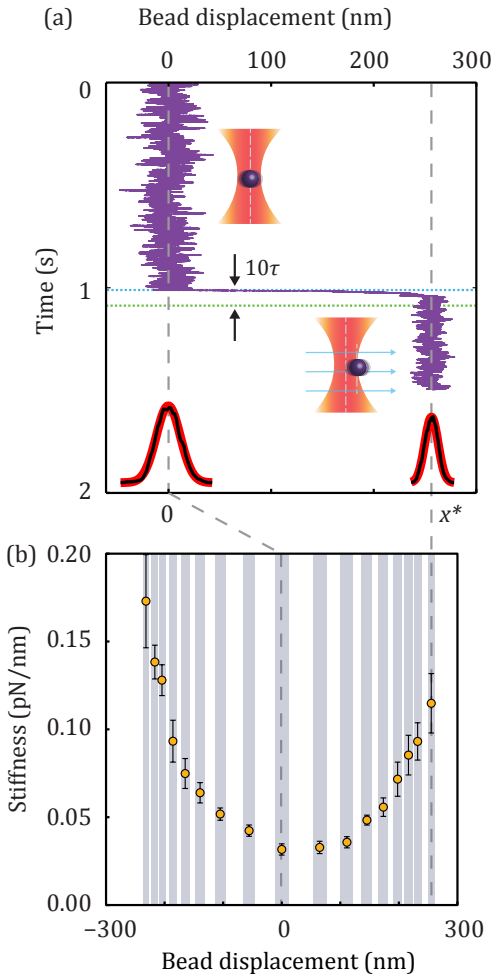

Figure 4.5: (a) Representative example of a raw data trace measured during force calibration (purple line). Starting at time $T = 0$, the position of a trapped particle was measured under no external force. At $T = 1s$, the stage began to move at constant velocity v_x, applying a constant drag force and causing the displacement of the bead to rise to an equilibrium position over a characteristic timescale, τ. In practice, τ was measured for each trace by fitting a piecewise exponential function to the displacement data; we assume that after 10τ the bead has reached its equilibrium position. The data were separated into two segments representing the beads motion under zero or constant external force; for each segment, the distribution of particle displacements was determined and the histogram (shown in black) fitted to a Gaussian function (shown in red) to extract the mean and variance. Each experimental condition was repeated ten times and we report the average local stiffnesses at each displaced position. (b) Local stiffness profile $\kappa\,(x^*)$ (yellow points) of the optical trap calculated from the distributions of bead positions under constant external force (Note that the error bars are smaller than the markers in the x-axis). The resolution at which the stiffness and force profiles can be measured is given by $2\sigma\,(x^*)$ (blue bars). Reprinted with permission from [78], Optics Letters.

method are compared in Fig. 4.6, and show good agreement over the full force range. By calibrating the nonlinear range of the trap, the experimenter can take advantage of a higher maximum trap force, as well as an extended displacement range. As shown in Fig. 4.6, we measure an enhancement of approximately 120% between the maximum force of the linear range (within ± 100 nm of the trap center) to the maximum force of the nonlinear range (± 230 nm).

For the purposes of validation, we obtained the drag coefficient ξ by fitting the power spectrum of the beads fluctuations in the trap center (with no applied external force) to a Lorentzian function using maximum likelihood estimation as described in [84]. Alternatively, the drag coefficient can be estimated using $\xi = 6\pi\eta r$, where r is the bead radius and η is the fluid shear viscosity. When the bead is held within a few radii of the coverglass surface there is an additional correction to the drag coefficient, which has a highly non-linear dependence on the height of the bead above the coverglass surface [47]. This distance is difficult to measure and as a consequence, introduces considerable errors in the determination of ξ. The Stoke's drag method also assumes that the drag coefficient remains constant throughout the experiment, which may not be the case as the bead is moved through regions of varying temperature or surface roughness. In particular, the solution viscosity may be sensitive to temperature gradients around the focused laser [85].

By contrast, our method of obtaining the force profile from only the position fluctuations of the trapped particle requires no knowledge of the drag coefficient, avoiding these issues altogether. We do require an estimate of the system temperature to calculate k_BT, however this is fairly insensitive to temperature fluctuations. With our new method, a change from $20°C$ to $25°C$ (293 to 298 K) results in only a 2% uncertainty in the stiffness measurement; by contrast, the same $5°C$ change causes a 12% change in the viscosity of water corresponding to a 12% uncertainty in the forces calculated in the Stokes drag

method. These viscosity changes can be even larger in other fluids, *e.g.* glycerol.

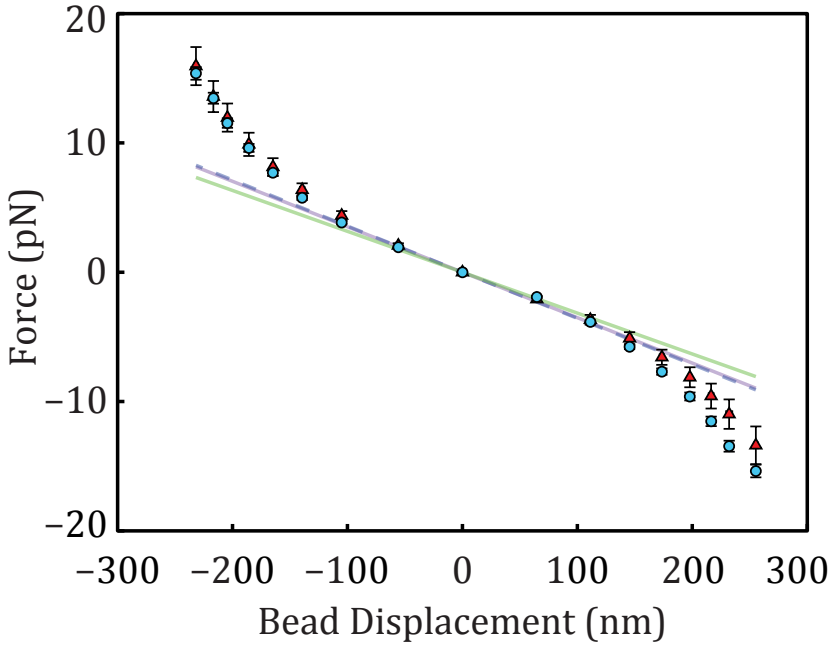

Figure 4.6: Force profiles obtained from new calibration method (red triangles) compared to traditional Stokes drag method (blue circles). In the Stokes drag method, forces are equal to the external fluid drag forces applied to the bead. In the new method, forces are calculated by measuring the local trap stiffnesses as a function of bead displacement and integrating. (Displacement error bars are smaller than the figure markers). Linear stiffnesses were measured at the trap center with no external force and then extrapolated into the nonlinear range using the equation $F_{linear} = \kappa_{linear} x$: traditional Equipartition method (purple line), in which the stiffness is found from a long measurement (typically 10 trials of 100s each) of the particle's thermal fluctuations under no external force, Power Spectrum method (blue dashed line), in which the stiffness is found by using the same data to calculate and fit the particle's power spectrum, and new method (green line), which uses the same calculation as the Equipartition method on our particle position data before the constant drag force is applied (typically using 20 trials of 1s of data each) (see Fig. 4.5(a)). Reprinted with permission from [78], Optics Letters.

In summary, the method we describe allows robust measurement of the nonlinear force profile of the trap and allows the experimenter to easily and accurately extend the force and displacement range of an existing single-beam optical trap. Direct measurement of the entire trap force profile avoids extrapolation of the linear range past its valid boundary

and can account for minor asymmetries in the trapping beam. In contrast to prior methods, our approach does not require independently calibrated forces or knowledge of the size of the trapped particle, fluid viscosity and height of the bead above the surface, simplifying considerably the calibration procedure. Our method works best when the local trap stiffness is reasonably high, and therefore the extent of the particle fluctuations $\sigma(x^*)$ is small, providing good spatial resolution of the trap force profile. Although a stiff trap provides good spatial resolution of the force profile, in this regime, the amplitude of the fluctuations from background sources (*i.e.* mechanical vibrations and electronic noise) can compete with that of the desired particle fluctuations, so care must be taken to identify and eliminate possible sources of undesired fluctuations for best results.

Funding. National Science Foundation (NSF) (CMMI-1254893, MCB-1329722).

Acknowledgments This project made use of the UCSB MRL Shared Experimental Facilities supported by the MRSEC Program of the NSF under Award No. DMR-1121053; a member of the NSF-funded Materials Research Facilities Network. Special thanks are extended to the technical staff of Physik Instrumente and IntraAction.

4.3 Using the Fluctuations Method in Low-Viscosity Fluids

Our newly developed nonlinear calibration method that we described in Section 4.2 allows an experimenter to extend the force calibrations of an optical trap to include its nonlinear range, thereby increasing the maximum trapping force that the instrument is able to measure and apply, without requiring any hardware modifications, and without needing to determine the sample chamber's viscosity, the particle's size, or the stage velocity. Only an estimate of the sample chamber's temperature is needed.

However, in order to perform the Fluctuations calibrations, the experimenter needs to apply a drag force up to the maximum trapping force in order to probe the farthest extent of the trap. This can be challenging when trapping particles in water, where the viscosity is very low. Consulting the Stokes' drag force $F = 6\pi\eta rv$, we see that the only way to make up for a low drag coefficient is either a larger particle or a higher velocity.

Many optical trapping setups use precise piezo stages to perform fine PSD calibrations (see Section 2.3.5). Our PI 517 stage performed this function well, but its maximum velocity was only 350 microns/s. With this stage, using a 1-micron diameter particle in water, the maximum drag force we could apply was about 3 pN. Instead, we used a mixture of glycerol and water to increase the viscosity.

It can be a hassle to increase the velocity capabilities of a optical trapping setup, and it would be highly beneficial if experimenters did not have to make hardware changes in order to use our Fluctuations method. In addition, in vitro experiments involving motor proteins must be done in a water-based buffer.

Even if the experimenter were to install a stage with higher velocities, the signal to noise ratio of the measurement decreases as the trap force increases, due to the reduced magnitude of the particle's fluctuations in the stiffer trap. For very high laser powers, the accuracy of the calibration decreases significantly.

4.3.1 Theory

In this chapter, we present a method for circumventing this issue. We hypothesize that the optical trapping forces at each displacement from the trap center should scale linearly with the linear stiffness at the center of the trap, as is illustrated in Figure 4.7. We expect this to be true because the optical trapping force depends on the intensity gradient of our Gaussian laser beam[86] [87]–the shape of the beam doesn't change when

the laser power changes, only the magnitude of the beam intensity. Therefore, the shape of the force vs. displacement curve should only be changed by a constant factor if the power changes. The relationship between force and intensity gradient is described by the Raleigh scattering approximation of the trapping force:

$$F_{trap} = \frac{2\pi}{c} r^3 \frac{m^2 - 1}{m^2 + 1} \Delta I\,(x) \tag{4.5}$$

where F_{trap} is the trapping force, c is the speed of light in a vacuum, r is the particle radius, m is the ratio of refractive indices of the particle and medium, and $\Delta I\,(x)$ is the intensity gradient of the beam as a function of the radial position x.

We predict that we can obtain that constant factor by comparing the more easily obtainable linear trap stiffnesses at high and low powers–if the whole curve should scale linearly with power, then the linear stiffnesses, i.e. the slopes of the curves at the trap center, should also scale linearly with the same scaling factor.

To make use of this property in an experiment, we would lower the trap power to a level where the trapping forces are small enough compared to the drag forces in water, and then calibrate the full nonlinear force vs. displacement curve using our Fluctuations method. We would then raise the trap power to its maximum value and calibrate just the linear stiffness at that high power, then calculate the ratio of the linear stiffnesses at high and low power and use that ratio as the scaling factor with which to multiply the low power trap force curve, thereby determining the shape of the force vs. displacement curve at high trap power:

$$F_{trap}^{HP}(x) = \frac{\kappa_L^{HP}}{\kappa_L^{LP}} F_{trap}^{LP}(x) \tag{4.6}$$

κ_L^{HP} and κ_L^{LP} are the linear stiffnesses of the trap at high and low power, respectively. The trap could then be used to measure and apply forces at its highest power in

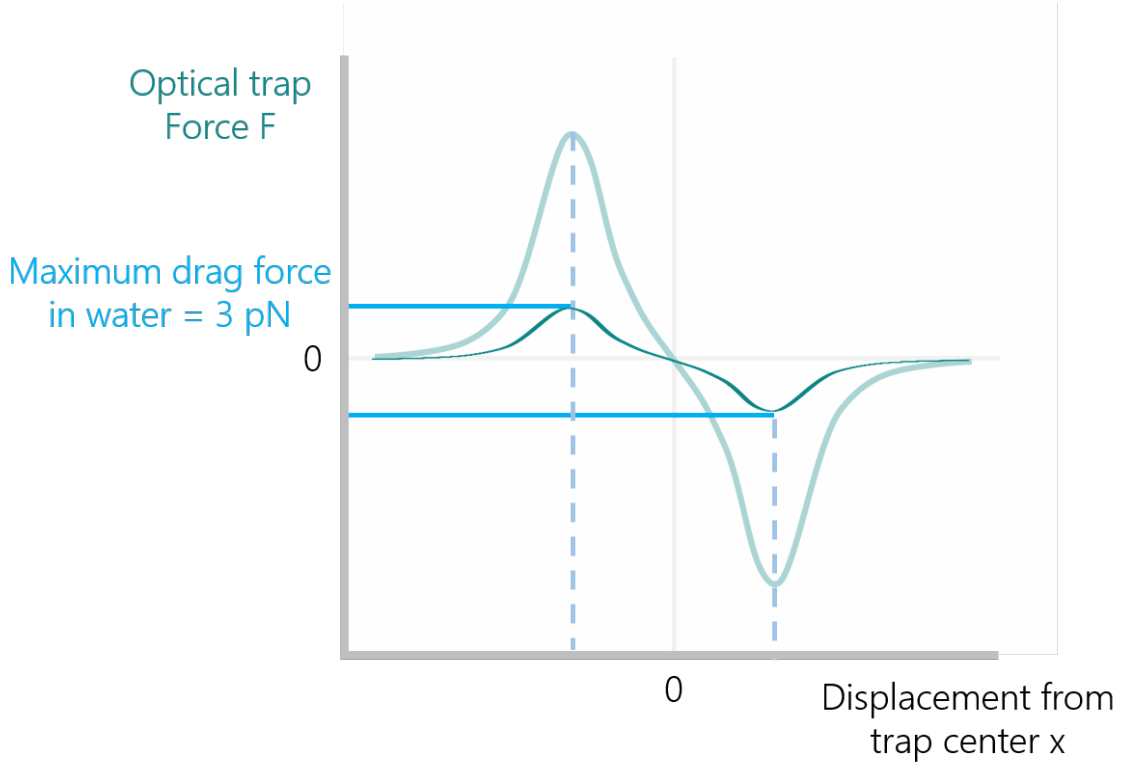

Figure 4.7: Force vs. displacement curve shapes for an optical trap. The theoretical optical trapping force vs. displacement curve has the shape of the derivative of a Gaussian, because the force is proportional to the intensity gradient of the trap. We predict that this shape should scale linearly with power, and that an experimenter could calibrate the curve at low power, then use the ratio of linear stiffnesses to map the low-power shape up to higher powers. The maximum force that our smaller piezo stage can apply to 1-micron particles in water is 3 pN.

water, as the displacement to force mapping has been determined.

4.3.2 Validation

To test this hypothesis, we used 1 micron polystyrene beads in a sample chamber filled with a mixture of about 60% glycerol and 30% percent water. The glycerol raised the drag coefficient of the sample chamber fluid, which allowed us to apply high enough drag forces to probe the entire nonlinear range of our maximally powered optical trap, to compensate for the relatively low maximum velocity of our PI 517 piezo stage. We used

both our new Fluctuations method and the Stokes' Drag method to attempt to confirm our hypothesis using both our new method and a more established method. For both of these calibration methods, we moved the stage at a constant velocity to apply a constant drag force to the bead and to displace it from the trap center by a constant distance. We measured the displacement, and then calculated the trapping force using either the drag force, or by integrating the trap stiffnesses from the variance of the bead's fluctuations.

To compare the force vs. displacement curves of the trap at various laser powers, we used the AOD to set the laser power to 100%, 50%, and 20% of its maximum power. We first set the laser to 100% power, trapped a bead, then ran a LabVIEW vi to perform the stage motions and the measurements for the Stokes' Drag and Fluctuations calibration methods. We then used the AOD to turn down the trap power to 50%, and waited about 20 minutes to allow the equipment and sample chamber to cool and come to equilibrium to avoid observing any transient behaviors due to heat-induced expansion of the optics. We performed the calibrations at 50% power, then lowered the power to 20%, waited 20 minutes, and repeated the calibrations a third time. We held onto the same bead for the calibrations at all three trap powers so that slight differences in bead size or shape would not affect the calibration curve shapes.

Figure 4.8 shows preliminary data suggesting that the trapping force curve is indeed scalable with trap power.

As we mentioned above, these data were collected from beads in a mixture of water and glycerol, but with the faster velocities made available by our PILine stage (see Section 2.4.2) similar measurements could be made in water.

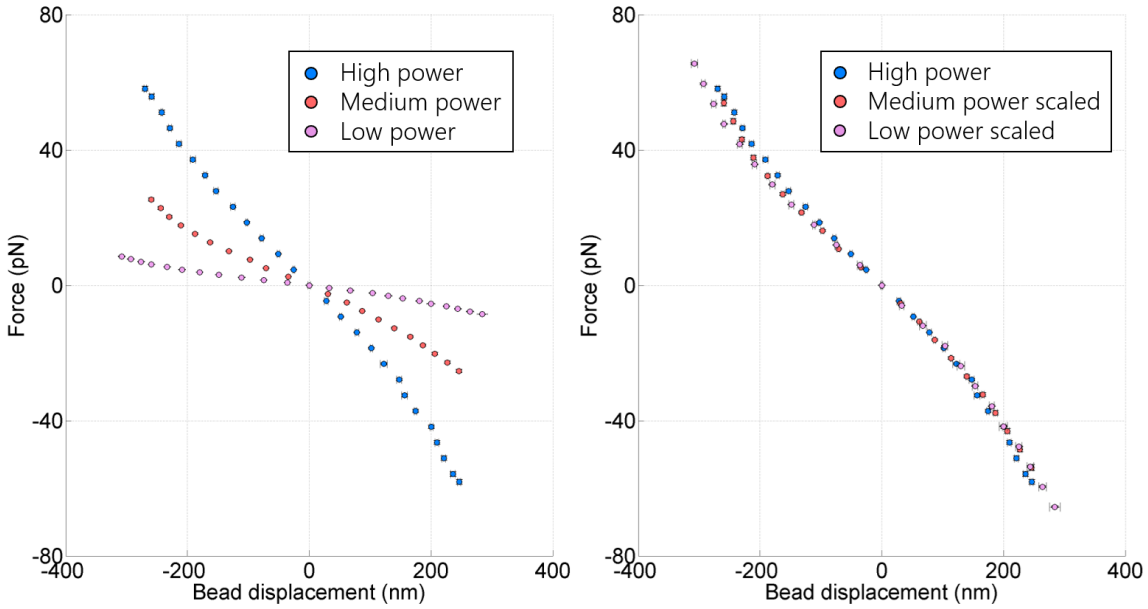

Figure 4.8: Force vs. displacement curves, unscaled and scaled by the proportions of their linear stiffnesses. These data were calculated using the Stokes' Drag method. The scaling factors are 1.9 for the medium power curve, and 5.8 for the high power curve.

Chapter 5

Investigating the Distributions of Diffusion Coefficients

5.1 Introduction

Diffusion has long been a topic of interest for the single molecule community, with a primary focus on two- and three-dimensional diffusion inside cells. One-dimensional diffusion has recently gained attention in the microtubule community due to the discovery that tau diffuses along microtubules[39]. Other studies have demonstrated the diffusion of various molecules along the microtubule lattice, including Myosin Va[88], EB1[40], and charged nanoparticles[89]. Figure 5.1 shows kymographs of the diffusion of single EB1 molecules along microtubules polymerized with GMPCPP provides, produced from fluorescence imaging data by Lopez et al.[40].

In microtubule diffusion studies, particle trajectories are found by tracking the positions of single molecules over time, relative to a particle's starting point. A diffusion coefficient distribution can be obtained by calculating one diffusion coefficient for each particle trajectory, and then plotting those diffusion coefficients in a histogram. There are

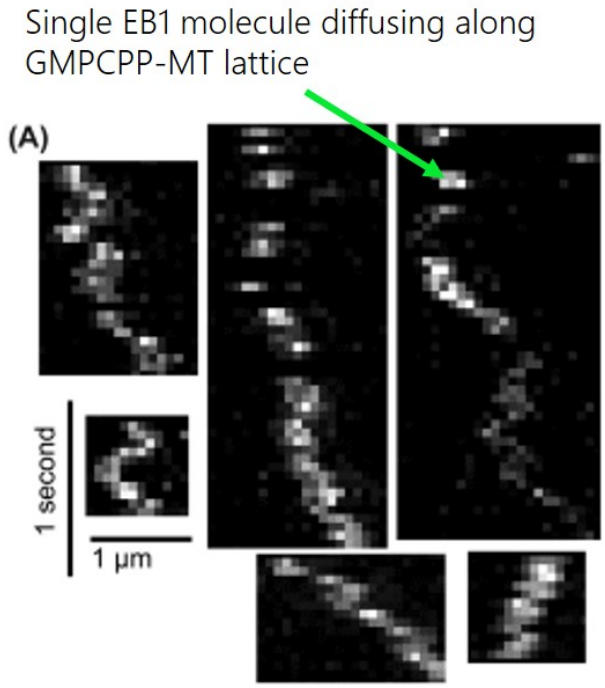

Figure 5.1: Kymographs created by Ben Lopez showing fluorescently-labeled EB1 proteins diffusing along a GMPCPP-polymerized microtubule[40]. Each image represents a different particle trajectory, with the microtubule length represented in the horizontal axis and time represented in the vertical axis. Reprinted from Cytoskeleton **73**(1):23-34 (January 2016), by Benjamin J. Lopez and Megan T. Valentine[40]. Reprinted with permission from Wiley Online Library.

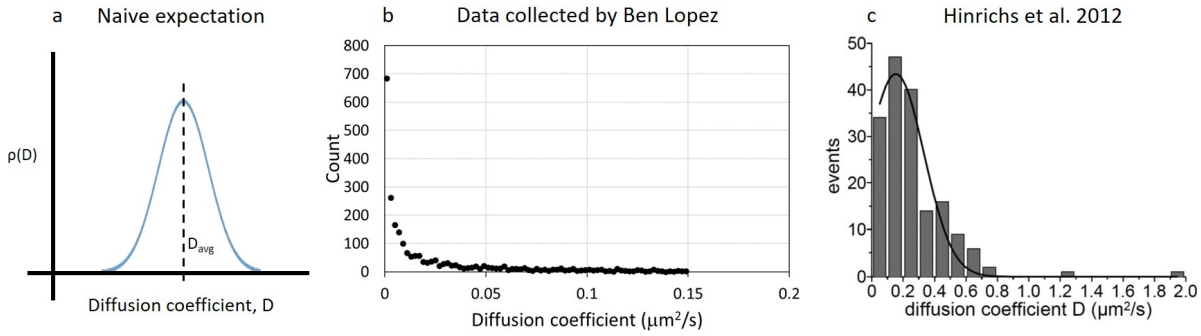

Figure 5.2: Distributions of diffusion coefficients can be plotted when a diffusion coefficient is calculated for each particle trajectory in a data set. a. As a first naive guess, we expected that the shape of the diffusion coefficient distribution would be Gaussian; however this shape is not reflected in b. experimental distributions obtained by Ben Lopez (unpublished data) and c. Hinrichs et al., 2012[39]. Figure 5.2 c. was originally published in the Journal of Biological Chemistry. Maike H. Hinrichs, Avesta Jalal, Bernhard Brenner, Eckhard Mandelkow, Satish Kumar, and Tim Scholz. Tau Protein Diffuses along the Microtubule Lattice. J. Biol. Chem. 2012; 287:38559-38568. ©the American Society for Biochemistry and Molecular Biology.

a number of ways to calculate a diffusion coefficient from a particle trajectory, which will be described in detail in the following sections. Without making any specific assumptions about the diffusing system, it seems not unreasonable to expect that the distribution of diffusion coefficients would be normally distributed, simply because experiments often obtain Gaussian distributions from measured independent random samples. However, the distributions of diffusion coefficients reported in studies in which single molecules diffuse on microtubules typically look somewhat exponential[39] [90]. Figure 5.2 shows two such plots of diffusion coefficient distributions.

These data inspire the question: why aren't the distributions Gaussian? Can the shape of the diffusion coefficient distribution tell us something about the underlying biological system? On the other hand, could the non-normal distribution be caused by experimental noise, analysis artifacts, or the stochastic nature of the motion?

Furthermore, there are many different methods, tools, and analysis choices used when

calculating diffusion coefficients and their distributions, but a clear guide detailing which techniques should be used under which circumstances does not exist. It would be of particular interest to experimenters to have a road map for the best analysis practices to use when experiments yield limited numbers of trajectories, time steps, or both.

It is believed that the microtubule associated protein tau can transition between weakly-bound and strongly-bound states on the microtubule[39], in which the proteins are either diffusing or static. The switching dynamics of tau are important to understanding the biological functioning of these systems, and the ability to distinguish these different states is critical to these investigations. It would therefore be enlightening to know under what conditions an experimenter can resolve two distinct underlying populations of diffusion coefficients.

We attempt to address these questions through both analytical approaches and simulations, and we focus on understanding the methods for obtaining an estimate of the diffusion coefficient of a system. We find that the distribution of diffusion coefficients is not necessarily Gaussian, but arises from Gamma-distributed mean squared displacements.

5.2 Background

5.2.1 Diffusion Coefficient

Diffusion is the random process by which freely moving particles tend to spread out over time, for example aroma molecules in air, or dye molecules in water. The diffusion coefficient characterizes how quickly the molecules tend to spread, and is given in units of distance squared per time, for example $\frac{nm^2}{ms}$.

Figure 5.3a shows the trajectories of 100 simulated diffusing particles. Over time,

some particles remain close to their starting position, while others end up far from the starting point; however, in pure diffusion the average displacement of an ensemble of particles is always zero, as evidenced by the constant mean of the particle position distributions at different time steps in Figure 5.3b. The particle position distributions tend to spread out over time, as particles have more chances to explore farther from their starting places. This process is analogous to flipping a fair coin–any particular sequence of coin flips is equally likely to occur, although there are many sequences that produce equal numbers of heads and tails, and only fewer sequences that produce nearly all heads or all tails. Our particle steps are like coin flips: with each new timestep, the particle is equally likely to take a step forward as it is to take a backward step. Any particular particle trajectory is just as likely to occur as any other, but there are more sequences of steps that will lead the particle back to a position of zero than there are sequences that will lead the particle very far from the starting position, which is why the distribution of particle positions increases toward the zero position. The distribution of particle positions at any point in time is Gaussian.

In a purely diffusive system, the variance of the distribution of particle positions increases linearly over time, which is expressed by the relation

$$\langle x^2 \rangle = 2dDt \tag{5.1}$$

where d is the number of spatial dimensions that the particles can diffuse in, t is time, and D is the diffusion coefficient. Thus, the diffusion coefficient is defined as the constant that characterizes the magnitude of the increase in variance over time—the "speed" of the spread.

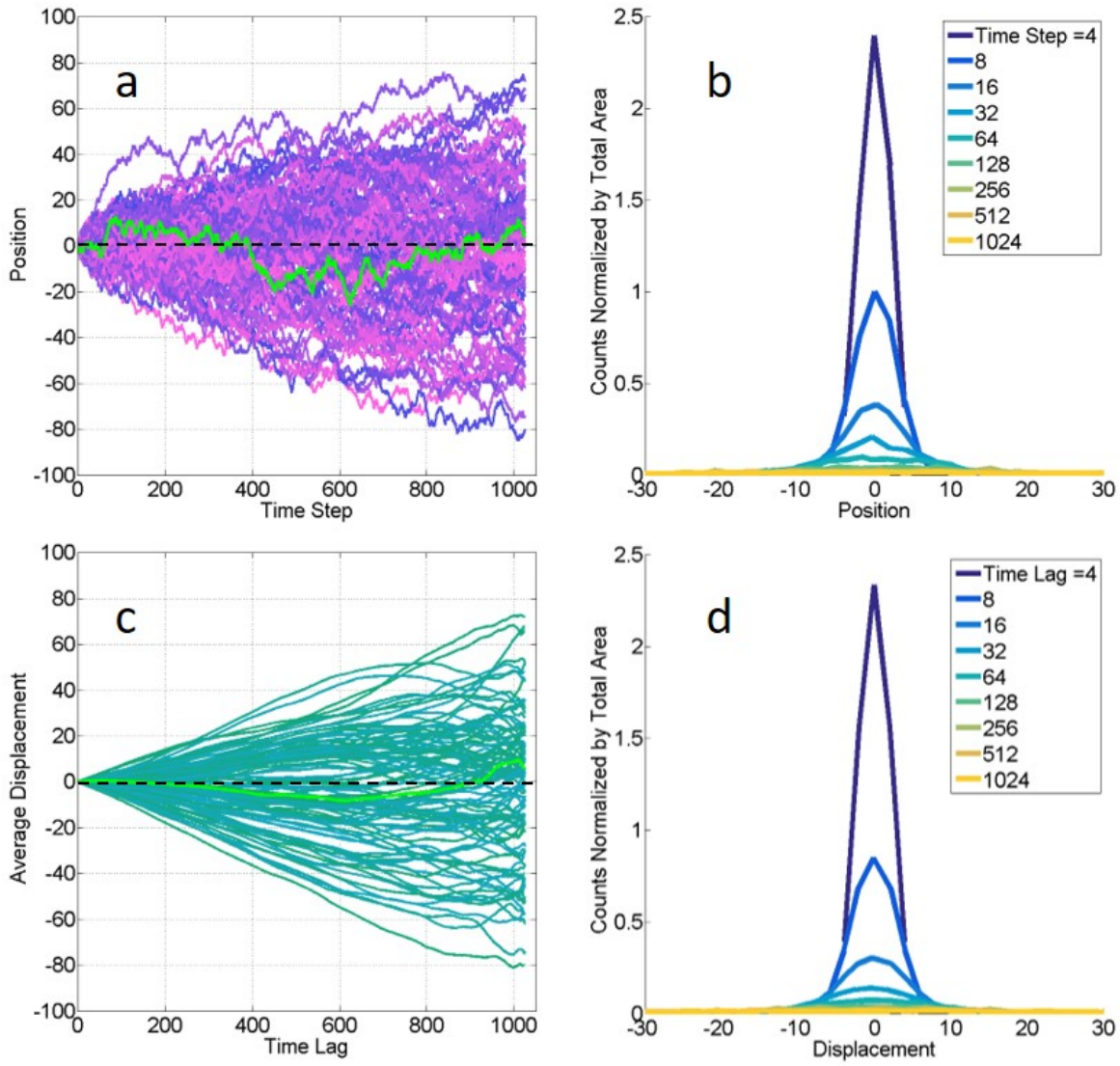

Figure 5.3: Caption appears on following page.

Figure 5.3: Example simulated particle positions and displacements, with 1025 time steps, 1024 trajectories, and using the fully overlapping binning scheme (see Section 5.3). Plots a. and c. only show the first 100 trajectories to simplify the visualization, but plots b. and d. were created using all trajectories. Dashed black lines in a. and c. are included to help the eye compare the highlighted curves to the zero gridlines. a. Discrete particle positions plotted as a function of the simulated time steps. A random trajectory is highlighted to show that, while the ensemble distribution of particle positions spreads out over time, individual particles can lead winding trajectories because each unique collection of particle steps is equally likely to occur. b. Distributions of particle positions plotted at several different time steps. The particle position distribution tends to spread out over time, and the diffusion coefficient is used to characterize that spread, as described by Equation 5.1. c. Average particle displacements plotted against time lag (see Section 5.2.2 for a description of displacements) Each time lag is associated with many displacements, so these are averaged together to obtain one average displacement value for each time lag. The highlighted average displacement vs. time lag curve is atypical, but illustrative, in that it exhibits different behaviors on different time scales: its average displacements are close to zero for short time spans (lag of 0 to about 200), slightly negative average displacements at medium time scales (lag of about 200 to 900), and positive average displacements at long time scales (lag of about 950 to 1024–the particle ended up at a positive position, which is a net positive displacement from it starting position of zero.). By following some of the other average displacement vs. time lag curves, we can see that most of the particle trajectories have either positive or negative average displacements at all time scales. d. Distributions of particle displacements plotted at several different time lags. Note that ALL particle displacements, not the average displacements, were used to calculate these distributions. The variance of the displacement distributions is also characterized by the diffusion coefficient, as described by Equation 5.4. (Note that in b. and d. histogram count values of 0 were removed for plotting, to make the distributions easier to visualize. Due to the discrete nature of the simulations, there are positions and displacements that particles cannot reach at any particular time step (odd or even positions or displacements cannot be reached at even and odd time steps, respectively). These zero values are not representative of the true distributions of the position and displacement histograms, and only make it difficult to see the underlying Gaussian distributions.)

5.2.2 Mean Squared Displacement

The term displacement generally means the difference between a starting and ending point. In diffusion, we can refer to a number of different types of displacements, which can be confusing without proper context. When we talk about the displacements in

the Mean Squared Displacement (MSD), we are talking about the distances between the positions occupied by a particle in one single trajectory. One way to find displacements is to take the differences between the particle's starting point and the particle's position at each moment in time. In this way, we would get one displacement for each time point. However, we don't have to limit ourselves to using the particle's starting point as the reference for all displacements. Instead, we can think of the particle's trajectory as lots of min-trajectories stitched together. For example, we can divide the particle's trajectory into segments of equal lengths of time, and obtain many displacements for each length of time used by finding how far the particle moved in that amount of time. In other words, we take the beginning of each segment as a starting point, and find out how much the particle was displaced in the amount of time defining the segment. We call the time lengths "time lags" or "lags" and denote them with the symbol τ. Figure 5.6 illustrates the segmenting of a particle trajectory into non-overlapping segments or bins.

For small lags, we can divide a trajectory into many segments, and obtain many displacements for each lag, for example imagine dividing a 10-second-long trajectory into 5 portions of 2 seconds each, obtaining 5 different displacements. As the time lag gets larger, the number of displacements we can obtain decreases, for example if we divide the 10-second-long trajectory into 5-second-long segments we can only get two of those segments. We can also overlap the time lag segments to get more displacements by using different binning schemes, which we explain in detail in Section 5.3.2 and Figures 5.4–5.6.

The calculation of MSD as a function of lag, when using fully overlapping segments, is described by the equation:

$$MSD = \langle \Delta x^2(\tau) \rangle = \frac{1}{N} \sum_{i=1}^{N} \left[x\left(i\Delta t + \tau\right) - x\left(i\Delta t\right) \right]^2 \tag{5.2}$$

for time lags of $\tau = m\tau_{min}, m = 1, 2, 3, ...M$,

where x is the particle position, τ is the time lag, τ_{min} is the smallest time lag value, m is the discrete lag or lag index, i is the index of the time step, Δt is the time increment of one time step, and N is the number of overlapping segments that the trajectory can be cut into at lag index m (N = number of discrete time steps - m for fully overlapping bins). The time lag τ in actual units of time is equal to the discrete lag m multiplied by the amount of time spanned the minimum lag, τ_{min} (and τ_{min} is often set equal to the time of one time step, Δt). For fully overlapping bins, the largest possible lag index, M, is equal to the number of time steps - 1.

For each trajectory, we obtain one Mean Squared Displacement for each time lag. To do this, we pick a time lag, and divide the trajectory into equal portions each having duration equal to the time lag. We calculate how far the particle moves during each time segment, and obtain one displacement for each segment. We then square each displacement, add them all up, and divide by the number of segments we had. Again, each time lag will produce a different number of segments, and we must divide the sum of squares of the displacements by the corresponding number of segments. To summarize, the MSD is obtained by calculating the *mean* of many *squared displacements*.

We repeat this process for many different time lags of increasing durations, and obtain a list of MSD values corresponding to the lags. Often in experiments, observation techniques such as imaging provide a natural discretization of time that is used to decide which time lags to use. For example, for a camera frame rate of 20 frames/s, a natural minimum lag time to choose would be the camera frame time, or 0.05s, and multiples of 0.05s would then be used as larger lags.

The MSD has units of distance squared, for example nm^2. MSD is analogous to the variance of the particle position distribution, in that it is related to the diffusion

coefficient through the equation:

$$MSD = 2dD\tau \tag{5.3}$$

where τ is the time lag, and d and D are again the dimensions and diffusion coefficient, respectively.

We can also think of the MSD as the spread of the displacements over time, which also increases linearly with time, according to the relation:

$$\langle (\Delta x)^2 \rangle = 2dD\tau \tag{5.4}$$

where Δx represents displacement. An illustration of the displacement spreading is shown in Figure 5.3 b and c. As one would expect, the variance of the displacement distributions at various time lags is also equal to $2dD\tau$.

Equation 5.3 implies that one could plot MSD vs. time lag, and obtain an estimate of the diffusion coefficient D from the slope of the line. While strictly speaking this is true, MSD is an ensemble property, which means that its relations are only accurate when we look at enough data. An experimenter needs to obtain either a very long trajectory and have many displacements to average together, or must average together MSD vs. τ curves from many different trajectories, in order for Equation 5.3 to hold with reasonable accuracy.

In Figure 5.7 a, MSD vs. τ plots from simulated single trajectories with 1024 time steps do not appear particularly linear (see Section 5.3 for details on how these simulations were performed), and the single molecule experiments we discuss in this chapter typically have far fewer data points due to measurement limitations. Note also that MSD curves are bound to appear less linear with increasing lag because the number of displacements of length τ necessarily decreases, which makes the MSD at large lags less averaged.

This inaccuracy is not, however, due to any measurement noise, but rather to the underlying stochastic nature of diffusive processes. Although the ensemble follows particular relations, individual particles will have widely varying trajectories, and it is only by averaging many displacements, trajectories, or both, that the ensemble relations become accurate.

5.2.3 Single Molecule Particle Tracking

Measuring the diffusion coefficient of single molecules diffusing on microtubules is exceedingly difficult. Fluorescence microscopy is used to measure a signal coming from a labeled particle as it moves along the microtubule lattice. Thanks to advanced cameras and averaging techniques, typical localization errors in particle positions are on the order of 10 to 40 nm. However, the number of measurements obtainable is quite small, due to photobleaching and particles unbinding from the microtubule. For example, Lopez's experiments were performed with a camera frame rate of 20 frames/s, and particle trajectories up to about 1 s long were measured[40]. This produced only 20 frames of data to work with.

The time consuming nature of these measurements limits the number of particle trajectories an experimenter can reasonably obtain. Lopez obtained an astounding number of trajectories: between 450 and 1700 trajectories for each different set of microtubule conditions that were studied.

The fields of Fluorescence Photobleaching Recovery (FPR) and Fluorescence Correlation Spectroscopy (FCS) deal with similar data collection challenges as Single Particle Tracking (SPT). Elliot L. Elson notes that "Because of its stringent requirements for stability of sample and measuring system and the long periods required for data accumulation, FCS is generally more difficult to use than is FPR and is typically unsuitable

for measurements on living systems such as cells in culture."[91] Qian et al. argue the advantages of SPT over FPR and FCS for measurement of diffusion coefficient in cells, pointing out that SPT allows the experimenter to observe qualitative changes in single particle behavior, such as when a particle moves over regions of varying "roughness"[92]. With regard to amount of data required for a good measurement, Petersen invokes a figure-of-merit for the fluorescence intensity that is proportional to the square root of the number of data points collected[93]. Qian notes that uncertainties in FCS measurements are inversely proportional to the number of measurements[94].

5.2.4 Prior Studies on Diffusion Coefficient Distributions

In 1997, Michael Saxton used simulations to study the distributions of the diffusion coefficients calculated from single particle trajectories diffusing in two dimensions[95]. Saxton was interested in whether the distributions of diffusion coefficients of proteins and lipids diffusing in the cell membrane might reflect the heterogeneity of the membrane. He estimated diffusion coefficients by simulating diffusing particles, plotting each particle trajectory's MSDs vs. time lags curve, fitting a line to each curve, and calculating D from the line's slope. In this way Saxton obtained one diffusion coefficient for each particle trajectory.

While Saxton was primarily concerned with the effects of obstacles on diffusion in cells, his work shows that the distributions of diffusion coefficients even in unobstructed 2D diffusion are not always Gaussian (See Figure 5.10 a), and that the shape of the distribution changes with both number of time steps simulated and number of lags used when fitting lines to the MSD curves. Saxton's plots show that the distribution shape seems to morph continuously from Gaussian into a shape reminiscent of a lognormal distribution. Saxton's diffusion coefficients displayed in Figure 5.10 a) were calculated by

fitting lines to the MSD vs. time lag curves of individual simulated particle trajectories, without weighting the fit or forcing the y-intercept to zero.

Saxton did not, however, provide an explanation for why the distributions appear in these alternate shapes, but he wrote that "Wade et al. (1989) found the distribution of D to be lognormal and used the geometric mean as the value of D."[95] Wade, in the aforementioned paper, writes "The values of D_{lat} [the lateral diffusion coefficient in B lymphoma cells] typically are not a normal distribution. Accordingly, geometric mean D_{lat} were calculated from normally distributed lnD."[96] Again, no explanation is given for why the distribution of diffusion coefficients should be non-Gaussian, or lognormal in particular.

5.3 Diffusion Simulations

To investigate these questions, we performed simulations to model diffusion. In this way we were able to show what a pure diffusive process should look like in the absence of measurement noise, and to clearly visualize the underlying relationships between particle positions, mean squared displacements, and diffusion coefficients.

5.3.1 Simulating Particle Trajectories

The basic rules of the simulation are simple: we create a fixed number of evenly-spaced time steps, and allow a particle to take one step either forward or backward with each time step. The particle is equally likely to take a backward step as it is a forward step. The particle is not allowed to sit still during a time step–it must take one discrete step with each time step. The cumulative displacements from the starting position that the particle reaches by taking its discrete steps are known as the particle's 'positions'. The collection of the positions that the particle reaches over the time steps are referred

to as the particle's 'trajectory'. We simulated many different particle trajectories for our analyses.

We simulated particle trajectories in MATLAB, using MATLAB's random number generator. First, we generated a uniformly distributed random binary matrix, in which each matrix element is either a 1 or a zero (with equal probability). We designated the rows of the matrix as representing individual particle trajectories, and the columns as representing time steps of the trajectory. The 1 values in the matrix represented particle steps forward, and the 0s represented steps backward. We use the shorthand names NTraj to indicate the number of particle trajectories used in an analysis, and NT to mean the number of time steps used in each trajectory.

We generated a large file of random binary data with 10 000 x 10 000 elements, and saved it to the disk. In this way, we can use the same data repeatedly without having to generate new trajectories each time, and we can compare how different analysis methods work on the same data set. We also cut this data into subsets: for example, for our studies we used only the first 1024 trajectories and the first 1025 time steps. This gives the option in the future to run a new analysis that uses more trajectories and time steps; because we made use of the same data as in the smaller analysis, we would be able to compare the results as though we had simply added more particle trajectories to our data set. This would be analogous to an experimenter asking the question "what would my results look like if I observed additional particle trajectories or steps and added them to my data set?"

To convert our binary data into particle trajectories, we first converted all of the 0s in the matrix to -1s. Next, we replaced the entire first column of the matrix (i.e. the first time step of each trajectory) into 0s. We did this for analysis convenience, to give each trajectory a common starting position of 0. (Note that we used 1025 time steps to ensure that each trajectory would have 1024 displacements of time lag = 1 with respect to the

particles' starting position of 0.) Next we transformed the particle steps into particle positions (relative to the starting point of 0) by calculating the cumulative sum of the steps along the columns of the matrix. For example, if the first five particle steps of a trajectory were [+1 -1 -1 -1 +1], then we would replace the first element to zero to obtain [0 -1 -1 -1 +1], and then cumulatively sum the columns to obtain our particle positions: [0 -1 -2 -3 -2]. This example would have 5 rows of particle positions, but the particle would have taken only 4 "time steps" relative to its starting position (see Figure 5.4 for illustrations of time steps, particle steps, and particle positions).

5.3.2 Binning schemes for calculating Mean Squared Displacement

There are several binning schemes that can be used when finding the displacements used to calculate MSD. First, fully overlapping bins can be used, in which all possible displacements that have a duration of the lag time are used (Figure 5.4.) Each lag bin is simply shifted over by 1 time step from the previous bin. Lags up to NT-1 can be used, because the largest lag possible is the time difference between time step NT and time step 1.

Next, half-overlapping bins overlap each other halfway, each bin starting at the last bin's endpoint minus half the bin size (Figure 5.5). With half overlapping bins, only lags of even value are used, because with discrete time steps it would be unclear where to start the next odd-valued bin. Lags up to the nearest even lag less than NT - 1 can be used.

Finally, non overlapping bins do not overlap each other at all (Figure 5.6). Each bin starts at the endpoint of the last bin.

Non overlapping bins have the advantage of being uncorrelated, but they do introduce

a bias. Saxton described this phenomenon in his 1997 study of diffusion coefficient distributions: "...in the average over independent pairs [non overlapping bins], trajectory points are sampled differently depending on how many prime factors the number of the time step has."[95]

Fully overlapping bins, on the other hand, make use of all the data, but are highly correlated. It is possible to account for this oversampling in the calculation of statistical quantities by adjusting the degrees of freedom to dof = 1.4m/j, where m is the discrete time step and j is the discrete lag [97].

5.3.3 Calculating Diffusion Coefficient

The theoretical diffusion coefficient for our simulations can be found from Equation 5.1, using the discrete simulated position and time steps as reference units:

$$D_{sim} = (1 \text{ step})^2 \text{ / } 2*1*(1 \text{ time step}) = 0.5 \text{ steps}^2/\text{time step}$$

where d = 1 because our simulations are 1-dimensional.

In our simulations, we used Equation 5.3 to calculate diffusion coefficients in order to be able to compare our distributions of diffusion coefficients to Saxton's results, and to experimental results found from fitting lines. First, we fitted lines to each MSD vs. lag curve for our simulated particle trajectories and obtained the diffusion coefficient as described by Equation 5.3. We compared line fits to all of the MSD data to lines fitted to only a portion of the MSD data: we fit a line to the MSD vs. lag data from a lag of 0 to a lag of ND, where ND represents the value of the maximum lag used in a particular fit. We also compared the choice to force the -intercept of the fit to be zero or not. Since the true MSD of a trajectory at a time lag of 0 is by definition 0, then we can make the argument that a line fit that accurately represents a particular MSD should also have a value of 0 at a lag of 0. This also holds with the fact that diffusion coefficients should have positive

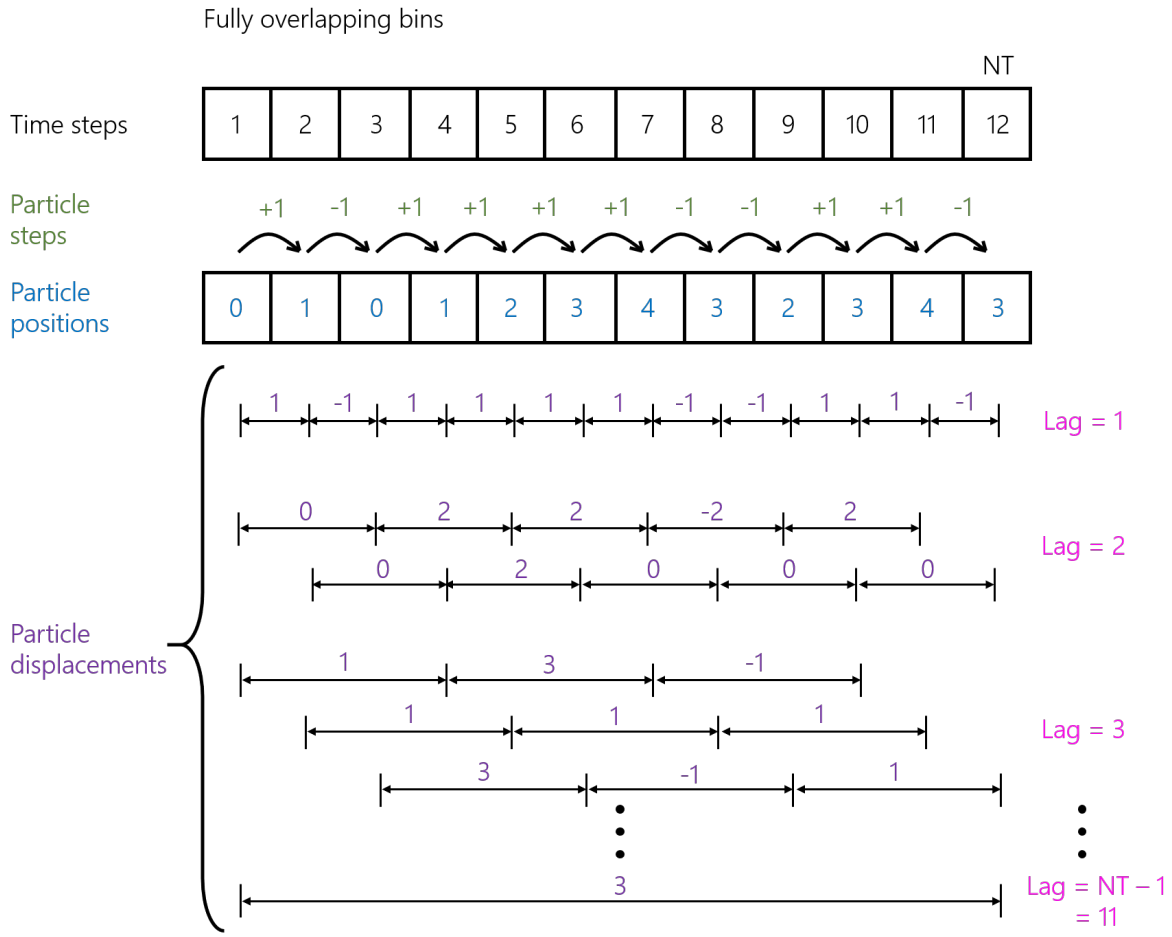

Figure 5.4: Fully overlapping binning scheme. We simulate discrete time steps, and allow each particle to step either forward or backward with each time step. By cumulatively adding the steps, we calculate the particles' positions at each time step, starting each trajectory from the reference position of 0. Particle displacements are then calculated for each integer time lag value. In the fully overlapping binning scheme, we use all possible pairs of positions that are a certain lag apart to find our particle displacements. The displacements are the distance a particle travels during the lag time from any particular starting point. Displacements can have positive or negative values. All integer lags up to the total number of simulated time steps minus one (NT-2) are used in the fully overlapping binning scheme.

values, and when the y-intercept is forced to 0 then the slope of any resulting line fit of MSD vs. lag data must be positive. In addition to selecting only the first portion of MSD data from 0 up to ND, we alternatively selected out only the MSD data at octave

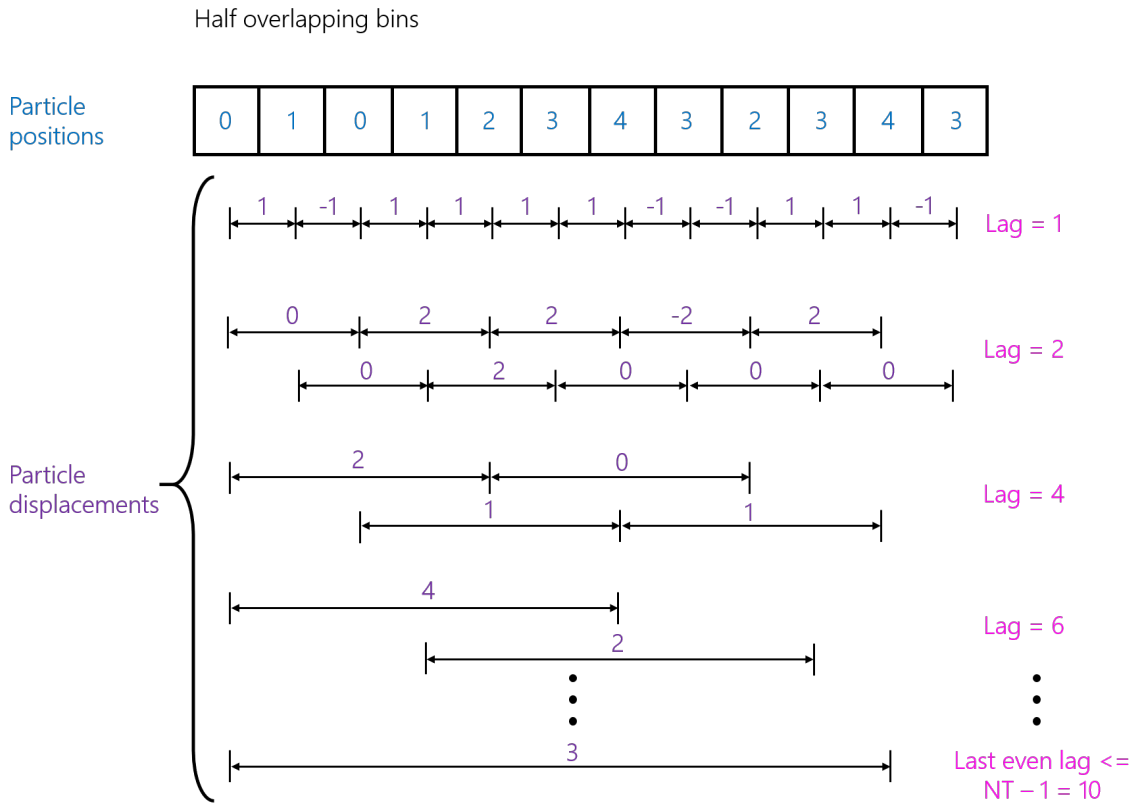

Figure 5.5: Half overlapping binning scheme. In this scheme, bins are only allowed to overlap by half their time length. Because our simulations use discrete time steps, only even-valued integer time lags can be used, as odd-valued time lags would add a lop-sidedness to the overlap. Lags with a value up to the nearest even integer to NT-1 are used.

lags (lags of powers of 2). Octave lags have the advantage of weighting all frequencies of particle motion equally. The line fitting choices and conditions are illustrated in Figure 5.7.

We used these line fitting methods in combination with the various binning schemes described in Section 5.3.2.

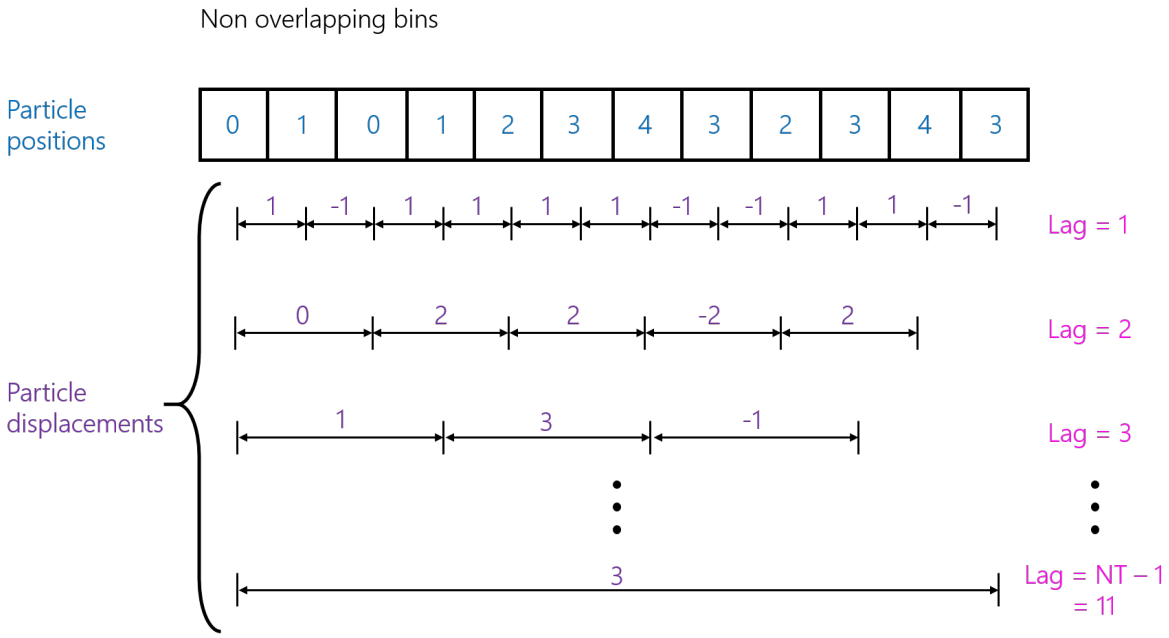

Figure 5.6: Non overlapping binning scheme. In this scheme, the displacements do not overlap, though they do share endpoints. Integer lag values up to NT-1 are used.

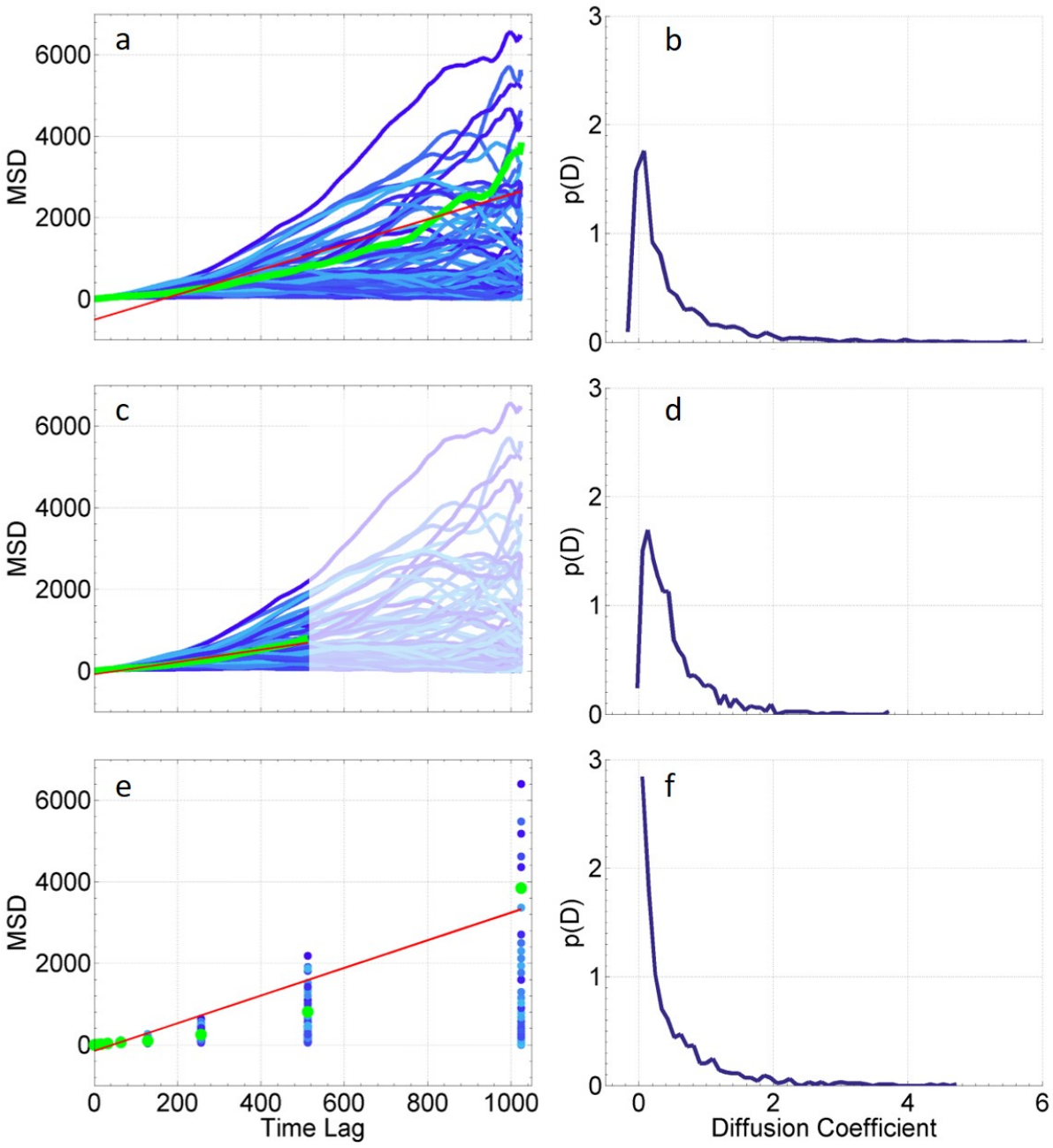

Figure 5.7: Caption appears on following page.

Figure 5.7: Example simulated MSDs and the resulting distributions of diffusion coefficients calculated from line fits to the MSDs, with 1025 time steps, 1024 trajectories, and using the fully overlapping binning scheme. In a., c., and e., only the first 100 trajectories are shown to simplify the visualization, but in b., d., and f., all trajectories are used to calculate the distributions. a. A line is fitted to the highlighted trajectory and its slope is used to calculate D using Equation 5.3. The rest of the MSD curves display a fairly wide range of slopes. b. The distribution of diffusion coefficients obtained by fitting lines to each MSD vs. lag curve. All MSD data up to a lag of 1024 are used, which we notate as ND = 1024. c. MSD data above a lag of 512 are ignored, and lines are fitted to the remaining MSD data. d. Distribution of diffusion coefficients obtained by fitting lines to each trajectory up to a lag of 512, which we notate as ND = 512. e. We show here only the MSD data corresponding to octave lags (lags of powers of 2), and a fit line is shown for the octave lag points of the highlighted trajectory. f. Distribution of diffusion coefficients obtained by fitting only the MSD data corresponding to octave lags. Octave lags up to 1024 are used, so we say that ND = 1024 for this case also.

5.3.4 Verification that Simulations Accurately Model 1D Diffusion

First, we validated the ability of our simulations to accurately model 1D diffusion by plotting histograms of particle positions vs. time and calculating corresponding from Equation 5.1 at time steps 4, 8, 16, 32, 64, 128, 256, and 1024. This process was done for simulations with 1025 time steps and 1024 trajectories. This is a nice first check to do because it is independent of any binning methods, as the MSD has not yet been calculated. We are only looking at how our particles' positions spread out over the simulated time. These histograms are shown in Figure 5.3b. The table in Figure 5.8 shows diffusion coefficients calculated from these particle position histograms, which match the theoretical simulation diffusion coefficient of 0.5 $steps^2/timestep$ within the calculated uncertainty.

We then used MSD data calculated using the fully overlapping binning scheme and plotted histograms of the particle displacements vs. time lag, shown in Figure 5.3d. We

	Diffusion coefficients calculated from particle position data and histograms, with uncertainties. (steps^2/time step)								
Time Step	**4**	**8**	**16**	**32**	**64**	**128**	**256**	**512**	**1024**
D calculated from Gaussian fit parameter	0.5	0.49	0.48	0.52	0.52	0.51	0.65	0.53	0.48
Uncertainty in D from propagated fit parameter uncertainty	0.2	0.04	0.04	0.08	0.07	0.09	0.1	0.2	0.08
D calculated from population variance	0.47	0.46	0.50	0.54	0.52	0.54	0.51	0.51	0.50
Uncertainty in D from propagated standard error of the variance	0.02	0.02	0.02	0.02	0.02	0.02	0.02	0.02	0.02

Figure 5.8: Diffusion coefficients calculated from the distributions of simulated particle positions at various time steps shown in Figure 5.3b., using Equation 5.1. Blue rows: diffusion coefficients calculated from a Gaussian fit to the histograms, with uncertainty propagated from confidence intervals on the fit parameter. Green rows: diffusion coefficients found by directly calculating the variance of the particle position values, with uncertainty propagated from the standard error of the variance. All diffusion coefficients in the table match the theoretical simulated diffusion coefficient of 0.5 $steps^2/timestep$ within their uncertainties, which supports the claim that the simulations have accurately represented diffusive behavior.

calculated diffusion coefficients from each histogram for lags of 4, 8, 16, 32, 64, 128, 256, and 1024, which are shown in the table in Figure 5.9. These diffusion coefficients also match the theoretical simulation diffusion coefficient within the calculated uncertainty.

These two checks show that our simple simulations accurately model diffusive behavior, and that we can extract the simulated diffusion coefficient of 0.5 $steps^2/timestep$ from our simulated particle trajectories.

Another technique that is commonly used to verify diffusive behavior is to plot MSD vs. lag on a log-log scale. A brief discussion of this technique and its results are shown in Appendix B.

5.3.5 Distributions of Diffusion Coefficients

To gain insight into the question of diffusion coefficient distributions, we reproduced one of Saxton's 1997 plots showing how the distribution of diffusion coefficients changes

	Diffusion coefficients calculated from displacement data and histograms, with uncertainties. (steps^2/time step)								
Time Lag	**4**	**8**	**16**	**32**	**64**	**128**	**256**	**512**	**1024**
D calculated from Gaussian fit parameter	0.6	0.53	0.53	0.519	0.51	0.51	0.5	0.5	0.48
Uncertainty in D from propagated fit parameter uncertainty	0.1	0.03	0.02	0.004	0.02	0.01	0.1	0.1	0.08
D calculated from population variance	0.50	0.50	0.51	0.51	0.50	0.50	0.50	0.50	0.50
Uncertainty in D from propagated standard error of the variance	0.02	0.02	0.02	0.02	0.02	0.02	0.02	0.02	0.02

Figure 5.9: Diffusion coefficients calculated from the distributions of simulated particle displacements at various time steps shown in Figure 5.3d., using Equation 5.4. Blue rows: diffusion coefficients calculated from a Gaussian fit to the histograms, with uncertainty propagated from confidence intervals on the fit parameter. Green rows: diffusion coefficients found by directly calculating the variance of the particle displacement values, with uncertainty propagated from the standard error of the variance. All diffusion coefficients in the table match the theoretical simulated diffusion coefficient of 0.5 $steps^2/timestep$ within their uncertainties, which supports the claim that the simulations have accurately represented diffusive behavior.

as the amount of MSD data used decreases[95]. Our reproduction is shown side-by-side with Saxton's results in Figure 5.10. Our figure matches Saxton's with minor differences. Figure 5.10c is a zoomed-out version of the figure which shows the long tail that Saxton's plot cuts off. These diffusion coefficient distributions seem to transition continuously from Gaussian to non-Gaussian.

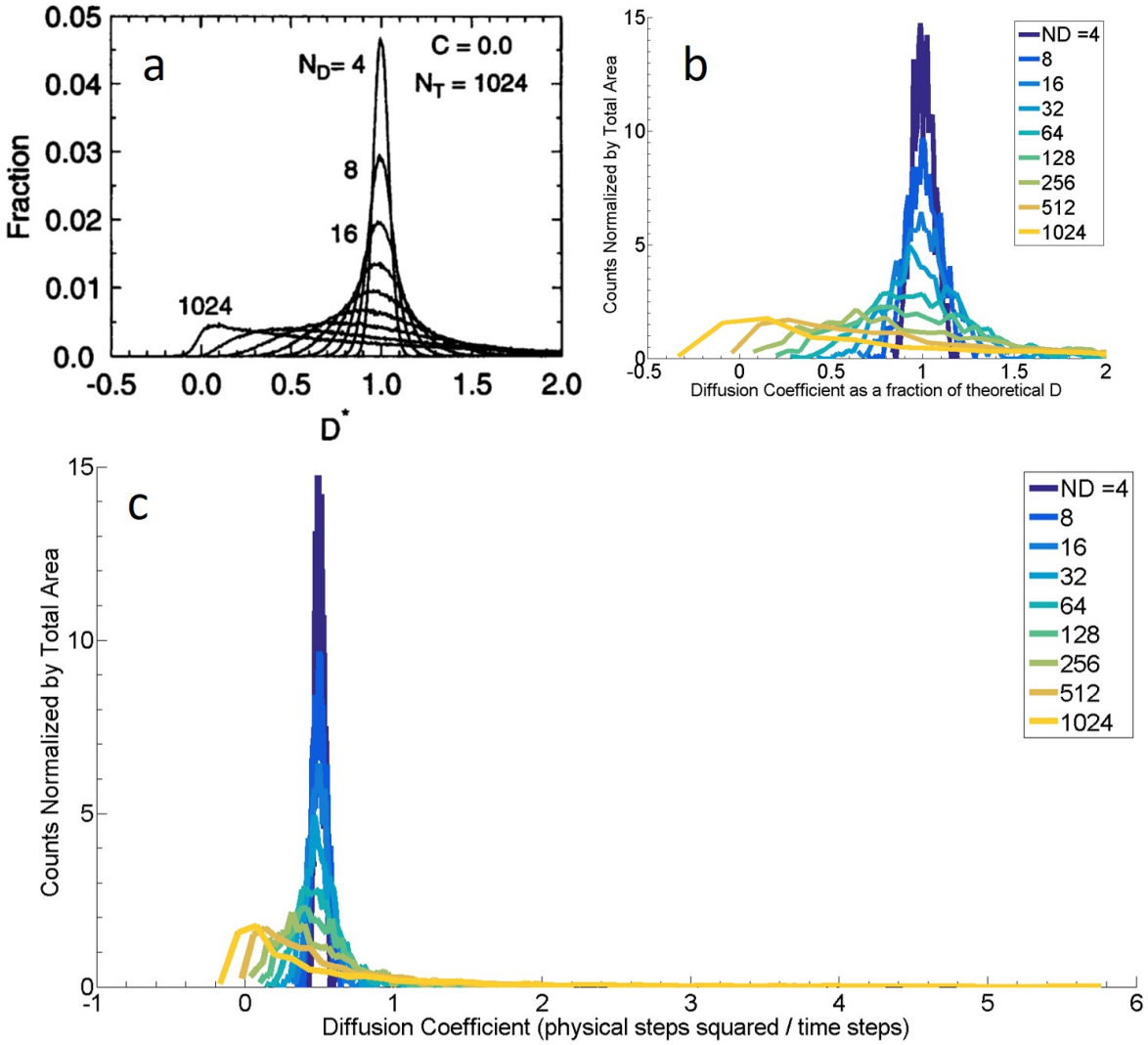

Figure 5.10: Caption appears on following page.

Figure 5.10: Change in diffusion coefficient distributions as amount of MSD data used increases. a. Simulation results from Saxton, 1997[95]. Reprinted from Biophysical Journal, 72/4, Michael J. Saxton, Single-particle tracking: the distribution of diffusion coefficients, 1744-1753, Copyright 1997, with permission from Elsevier. Saxton used 1024 time steps. The number of trajectories used was not stated. Diffusion coefficients were found by fitting lines to MSD vs. lag curves and using Equation 5.3. ND denotes that MSD vs. lag data was used for lags from 0 to ND, when calculating the line fits. The y-intercepts of the line fits were not forced to zero, which is why some diffusion coefficients less than zero were found. The fully overlapping binning scheme was used when calculating MSD, and the line fits were not weighted. The distributions of diffusion coefficients seem to morph from Gaussian to something like a lognormal distribution as ND increases. b. We repeated Saxton's simulation conditions in 1 dimension. We used what we denote as 1025 time steps, which is the same as Saxton's notated 1024 time steps due to a difference in indexing. We used 1024 particle trajectories. We also fitted lines to MSD vs. lag data from lags of 0 to ND, did not force the y-intercepts of the fits to 0, and used the fully-overlapping binning scheme. The diffusion coefficients in this plot are normalized by the theoretical diffusion coefficient of our simulations, $D_sim = 0.5$, to compare to Saxton's simulated diffusion coefficient of 1. c. Zoomed-out version of b., showing the long tails of some of the distributions. This version is unnormalized, showing the absolute diffusion coefficient.

Fully overlapping bins, Y intercept not forced to zero									
ND	4	8	16	32	64	128	256	512	1024
Mean D	0.502	0.504	0.506	0.507	0.502	0.499	0.49	0.50	0.50
STD of D	0.03	0.06	0.06	0.1	0.2	0.3	0.3	0.6	0.6
SEM of D	0.001	0.002	0.002	0.003	0.005	0.008	0.01	0.02	0.02

Figure 5.11: Mean diffusion coefficients directly calculated from the distributions of diffusion coefficients in Figure 5.10c, with standard deviation and standard error of the mean of the diffusion coefficients. SEM and STD are given to get a sense of the distribution, but are not good estimates of uncertainty in diffusion coefficient, because the distributions of diffusion coefficients are not Gaussian. Despite the widely varying shapes of the distributions of the diffusion coefficients, the mean of the distribution is consistently equal to 0.5 $steps^2/timestep$, which was the theoretical diffusion coefficient of our simulations.

In Figure 5.12, we show distributions of diffusion coefficients for different binning

schemes and with y-intercepts forced or not forced to zero. The different binning schemes don't make much difference in the distributions of diffusion coefficients. The choice to force the y-intercept to zero also doesn't make much difference, other than to eliminate negative diffusion coefficients.

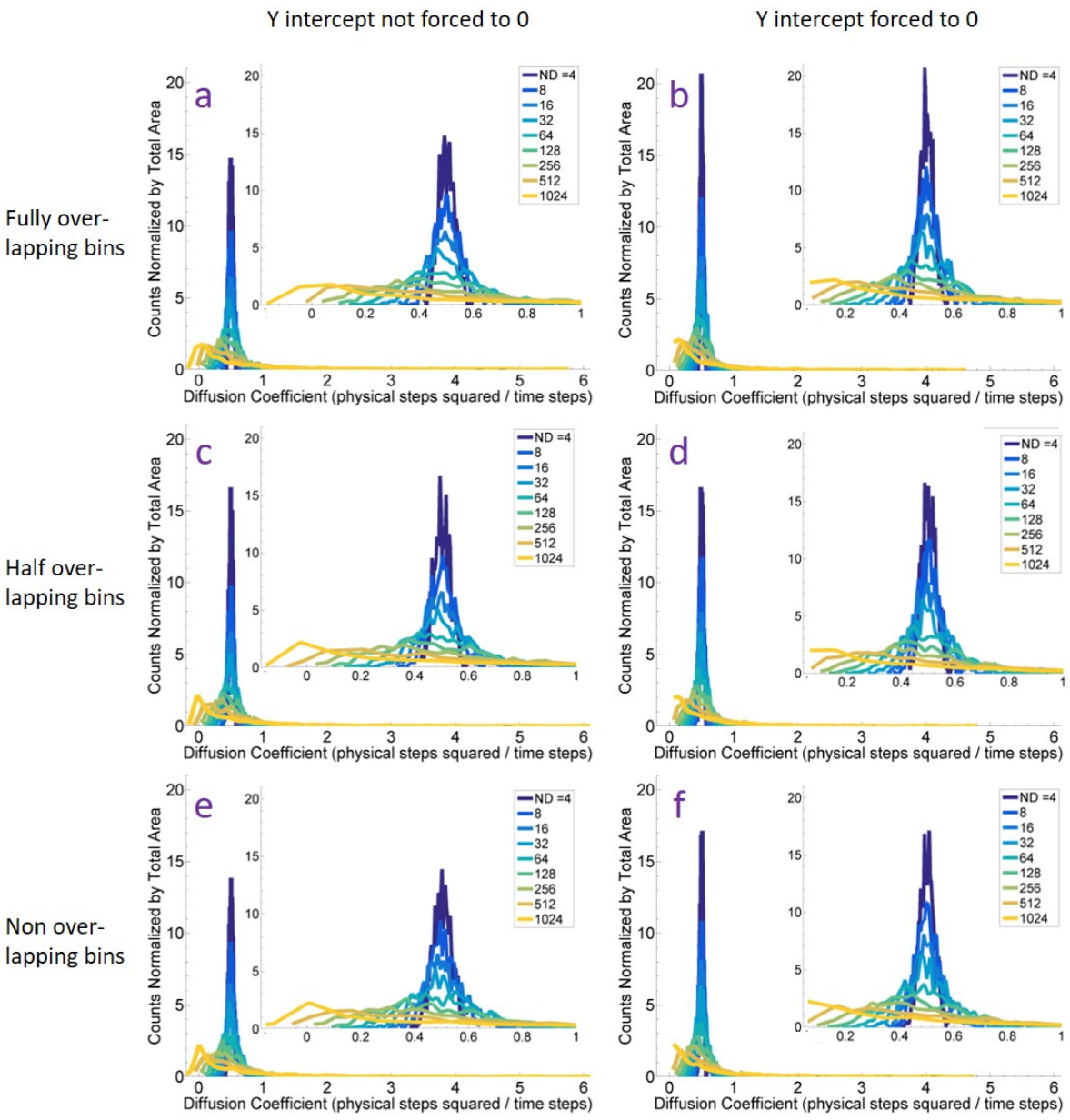

Figure 5.12: Caption appears on following page.

Figure 5.12: Comparison of different binning schemes and line fits. A grid of plots shows the distributions of diffusion coefficients made with line fits whose y-intercepts were either forced to 0 or not, and using either a fully-, half-, or non-overlapping binning scheme. These simulations were made with 1025 time steps and 1024 trajectories. The different calculation methods produced very minor differences.

5.3.6 Distributions of Mean Squared Displacements

Since the distributions of diffusion coefficients we calculated come from fitting the MSD vs. lag curves, an understanding of MSD distribution is crucial to understanding the distributions of diffusion coefficients. Figure 5.13 shows distributions of Mean Squared Displacements calculated using the non-overlapping binning scheme, at various time lags. In 2010, Xavier Michalet published a derivation of MSD distributions[98] (specifically for MSDs calculated using the non-overlapping binning scheme), describing them as Gamma distributed with parameters relating to time lag. We show this distribution below, using the shape-scale factor parameterization of the Gamma distribution, with our variable names, and setting the localization error terms that Michalet describes for modeling experimental positioning uncertainty to zero:

$$PDF_{MSD} = \frac{1}{\Gamma(k)\,\theta^k} x^{k-1} e^{\frac{-x}{\theta}} \tag{5.5}$$

$$k = \lfloor \frac{NT}{\tau} \rfloor, \theta = \frac{\alpha}{\frac{\lfloor \frac{NT}{\tau} \rfloor}{\tau}} \tag{5.6}$$

where Γ is the Gamma function, k is the Gamma distribution shape parameter, theta is the Gamma distribution scale parameter, NT is the number of timesteps in our simulation, τ is the time lag, and α is the average displacement a particle moves between camera frames, which for our simulation is simply equal to 1 time step per 'frame'. $\lfloor * \rfloor$

represents the integer part, or floor function.

This expression for the distribution of the MSD changes based on the time lag, τ. In Figure 5.13, we plot our simulated MSD distributions (also using MSDs calculated with the non-overlapping binning scheme). We compare our distributions to Michalet's predicted distribution, and also show a Gamma fit to our distributions, with parameters k and θ shown in the table in Figures 5.14 and 5.15. Our simulated MSD distributions are well fit with Gamma functions at each time lag, and we see a clear transition in the distributions from Gaussian to Gamma as the time lag increases, as Michalet predicted. The shape and scale factors found by our Gamma fits differ significantly from those predicted by Michalet, but the confidence intervals on the Gamma fit parameters are quite large, which could imply that the shape of the fitted distribution could be quite variable.

Gaussian distributions are a subset of Gamma distributions; a Gamma distribution becomes Gaussian when the shape factor k grows large. The greater the lag, the more time particles have to make larger excursions, and because MSD is a squared quantity, the largest excursions, though rare, are amplified. Because the MSDs are Gamma distributed with shape and scale factors that change with time lag, the fit lines on MSD vs. time lag curves used to calculate diffusion coefficient will incorporate points from many different distribution shapes. Thus, the higher the final lag, ND, in the fit, the less Gaussian the distribution of diffusion coefficients becomes.

5.3.7 Keeping Number of Displacements Constant for Each Lag Time

As the lag increases, the number of displacements that can be computed necessarily decreases (for example, with 1025 time steps, there is only 1 displacement possible for a

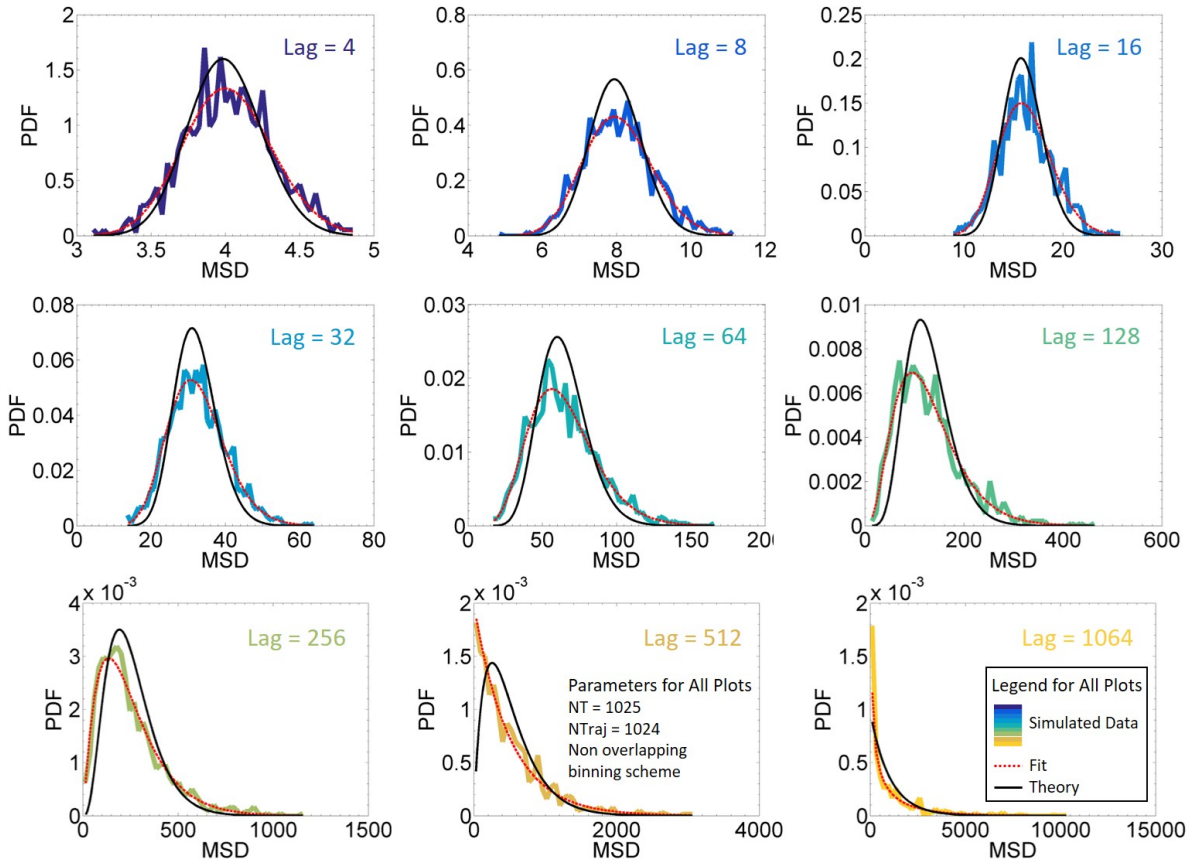

Figure 5.13: Distributions of MSD's calculated using the non-overlapping binning scheme. Colored lines show simulated MSD distribution data. Red dashed lines are a Gamma fit, with parameters k and theta shown in the table in Figures 5.14 and 5.15. Black lines show Michalet's predicted MSD distribution[98] (Equations 5.5 and 5.6). (Non-overlapping binning scheme was used to be able to compare simulated distributions to Michalet's theoretical MSD distribution, which was derived for a non-overlapping binning scheme.)

lag of 1024–the displacement between the first and final time step.) This also means that as the lag increases, the MSD is computed using fewer and fewer squared displacements averaged together. That is, as lag increases, the MSD becomes less of an averaged quantity.

To understand the effects of this phenomenon, we re-computed the mean squared displacements, but held the number of displacements constant–for each time lag, we

k	Lag = 4	Lag = 8	Lag = 16	Lag = 32	Lag = 64	Lag = 128	Lag = 256	Lag = 512	Lag = 1024
Lower Bound of 95% Confidence Interval	165	69	34	16	7.4	3.6	2.0	0.93	0.45
Fit Parameter	180	75	37	18	8.0	3.9	2.2	1.00	0.48
Upper Bound of 95% Confidence Interval	196	82	40	19	8.8	4.2	2.3	1.08	0.52
Theoretical Parameter	256	128	64	32	16	8	4	2	1

Figure 5.14: Gamma distribution shape factor. Blue rows show k with 95% confidence bounds found by fitting the simulated MSD distributions in Figure 5.13 (red dashed lines show the fit). Yellow row shows Michalet's predicted k[98] (Equations 5.5 and 5.6)

theta	Lag = 4	Lag = 8	Lag = 16	Lag = 32	Lag = 64	Lag = 128	Lag = 256	Lag = 512	Lag = 1024
Lower Bound of 95% Confidence Interval	0.021	0.10	0.41	1.7	7.3	30	106	458	1878
Fit Parameter	0.022	0.11	0.45	1.9	8.0	33	116	505	2103
Upper Bound of 95% Confidence Interval	0.024	0.12	0.48	2.0	8.7	36	127	557	2355
Theoretical Parameter	0.016	0.063	0.25	1	4	16	64	256	1024

Figure 5.15: Gamma distribution scale factor. Blue rows show theta with 95% confidence bounds found by fitting the simulated MSD distributions in Figure 5.13 (red dashed lines show the fit). Yellow row shows Michalet's predicted theta[98] (Equation 5.5 and 5.6)

computed displacements as usual, but then randomly selected a certain number of them to be used in the MSD computation. This process is illustrated in Figure 5.16. We use the shorthand term "NumDisps" to describe the number of displacements randomly selected for use in the MSD computation.

We repeated these calculations for several different values of NumDisps. Figure 5.17 shows the MSD vs. time lag curves computed using different values of NumDisps. As NumDisps increases, the "noisiness" of the MSD curve decreases, as the MSD incorporates more displacements averaged together. Although MSD vs. time lag curves should become more linear either as more data is incorporated into them (whether by including more time steps or more displacements, or by averaging multiple MSD curves together), but the curves in Figure 5.17 do not become noticeably more linear at the scales of

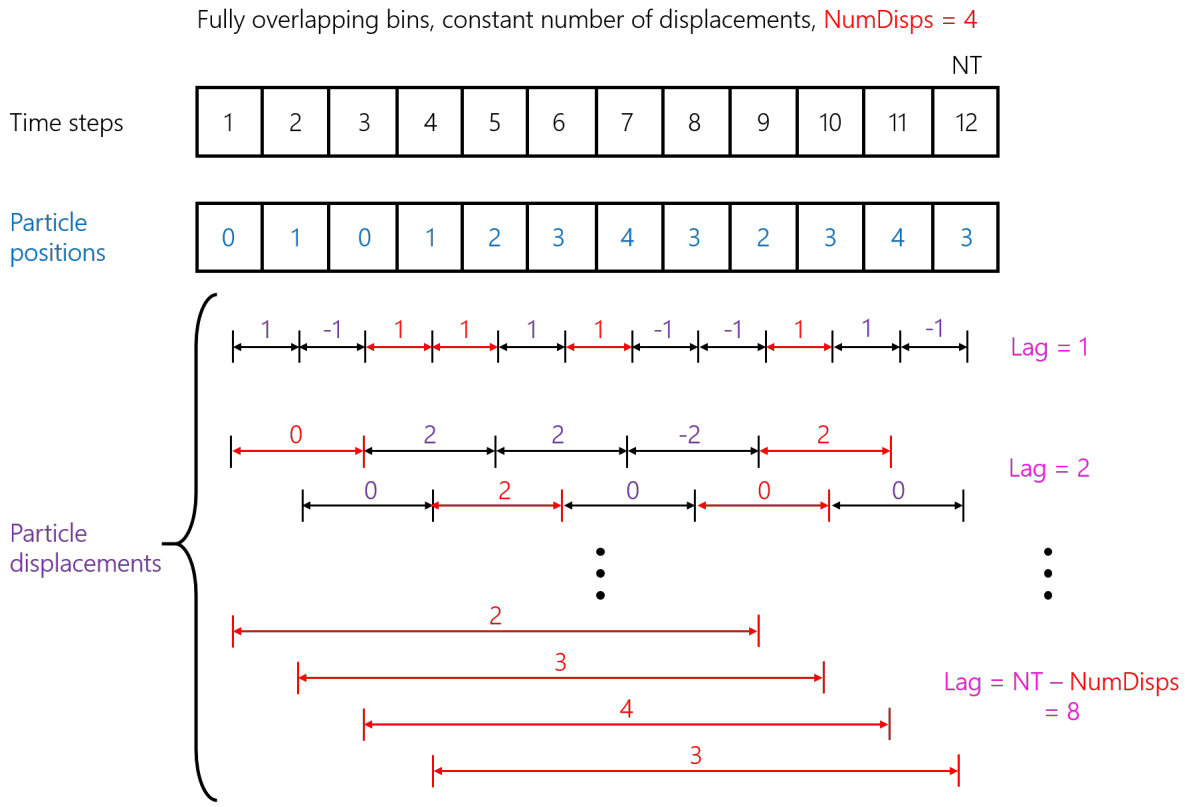

Figure 5.16: Illustration of how we calculated MSDs based on constant numbers of displacements, or as we call this parameter, constant NumDisps. For one calculation of MSD with constant NumDisps, we first select the value of NumDisps–in this illustration, NumDisps = 4. For each lag, we then randomly select NumDisps (4) displacements, square them, sum them, and then divide by NumDisps (4) to get the MSD value at that particular lag. Contrary to traditional MSD calculations, where the number of displacements increases as lag increases, holding NumDisps constant lets us compare MSD vs. lag curves where all lags use the 'same amount of data' in their MSD value. When we have a constant NumDisps, we can calculate MSD for a lag up to NT - NumDisps (where NT is the number of time steps in the particle trajectory).

NumDisps shown–this suggests that quite a lot more data is needed before individual MSD trajectories will converge to a line with a slope that will give a good estimate of the population diffusion coefficient.

The changes in MSD distribution with NumDisps are shown in Figure 5.18. These MSD distributions appear to converge to the Gamma functions predicted by Michalet

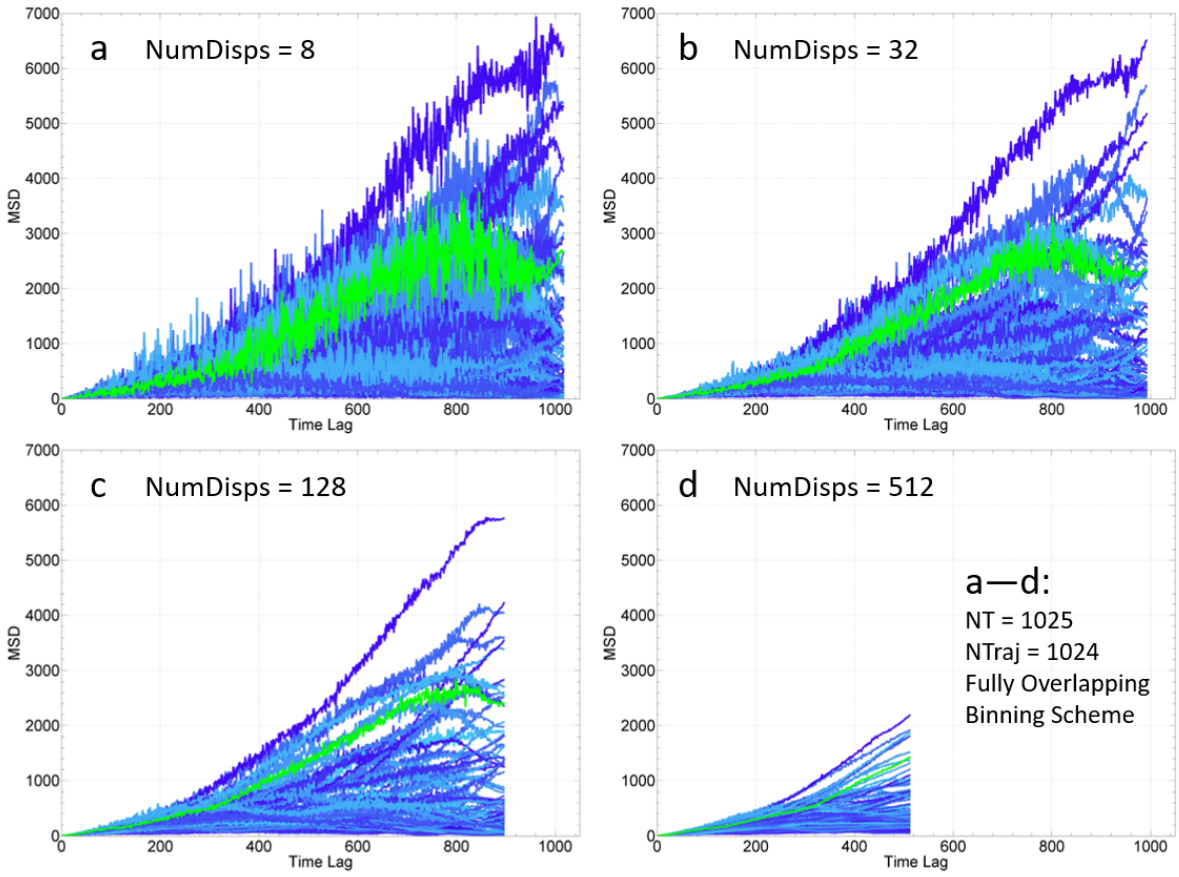

Figure 5.17: Mean squared displacement curves calculated for several constant NumDisps, with NT = 1025, NTraj = 1024, and using the fully overlapping binning scheme. Only the first 100 trajectories out of 1024 were plotted for ease of visualization. Note that as NumDisps increases, the maximum lag at which the MSD can be calculated decreases. As NumDisps increases, the MSD vs. time lag curves become less "noisy", as they incorporate more data points into the average.

as NumDisps increases, but seem to have entirely different shapes for small NumDisps. Looking at the corresponding lags in Figure 5.17, the MSD curves do appear to "tighten" towards 0 as NumDisps increases. This effect persists when we repeat the calculations using the non-overlapping binning scheme, implying that it is not caused by a change in correlation between displacements as NumBins changes.

Figure 5.20 shows distributions in diffusion coefficients found using constant numbers

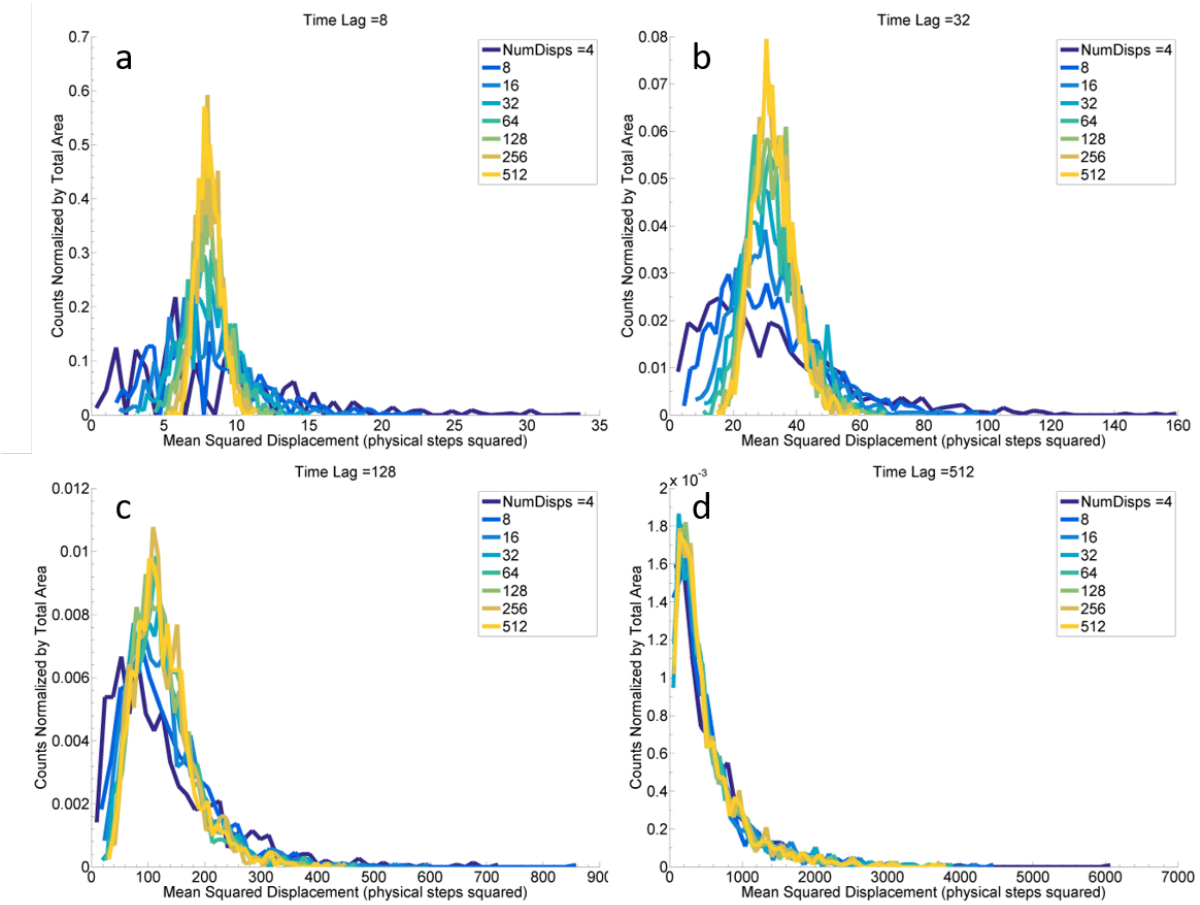

Figure 5.18: Distributions of mean squared displacements as functions of time lag and NumDisps, NT = 1025, NTraj = 1024, using the fully overlapping binning scheme.

of displacements in the MSD calculations. These distributions show very similar shape trends to those in Figures 5.10 and 5.12, in that the distributions appear nearly Gaussian for small ND and non-Gaussian for large ND. This supports the idea that the distributions of diffusion coefficients naturally become non-Gaussian as the lag increases, and that the non-Gaussian shapes are not caused by a insufficient amounts of data.

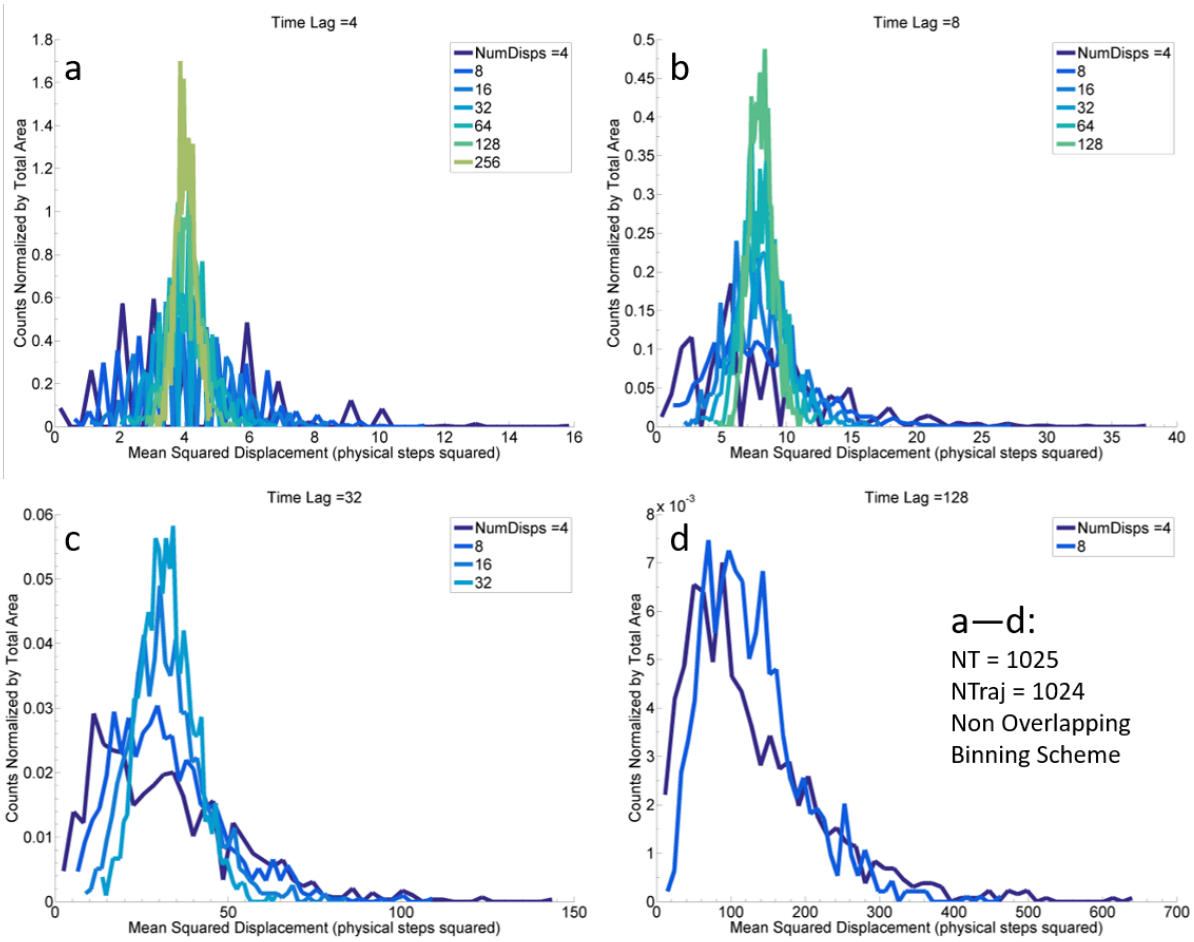

Figure 5.19: Distributions of mean squared displacements as functions of time lag and NumDisps, NT = 1025, NTraj = 1024, using the non overlapping binning scheme.

5.3.8 Distinguishing Static Particle populations

One particular challenge in studying single molecule diffusion on microtubules is determining whether or not some fraction of the particles are actually static, and whether the proteins switch between strongly- and weakly-bound states, as it is believed with tau[39]. Measurement noise, including the slight motion of microtubules fixed to a surface, makes it extremely difficult to determine by eye whether a particle is static or diffusing.

In his study of EB1 diffusing on microtubules, Ben Lopez attempted to distinguish a

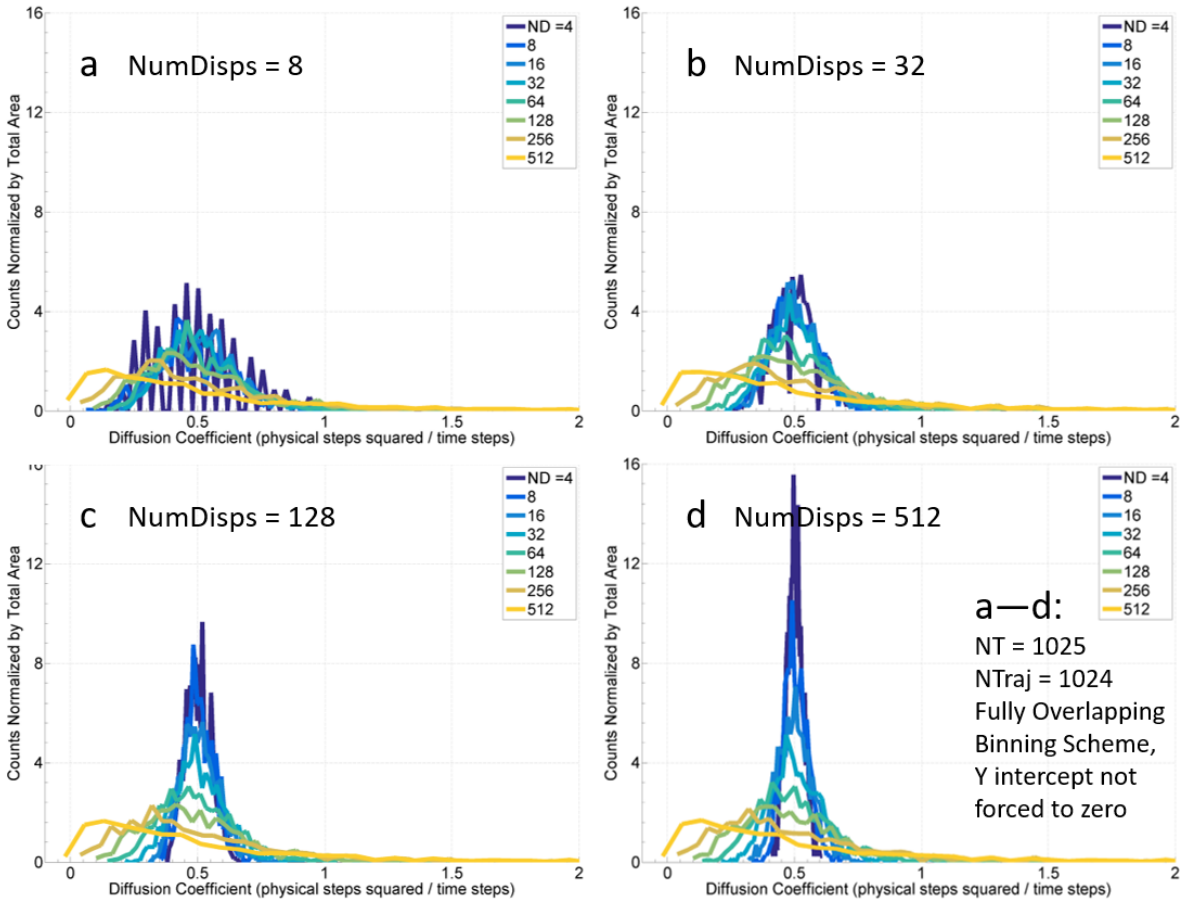

Figure 5.20: Distributions of diffusion coefficients found by fitting lines to MSD vs. lag curves that were calculated using a constant number of displacements, NumDisps. ND is the maximum lag that was used to create the fit. NT = 1025, NTraj = 1024, fully overlapping binning scheme, y-intercept was not forced to zero.

static EB1 population by measuring the perceived diffusion coefficient of EB1 molecules that were purposefully immobilized as a control[40]. Lopez measured a value of 0.001 μm^2/s as the immobilized EB1 diffusion coefficient, and hoped to use this as a cutoff value to differentiate diffusing EB1 molecules from static EB1 molecules. However, the measured distribution of diffusion coefficients showed a continuous rise in the counts as D decreased (Figure 5.2b), in an exponential-looking distribution, and no clear cutoff value between static and diffusing populations could be determined.

After seeing the non-Gaussian nature of many of our simulated diffusion coefficient distributions, we wanted to model the experimental conditions of Lopez's EB1 data to see what fraction of diffusion coefficients would have a value less than or equal to 0.001 μm^2/s, in a pure diffusive process without measurement noise.

Lopez's experiments included a camera frame rate of 20 frames/s, and the measured particle trajectories typically lasted for less than 1 second before the particle bleached or detached from the microtubule. Lopez was able to gather between 450 and 1700 particle trajectories for each of the different microtuble conditions he looked at, and the mean diffusion coefficients $D_{Experimental}$ ranged from 0.1 to 0.4 for different microtubule conditions.

Since the underlying step size of the EB1 diffusive process is unknown, we decided to us a new simulation method to model Lopez's experimental conditions. Instead of producing discrete random particle steps, we instead replaced the particle steps with continuous random particle displacements pulled from a Gaussian distribution. For each particle trajectory, we pulled NT values from a Gaussian distribution with a mean of 0 and a variance equal to $2 * D_{Experimental} * \Delta t$, using a $D_{Experimental}$ of 0.1 $\mu^2 m/s$–one displacement value for each time step. For NT, we used 1 second * 20 frames/s = 20 frames, or time steps. We set the first displacement value to 0 to create a common starting point for the trajectories, and then cumulatively summed these displacement values to obtain the particle's positions over time. Each time step represented 1 camera frame, each with a time change of 1 / 20 frames/s = 0.05 s. We simulated 1000 of these trajectories.

We used the fully overlapping binning scheme to calculate the MSD of the trajectories, and then calculated diffusion coefficients by fitting lines to the MSD vs lag curves. We did not force the y-intercepts of the fits to zero.

Figure 5.21a and b show the simulated particle positions over time and their distribu-

tions, as validations that these simulations correctly model diffusion. The table in Figure 5.22 show diffusion coefficients calculated from particle position distributions according to Equation 5.1. All of these calculated diffusion coefficients match the experimental and simulated $D_{Experimental}$ value of 0.1 $\mu^2 m/s$ within their uncertainty.

Figure 5.21d shows the distributions of diffusion coefficients calculated from these simulations, by fitting lines to the MSD vs. lag curves and using the lags from 0 to ND. It is interesting to note that none of these distributions looks particularly Gaussian, which reflects the distribution shape that Lopez found in Figure 5.2b. Lopez typically cut off his MSD trajectories at 1/3 of their largest lag, which would correspond to an ND between 0.2 and 0.4 for our plot.

Due to our modified simulation procedure of sampling from a Gaussian distribution, the "step size" of this process is effectively infinitely small, but is technically related to the number of significant digits used in our computations. By sampling displacements from a "continuous" Gaussian distribution, we effectively made our smallest possible displacement equal to the smallest number that we can represent with a double precision floating point number–this number is very small compared to the displacements we actually worked with in our calculations. This condition of measured displacements being much larger than inherent diffusive step sizes is true for most experimental measurements of single molecule diffusion on microtubules, which is perhaps why experimenters often see diffusion coefficients distributions that resemble exponential distributions.

The table in Figure 5.23 shows the mean diffusion coefficient calculated directly from each distribution of diffusion coefficients. The mean diffusion coefficients are all very close to the experimental and simulated diffusion coefficient of $0.1\mu m^2/s$. The standard deviation of the distributions and standard errors of the mean are also shown to get a sense of what an experimenter would see if calculating these parameters, even though standard deviation and standard error of the mean do not make sense to use as uncertainty

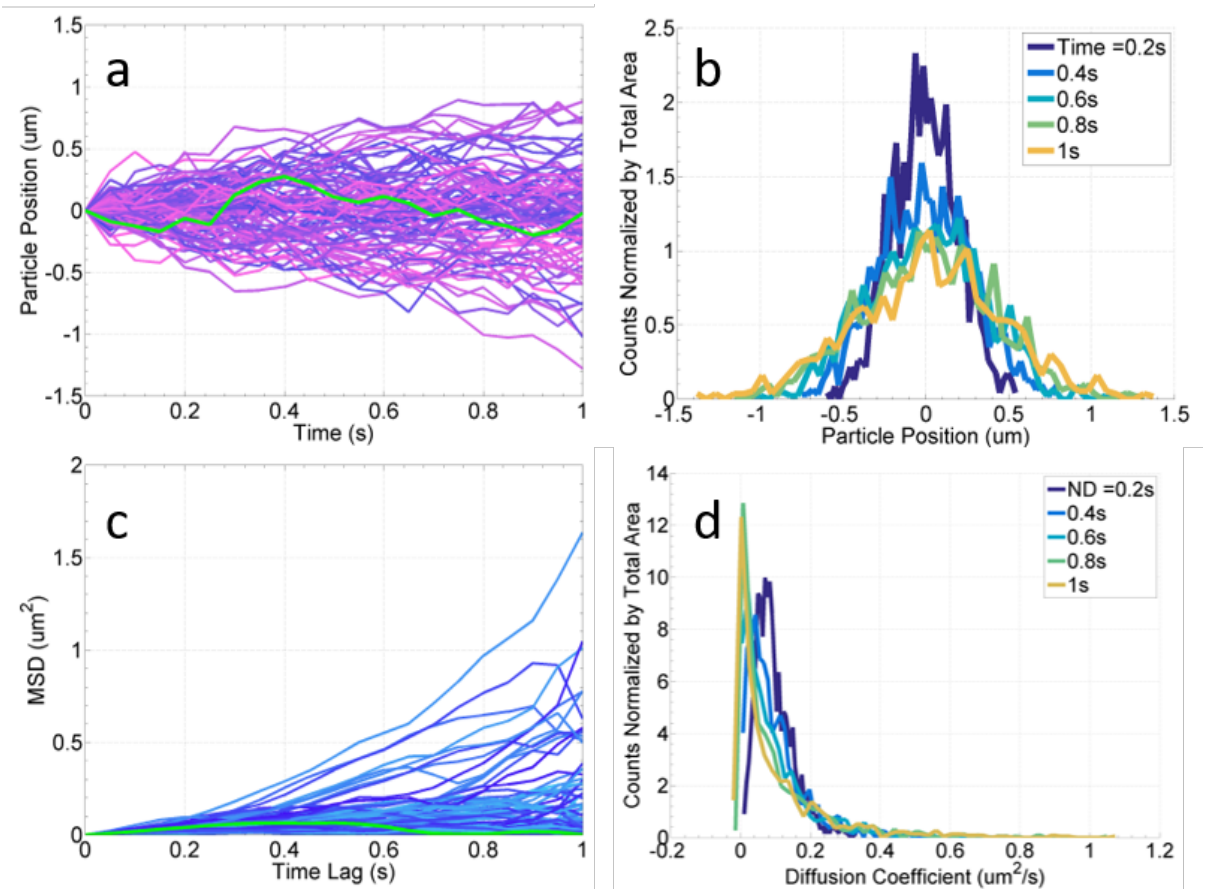

Figure 5.21: Simulations modeling Ben Lopez's EB1 experimental conditions[40]. a. Simulated particle positions over time. Because underlying EB1 step size is unknown, we chose to simulate these particle positions by drawing one particle displacement for each time step from a Gaussian distribution with a mean of 0 and a variance given by the experimental diffusion coefficient of 0.001 $\mu^2 m/s$. These displacements were summed up cumulatively over the time steps to produce trajectories of particle positions vs. time. b. Histograms of particle positions at particular times were plotted to validate that the simulated process accurately represents diffusion. Values of diffusion coefficients found from these histograms are given in the table in Figure 5.22. c. Simulated particle MSD vs. lag, calculated using a fully overlapping binning scheme. d. Distributions of diffusion coefficients found by fitting lines to the MSD vs. lag curves, and using lags from 0 to ND.

estimates of the mean diffusion coefficient for these non-Gaussian distributions.

The table in Figure 5.23 also shows the percentage of diffusion coefficients in each distribution that were less than or equal to 0.001 $\mu m^2/s$, the diffusion coefficient that

Time (s)	0.2	0.4	0.6	0.8	1.0
D calculated from Gaussian fit parameter (µm^2/s)	0.10	0.11	0.11	0.10	0.10
Uncertainty in D from propagated fit parameter uncertainty (µm^2/s)	0.02	0.01	0.01	0.02	0.01
D calculated from population variance (µm^2/s)	0.097	0.098	0.098	0.101	0.101
Uncertainty in D from propagated standard error of the variance (µm^2/s)	0.004	0.004	0.004	0.005	0.005

Figure 5.22: Diffusion coefficients with their uncertainties, calculated from the histograms of particle positions at particular times. The blue rows show diffusion coefficients and their uncertainties calculated from Gaussian fits to the particle position distributions. The green rows show diffusion coefficients found by directly calculating the variance of the particle positions, with uncertainties propagated from standard error of the variance.

Lopez measured for his deliberately immobilized EB1 molecules. These calculations show that as ND increases, a significant portion of the distribution of diffusion coefficients could appear as though they were static, simply due to the fact that the distributions include a large number of low diffusion coefficients.

ND (s)	0.2	0.4	0.6	0.8	1.0
Mean D (µm^2/s)	0.0967	0.0973	0.0985	0.0989	0.101
SEM of D (µm^2/s)	0.00005	0.00008	0.0001	0.0001	0.0002
Std Dev of D (µm^2/s)	0.05	0.08	0.11	0.13	0.15
% of D's < 0.001 um^2/s	0%	0.1%	1%	5.3%	16%

Figure 5.23: Diffusion coefficients from the EB1 modeling simulations, calculated by taking the mean value of the distribution of diffusion coefficients. Standard error of the mean of D as well as the standard deviation of D are shown for comparison, although neither of these is a good measure of the uncertainty in the mean D because the distributions of D are not Gaussian. In the final row, we show the percent of diffusion coefficients from the distribution of diffusion coefficient which had a value less than or equal to $0.001\mu^2 m/s$, the diffusion coefficient value that Lopez measured for deliberately immobiliezd EB1 particles[40].

These findings support Lopez's hesitancy to define a cutoff diffusion coefficient value

to separate diffusing and static populations of EB1. Experimenters should also be careful when labeling a particle as diffusing or static, as measurement noise and the fact that the diffusion coefficients distributions do not show clear Gaussian peaks mean that particles that are in fact diffusing could appear static. However, if an experimenter obtained a diffusion coefficient distribution that was markedly different from any of the distribution shapes shown here, then that could suggest anomalous diffusion.

5.4 Conclusions

The distribution of diffusion coefficients, even for a purely diffusive process with no measurement noise, is not necessarily Gaussian, and may appear to have a shape reminiscent of a Gaussian, Gamma, chi-squared, lognormal, or exponential distribution. These shapes do not indicate anomalous diffusion, or measurement problems. Because these distributions often include a significant fraction of small diffusion coefficients, experimenters must use extreme caution in setting thresholds to determine whether a single particle trajectory is diffusive or stationary based on its computed diffusion coefficient. Experimenters should also take care when using diffusion coefficient to define "outlier" particles, as some of the natural diffusion coefficient distribution shapes include long tails with small numbers of large diffusion coefficients. Bayesian approaches are a useful tool for determining whether a data set fits a particular diffusive model because they do not require any prior assumptions of the distribution shape, and have been described by Monnier in 2012[99], who also provides a MATLAB package for Bayesian diffusion analysis at http://msd-bayes.org/.

For best estimates of the particle population diffusion coefficient, we recommend avoiding calculating diffusion coefficients for single particle trajectories, and instead using averaging methods, such as averaging all MSD vs time lag curves together before fitting a

line, or obtaining a variance from the histograms of all particle displacements. Using the latter method, confidence intervals on the diffusion coefficient can be found by calculating the uncertainty on the variance. Michalet[98] has described obtaining uncertainty for diffusion coefficient from the uncertainty in the line fit parameters of MSD vs. lag, and provided a heuristic formula for determining the number of data points that should be used in an MSD line fit.

Chapter 6

Conclusions and Future Directions

6.1 Summary

Our efforts have laid the groundwork for many transport experiments. We have constructed a sophisticated optical trapping setup capable of applying and measuring forces with 2 pN accuracy, controlling sample motion with nm to micron precision over a wide range of distances and speeds, and observing samples with both brightfield and TIRF microscopy. We have developed extensive software for controlling and calibrating all aspects of the setup. We designed a new biomimetic droplet system that reproduces the surface properties of biological cargoes, while exhibiting a modular and practical design that can be adjusted to new purposes. We developed a new optical trapping force calibration technique that greatly expands the usable radius of the trap, while reducing the technological requirements of the calibration. Finally, we explored and elucidated diffusion measurements to help experimenters improve their reporting accuracy and interpretation of diffusion data.

6.2 Use of Biomimetic Cargoes in Collective Motor Transport

Our biomiemtic cargoe system could be used in many ways to test fundamental questions about intracellular transport. With the addition of our new Fluctuations trap force calibration method, the useful force range of an optical trap can be extended to be able to apply and measure the high forces developed by groups of motor proteins.

By controlling the fraction of biotinylated lipids in the surface surface of our biomimetic droplets, the fraction of kinesins that attach to the cargo can be tuned. In this way plots of stall force vs. motor density, and velocity vs. force curves for varying numbers of motors could be produced.These experiments would test our hypothesis that fluid and rigid cargos have fundamentally different surface properties which affect the dynamics of collective kinesin transport.

The surface properties of the cargoes could also be adjusted to be somewhere between completely rigid and completely fluid. Cargoes of intermediate rigidity may be a better model for true biological cargoes, because biological membranes contain a diverse collection of lipids and proteins, resulting in more complicated surface properties. These cargoes could be used to investigate whether intermediate rigidity has a significant impact on kinesin behavior and transport. Cholesterol is known to increase cell membrane rigidity by inducing the formation of lipid rafts (lipids in a liquid-ordered phase[75].) The lipid mobility of cargoes with incorporated cholesterol or other biological membrane components can be measured using established techniques such as fluorescence recovery after photobleaching (FRAP.) We expect that it would take some effort to develop and characterize these intermediate cargoes

Our biomimetic cargo system could be used to study collective transport using other molecular motors. MAPs could be added to the microtubules to investigate their effects

on collective transport of fluid cargos. The behavior of multiple motors at microtubule intersections when pulling fluid cargoes could also be investigated, similar to the intersection studies done by Vershinin[29] and Ross[38]. The cargoes could perhaps even be injected into living cells as controlled test cargos for observing cellular transport *in vivo*. Our cargoes could be used to test fundamental questions such as how cells determine when a cargo has reached its destination, what mechanisms exist to regulate transport, the ways in which transport can go wrong, and possibly ways it can be fixed.

Appendix A

LabVIEW VIs

Below is a list of the main top-level vis that I used and created in order to run the optical trapping setup. Most of these top level vis call numerous subvis that I wrote, most of which have detailed documentation within them.

JoystickAndShutters_JCW4

Author: JCW Allows the user to control laser shutters and camera mirror, and the to run the large PILine M-686.D64 stage with a joystick. Use the shift key on the keyboard to toggle the trap shutter.

CalibrateDiode5thOrderAOD2014 - PSDcalibration_3

Authors: NRG, BL, JCW This is the vi you would use to calibrate the nm/V values of the PSD. This vi uses the AOD to sweep the trapping laser spot, which holds a trapped bead, through the stationary detection laser spot; the diffracted light on the PSD produces a voltage signal that is proportional to the bead's displacement from the center of the detection laser spot. This is done in two steps: first, FindCenterAndRadius AOD MX is run, which sweeps the bead first from left to right, then from top to bottom,

through the detection spot–this produces two (one for x direction, one for y direction) PSD voltage (V) vs. AOD frequency (MHz) plots; the plots are fitted with a derivative-of-a-Gaussian curve to find the center of the detection laser spot. The vi then adjusts the AOD frequencies to move the trap with bead into that fitted center point (the predicted center of the detection laser spot.) The main vi then raster scans the bead through an array of x and y AOD positions–that is, it raster scans the bead through a 2D slice of the detection laser spot in the laser's radial direction. (The z height of the stage and therefore the distance from the bead to the surface of the chamber is constant throughout this whole procedure.) The vi then fits the 2D rastered data to produce two values: the nm/V conversion factors in the x and y directions. These conversion factors are conceptually equivalent to the slopes of the derivative-of-a-Gaussian fit curves in the x and y directions. On 7/26/07, this was changed so that each axis uses it's own calibration value to compute sensitivity and NOT the average value. Also, global values for the nm to EODv were added.NRG 9/2012 BL: Updated for AODs and current setup 1/6/2015 JCW: I switched the global inputs "X MHz/nm" with "Y MHz/nm" because these calibration parameters follow the x as left-right convention, and I switched the outputs "X nm to PSDx V" with "Y nm to PSDy V" so that the outputs will follow the convention that x is the left-right direction on the camera.

Brightfield CameraControl

Author: Ben Lopez Runs the small PGR camera that we use for brightfield (USB connection)

Cameras_JCW_15

Author: JCW This vi runs both the small PGR CCD camera (with USB connection to the computer) and the Andor EMCCD camera (connected through a PCI card, plugs

into the back of the computer) at the same time. It controls a temperature loop to appropriately cool the EMCCD camera, and allows acquisition and saving of images from each camera. Andor Acquisition tab: User can change the camera settings by typing numbers into the boxes, then clicking "Set Acquistion Paramters"; parameters will only change after acquisition is turned off and back on again. Use "Number of frames to save" combined with the acquisition type "Acquire and save finite frames" to save a finite number of images at a time. "Approximate Andor Frame Time (s)" will add a delay within the Andor acquisition loop to approximate a desired time for each frame, but do not rely on this if you want to enforce a precise frame rate. If you need a precise frame rate, use the Andor proprietary software to run the Andor camera. CCD Acquisition tab: "Approximate CCD Frame Time (s)" will add a delay within the Andor acquisition loop to approximate a desired time for each frame, but do not rely on this if you want to enforce a precise frame rate. The Transfer Andor ROI to CCD Camera will take the Andor ROI (click on the Andor image to create an ROI) and transform it to map it onto the CCD camera image. This is useful for, for example, trying to keep track of the location of microtubules between TIRF and brightfield. To use this feature, the transformation between cameras must be calibrated with the X Offset, Y Offset, X Scale, and Y Scale values in the Andor tab. I recommend using a stuck bead slide, and drawing a line ROI between two diagonally separated beads in TIRF (Andor camera) then switch to brightfield (CCD camera) and first adjust the scale values so that the line length is orrect, then adjust the offset values to translate the line to the correct place so that the line stretches between the same two beads you saw in TIRF. This vi does not control shutters or the camera mirror–be sure to use another vi to physically switch the light path between cameras. The Andor Acquire button will collect Andor images using the settings specified in the Andor tab. The Andor Snap button will take a set of finite images using the specified settings. This allows you to turn on Andor

Acquire with the continuous option without saving anything to look at something, then hit the Andor Snap button to quickly save images. More notes on implementation and limitations are written in comments in the vi. Read before operating: The user can chage Number of pixels to bin BEFORE startup only. The user can change Exposure Time, Gain, and Set Temperature by changing the values and then pressing the Set Acquisition Parameters button. The user can change the values of Max frames to save and Number of frames to save for each acquisition any time before acquiring. A set temperature of -90 is recommended.

ConvertTDMS_JCW

Author: JCW The user can input the file path of a TDMS file that includes the NI proprietary RAW data encoding, and the vi creates a new file without the RAW data so that the file can be read by another program like MATLAB.

DVE Control

Author: IntraAction Corp. This is a vi that was provided by IntraAction to interface the AOD through labview. Use the Freq 1 values to adjust the x and y position of the trapping laser, and the Amplitude values (5.00 mW max) to adjust the power of trapping laser that goes through. Note that 5.00 mW on the AOD does not mean that 5.00 mW of trapping laser power goes through. I calibrated the AOD amplitude to laser power output separately.

EscapeExperiments17_JCW

Read before operating: WARNING: Running this VI will cause the PILiine stage to reference itself using its reference switches. Make sure there is nothing that could get in the way of the PILine stage.

Note that this vi does not have a way to directly detect the state of the shutters and mirrors, so the LEDs might not display the correct state on startup.

You can stop the vi with the F12 key on the keyboard.

You can toggle the Trap shutter using the Ctrl key on the keyboard.

You can stop the motion of the M686 Stage using the Shift key on the keyboard.

You can toggle data recording with the Enter key on the keyboard.

The arrow keys on the keyboard will move the M686 stage by the step size specified in the M686 Stage tab, at the specified velocity.

Unfortunately, I am not able to scale the voltage data to convert it to units of nm before streaming it to the disk, so the user must take note of the nm/V calibration factors and scale the data later.

Overview: Author: Jamie Wilcox Created: 2016-7-6 Last Modified: 2016-7-13 This vi controls: Brightfield Lamp shutter, Camera Mirror, Detection Laser shutter, Trapping Laser shutter, Green Laser shutter, Blue Laser shutter, M686 PI Stage, DAQ sampling 13: Changed vi so that new stage movements cannot be queued until the stage has stopped moving. In other words, if the stage is moving and you press an arrow key, then the event that would normally be triggered is ignored. 14: Added realtime data viewing. I chose to separate data viewing and data saving. It may be possible to both stream and view at the same time, but I do not know whether simultaneous viewing will affect the integrity of the stream (RAM overload might cause some of the measured values to not record) I had the option of adding the option to view the data while recording, but I decided that what I will normally want to do is to either view the data for a brief period of time or record the data, so I think splitting these functionalities is the best route at this time. Note that you can convert the first two DAQ channels to nm when viewing, but you CANNOT convert when saving. This conversion must be done later in post processing of the data. I do not allow the user to turn recording on while viewing, and vice versa.

This is because doing so would create a channel conflict. It may be possible to set it up so you can record while viewing, but I do not need to do this and I believe it would be tricky. 16: Added PI517 Stage control 17: Replaced InitConfigM686Stage_2_JCW with InitConfigM686Stage_2_JCW_2 because I seem to have a slightly different PI library than I did before, and I just needed to adjust the inputs to one function in that vi.

FindSurfaceHeightAndMove_JW

This is my modified version of setting a bead's height to a certain distance above the chamber surface (coverslip.) It moves the P-517.3CD stage in its z axis before running the surface-finding algorithm to prevent the stage drifting further and further towards its max value when this vi is used multiple times. That is, it resets the starting z value to 0 each time to avoid getting the stage into a position where it can't complete the commanded moves.

FindSurfaceHeightandMovePSD MX

Comments: Modified by MTV 05/2007 to update to DAQ-MX. Use this program to specify the height of a trapped bead above the coverglass surface. This program moves the stage in in z, and records the PSD sum voltage during the move, and plots the signal.

PowerSpectrumJCW2_2

Authors: BL, JCW This vi acquires PSD voltage data, converts the voltages to nm using the V/nm conversion factors found with CalibrateDiode5thOrderAOD2014 - PSDcalibration_3, saves the data, and displays x and y power spectra of the data. The data saved is raw PSD data, and the power spectra displayed in the GUI are NOT saved. There could potentially be a slight delay between the acquisition of different "averages"

(different chunks of data) so be sure to use the same number of samples for each average or chunk when you average the data and calculate the power spectra later.

StreamDAQ_JCW_1

This vi saves data from the PSD at a specified sample rate continuously, streaming the data to disk. It uses labview's proprietary TDMS RAW data format but can be converted to plain TDMS using ConvertTDMS_JCW. I used this for collecting overnight PSD measurements when testing the integrity of the trapping laser.

StokesDrag7JW

This vi performs Stokes Drag experiments–it sweeps the stage and its fluid past a trapped bead and records the bead's displacement from the stationary trap center (which should be calibrated to exactly overlap the detection laser center). The measurement uses the PSD voltages and V/nm calibration factors to determine the bead's displacement. This version only moves the stage at one velocity, but it does multiple trials at the same velocity. In StokesDrag4 I added a loop that does both the positive and negative of one velocity, one after another. This causes the bead to not have to move to its starting position after each run, and saves time. In StokesDrag5 I am using the input Time to collect data after moving stage (s) to determine how far to move the stage. The movement will always start at the same initial position, but the final position will depend on how much time's worth of data the user wants to collect and the stage velocity. The user must not input an amount of time to collect data that causes the final distance to be greater than the stage range. The user must also not put in a negative value for the start position. I also changed the 'microns to move z-axis' parameter to 'microns to move z-axis per microns to move x-axis.' The new input parameter is the number of microns that the stage should move in the z-direction for every micron moved in the x

direction. Changing this parameter means that the parameter stays the same regardless of how many microns the stage will move during the run. (Previously I had to change the microns to move z-axis parameter every time I changed the final distance moved.) In StokesDrag6 I replaced MV STAGE RECORD PSD 3 with –4. This change makes movement in the y direction work. StokesDrag7–I now calculate the amount of time that the stage can move at a given velocity. The stage can only move 100 microns. Before, I had to make sure that the amount of time I asked the vi to move for was short enough so that the stage wouldn't run out of space at that velocity. I don't have to worry about that anymore. The input, 'Max time to collect data after moving stage (s)' sets a maximum amount of time to collect data after the stage moves. If this user's max amount of time is shorter than the calculated amout of time that the stage is able to move at the given velocity, then the vi will use the user's value; if the user puts in an amount of time that is longer than the stage is able to move for, then the vi defaults to the amount of time the stage can move according to its range of 100 microns.

SelectShutters1_JCW

The function of this vi is to allow the user to individually move the shutters and the camera mirror, which are all controlled through the DAQ's binary input/output array.

PIStageSimpleMoveJW

A very simple vi to send velocity and absolute position commands to the P-517.3CD stage.

Raw PSD MX - saving data_JCW

Authors: BL, JCW This vi is used for watching the PSD signals through the DAQ in realtime. It shows the data in plots, dials, and as decimal values. Contrary to its name,

it does not actually have the capability to save any data.

TestStageVelocityAccuracy3

Moves the stage and tracks a stuck bead; saves bead position data. This vi was used to test the accuracy of the stage by commanding the stage to move at a constant velocity and recording the position of a stuck bead.

TestStageVelocityAccuracyUsingStageControllerVis2_M686

This vi was used to test stage accuracy by commanding the stage to move at a constant velocity and recording the stage position measured by the stage's own sensor.

Appendix B

Log-Log Plots of Mean Squared Displacements

One technique that is sometimes used to check whether a particle trajectory is diffusive is to plot the MSD vs. lag data on a log-log scale–if the MSD and lag data have a linear relationship, then they will appear as lines with a slope of 1 on the log-log plot. If the MSD vs. lag have a different power relationship, then the log-log plot allows the experimenter to easily observe the power by eye from the slope of the curve on the log-log plot. It is important to note, however, that small amounts of purely diffusive MSD vs. lag data will not appear linear, as shown in the plots below.

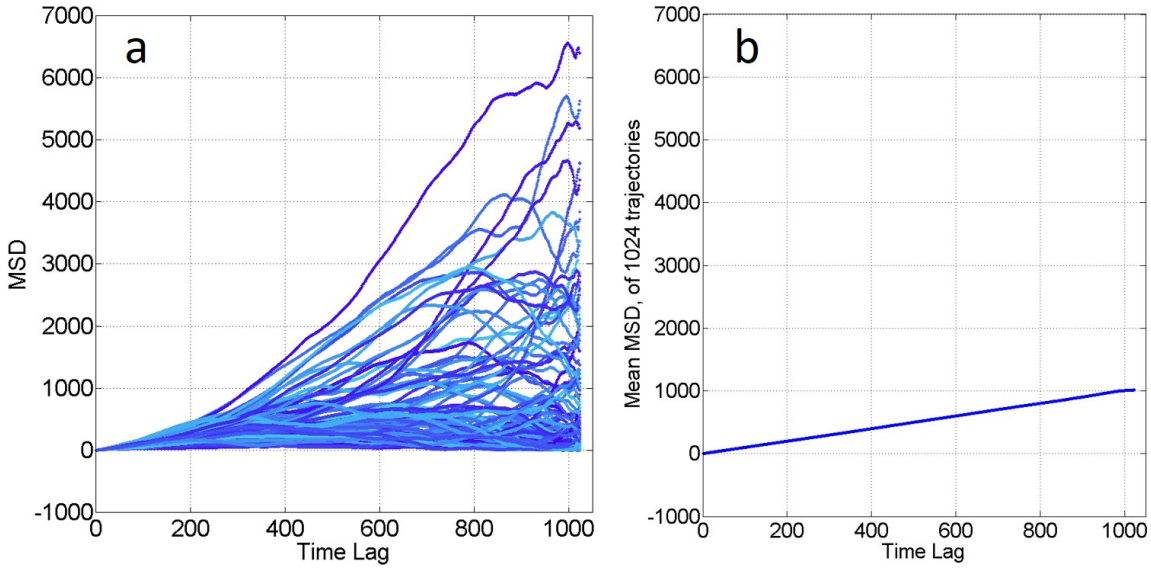

Figure B.1: MSD vs. lag data for 1024 simulated trajectories with 1025 time steps each, using the fully overlapping binning scheme to calculate MSD. a. MSD trajectories vs. lag. Only 100 trajectories out of the 1024 simulated trajectories are plotted for visualization. b. mean of all 1024 MSD vs. lag trajectories. The plot of mean MSD is very linear except at very large lags.

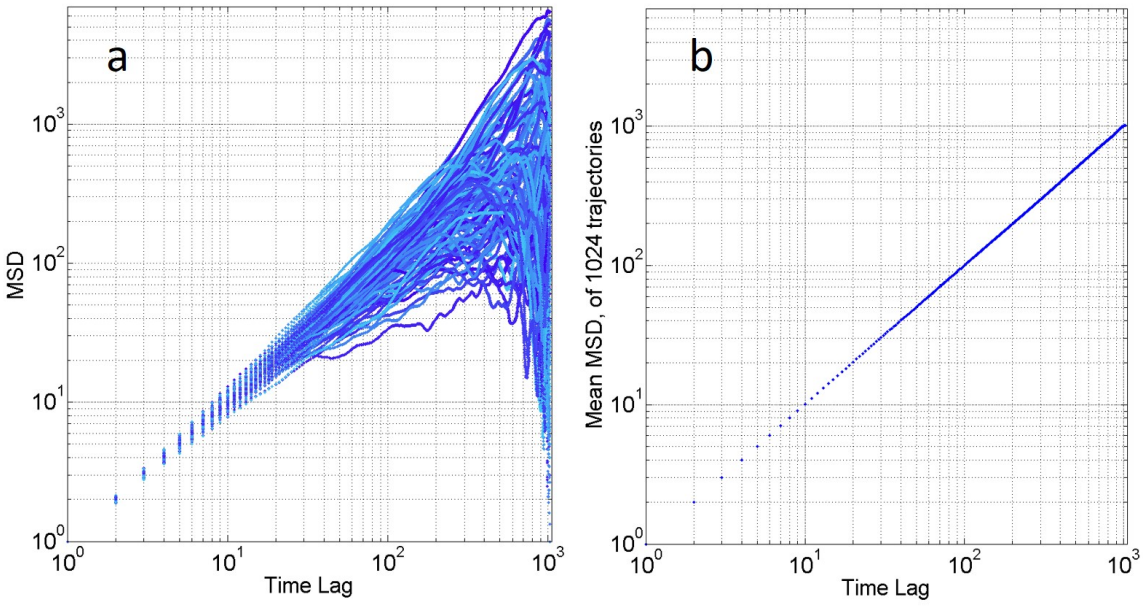

Figure B.2: The same data as shown in Figure B.1, plotted on a log-log scale. (1024 simulated trajectories with 1025 time steps each, using the fully overlapping binning scheme to calculate MSD.) a. 100 of the 1024 MSD trajectories are plotted for visualization. b. mean of all 1024 MSD trajectories. Again, mean MSD is very linear except at very large lags. It would be a mistake to look at one of the individual trajectories in a. and label it "non-diffusive at high lags"—although the trajectories become nonlinear at high lags, this is a normal result of the stochastic process, and not an indicator of anomalous diffusion.

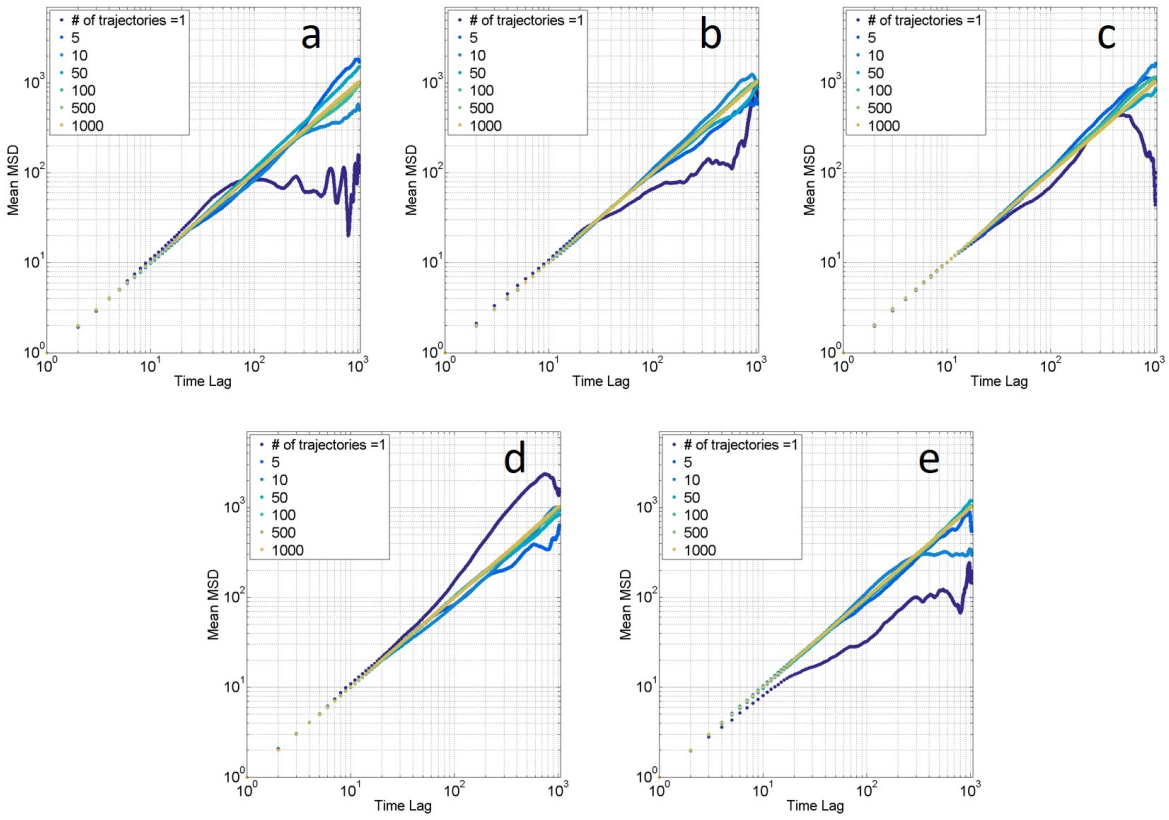

Figure B.3: Mean MSD on a log-log scale, averaged over varying numbers of trajectories. 1024 particle trajectories were simulated with 1025 time steps each, and the fully overlapping binning scheme was used to calculate MSD. 5, 10, 50, 100, 500, and 1000 MSD trajectories were uniformly sampled from the population of 1024 trajectories, and averaged together to produce the mean MSD vs. lag curves shown. Figures a–e differ only in the particular trajectories that were sampled and averaged together, and were produced by giving different seeds to the random number generator before trajectories were sampled. The plots a–e show the wide variability in mean MSD shapes that can appear when averaging few MSD trajectories together. The mean MSD curves appear to become reliably linear when 100 trajectories (each with 1025 time steps) are averaged together; in other words, the mean MSD curves require on the order of 10 000 particle position data points before their averaged MSD vs. lag curve appears linear.

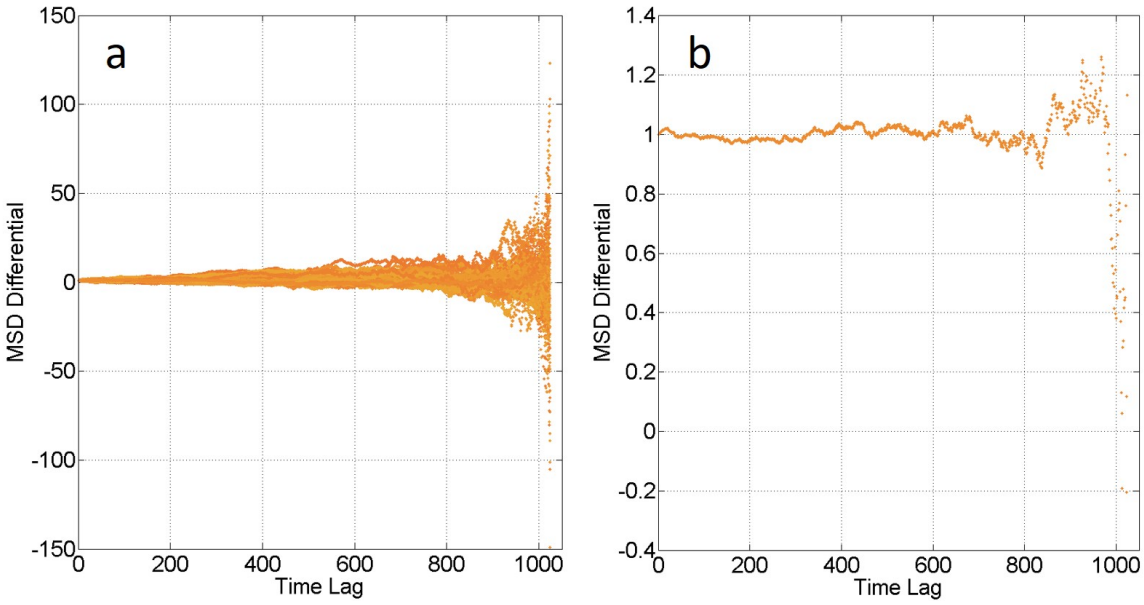

Figure B.4: a. The differentials of MSD vs. lag (numerical derivative–$(y_{i+1}y_i)$ / $(x_{i+1}x_i)$, where y is MSD and x is lag.) of MSD vs. lag trajectories. Differentials are a rough measure of local slope. a. Differentials of 100 MSD vs. lag trajectories. Although individual MSD trajectories can vary widely in slope, the population of curves is centered on a differential of 1. The amount of variation increases with increasing lag. b. Differentials of the mean of 1024 MSD trajectories (all 1024 MSD trajectories were averaged first, then the differentials of that averaged curve were calculated.) Differentials of mean MSD are close to 1, but vary more as lag increases.

Bibliography

[1] K. Luby-Phelps, *Cytoarchitecture and physical properties of cytoplasm: volume, viscosity, diffusion, intracellular surface area*, *International review of cytology* **192** (1999) 189–221.

[2] T. Guérin, J. Prost, P. Martin, and J.-F. Joanny, *Coordination and collective properties of molecular motors: theory*, *Current Opinion in Cell Biology* **22** (Feb., 2010) 14–20.

[3] C. Leduc, O. Campàs, J.-F. Joanny, J. Prost, and P. Bassereau, *Mechanism of membrane nanotube formation by molecular motors*, *Biochimica et Biophysica Acta (BBA) - Biomembranes* **1798** (July, 2010) 1418–1426.

[4] G. van Meer, D. R. Voelker, and G. W. Feigenson, *Membrane lipids: where they are and how they behave*, *Nature Reviews Molecular Cell Biology* **9** (Feb., 2008) 112–124.

[5] G. Morfini, G. Pigino, U. Beffert, J. Busciglio, and S. T. Brady, *Fast axonal transport misregulation and Alzheimer's Disease*, *NeuroMolecular Medicine* **2** (Oct., 2002) 89–99.

[6] G. B. Stokin and L. S. B. Goldstein, *Axonal Transport and Alzheimer's Disease*, *Annual Review of Biochemistry* **75** (2006), no. 1 607–627.

[7] E. Chevalier-Larsen and E. L. F. Holzbaur, *Axonal transport and neurodegenerative disease*, *Biochimica et Biophysica Acta (BBA) - Molecular Basis of Disease* **1762** (Nov., 2006) 1094–1108.

[8] K. R. Brunden, C. Ballatore, V. M.-Y. Lee, A. B. Smith, and J. Q. Trojanowski, *Brain-penetrant microtubule-stabilizing compounds as potential therapeutic agents for tauopathies*, *Biochemical Society Transactions* **40** (Aug., 2012) 661–666.

[9] O. A. Shemesh and M. E. Spira, *Rescue of neurons from undergoing hallmark tau-induced Alzheimer's disease cell pathologies by the antimitotic drug paclitaxel*, *Neurobiology of Disease* **43** (July, 2011) 163–175.

[10] J. L. Ross, M. Y. Ali, and D. M. Warshaw, *Cargo transport: molecular motors navigate a complex cytoskeleton*, *Current Opinion in Cell Biology* **20** (Feb., 2008) 41–47.

[11] S. M. Block, C. L. Asbury, J. W. Shaevitz, and M. J. Lang, *Probing the kinesin reaction cycle with a 2d optical force clamp*, *Proceedings of the National Academy of Sciences* **100** (Mar., 2003) 2351–2356.

[12] A. Yildiz, M. Tomishige, R. D. Vale, and P. R. Selvin, *Kinesin Walks Hand-Over-Hand*, *Science* **303** (Jan., 2004) 676–678.

[13] N. J. Carter and R. A. Cross, *Mechanics of the kinesin step*, *Nature* **435** (May, 2005) 308–312.

[14] K. Visscher, M. J. Schnitzer, and S. M. Block, *Single kinesin molecules studied with a molecular force clamp*, *Nature* **400** (July, 1999) 184–189.

[15] S. S. Rosenfeld, P. M. Fordyce, G. M. Jefferson, P. H. King, and S. M. Block, *Stepping and Stretching HOW KINESIN USES INTERNAL STRAIN TO WALK PROCESSIVELY*, *Journal of Biological Chemistry* **278** (May, 2003) 18550–18556.

[16] S. P. Gilbert, M. L. Moyer, and K. A. Johnson, *Alternating Site Mechanism of the Kinesin ATPase*, *Biochemistry* **37** (Jan., 1998) 792–799.

[17] F. Kozielski, S. Sack, A. Marx, M. Thormählen, E. Schönbrunn, V. Biou, A. Thompson, E. M. Mandelkow, and E. Mandelkow, *The Crystal Structure of Dimeric Kinesin and Implications for Microtubule-Dependent Motility*, *Cell* **91** (Dec., 1997) 985–994.

[18] E. P. Sablin, F. J. Kull, R. Cooke, R. D. Vale, and R. J. Fletterick, *Crystal structure of the motor domain of the kinesin-related motor ncd*, *Nature; London* **380** (Apr., 1996) 555–9.

[19] C. J. Lawrence, R. K. Dawe, K. R. Christie, D. W. Cleveland, S. C. Dawson, S. A. Endow, L. S. B. Goldstein, H. V. Goodson, N. Hirokawa, J. Howard, R. L. Malmberg, J. R. McIntosh, H. Miki, T. J. Mitchison, Y. Okada, A. S. N. Reddy, W. M. Saxton, M. Schliwa, J. M. Scholey, R. D. Vale, C. E. Walczak, and L. Wordeman, *A standardized kinesin nomenclature*, *The Journal of Cell Biology* **167** (Oct., 2004) 19–22.

[20] R. D. Vale, T. S. Reese, and M. P. Sheetz, *Identification of a novel force-generating protein, kinesin, involved in microtubule-based motility*, *Cell* **42** (Aug., 1985) 39–50.

[21] K. Svoboda, C. F. Schmidt, B. J. Schnapp, and S. M. Block, *Direct observation of kinesin stepping by optical trapping interferometry*, *Nature* **365** (1993), no. 6448 721–727.

[22] J. Howard and R. L. Clark, *Mechanics of motor proteins and the cytoskeleton*, *Applied Mechanics Reviews* **55** (2002) 39.

[23] D. D. Hackney and M. F. Stock, *Kinesin's IAK tail domain inhibits initial microtubule-stimulated ADP release*, *Nature Cell Biology* **2** (2000), no. 5 257–260.

[24] D. L. Coy, W. O. Hancock, M. Wagenbach, and J. Howard, *Kinesin's tail domain is an inhibitory regulator of the motor domain*, *Nature Cell Biology* **1** (1999), no. 5 288–292.

[25] K. Svoboda and S. M. Block, *Force and velocity measured for single kinesin molecules*, *Cell* **77** (June, 1994) 773–784.

[26] O. Campàs, C. Leduc, P. Bassereau, J. Casademunt, J.-F. Joanny, and J. Prost, *Coordination of Kinesin Motors Pulling on Fluid Membranes*, *Biophysical Journal* **94** (June, 2008) 5009–5017.

[27] G. Koster, M. VanDuijn, B. Hofs, and M. Dogterom, *Membrane tube formation from giant vesicles by dynamic association of motor proteins*, *Proceedings of the National Academy of Sciences* **100** (Dec., 2003) 15583–15588.

[28] P. A. Sims and X. S. Xie, *Probing Dynein and Kinesin Stepping with Mechanical Manipulation in a Living Cell*, *ChemPhysChem* **10** (July, 2009) 1511–1516.

[29] M. Vershinin, B. C. Carter, D. S. Razafsky, S. J. King, and S. P. Gross, *Multiple-motor based transport and its regulation by Tau*, *Proceedings of the National Academy of Sciences* **104** (Jan., 2007) 87–92.

[30] S. P. Gross, M. Vershinin, and G. T. Shubeita, *Cargo Transport: Two Motors Are Sometimes Better Than One*, *Current Biology* **17** (June, 2007) R478–R486.

[31] G. T. Shubeita, S. L. Tran, J. Xu, M. Vershinin, S. Cermelli, S. L. Cotton, M. A. Welte, and S. P. Gross, *Consequences of Motor Copy Number on the Intracellular Transport of Kinesin-1-Driven Lipid Droplets*, *Cell* **135** (Dec., 2008) 1098–1107.

[32] S. P. Gross, M. A. Welte, S. M. Block, and E. F. Wieschaus, *Dynein-Mediated Cargo Transport in Vivo: A Switch Controls Travel Distance*, *The Journal of Cell Biology* **148** (Mar., 2000) 945–956.

[33] S. M. Block, L. S. B. Goldstein, and B. J. Schnapp, *Bead movement by single kinesin molecules studied with optical tweezers*, *Nature* **348** (Nov., 1990) 348–352.

[34] R. Lipowsky and E. Sackmann, *Structure and Dynamics of Membranes: I. From Cells to Vesicles/II. Generic and Specific Interactions*. Elsevier, Jan., 1995.

[35] J. Israelachvili, *Intermolecular and Surface Forces - 3rd Edition*. Academic Press, May, 2011.

[36] O. Campàs, Y. Kafri, K. B. Zeldovich, J. Casademunt, and J.-F. Joanny, *Collective Dynamics of Interacting Molecular Motors*, *Physical Review Letters* **97** (July, 2006) 038101.

[37] S. Klumpp and R. Lipowsky, *Cooperative cargo transport by several molecular motors*, *Proceedings of the National Academy of Sciences of the United States of America* **102** (Nov., 2005) 17284–17289.

[38] J. L. Ross, H. Shuman, E. L. F. Holzbaur, and Y. E. Goldman, *Kinesin and Dynein-Dynactin at Intersecting Microtubules: Motor Density Affects Dynein Function*, *Biophysical Journal* **94** (Apr., 2008) 3115–3125.

[39] M. H. Hinrichs, A. Jalal, B. Brenner, E. Mandelkow, S. Kumar, and T. Scholz, *Tau Protein Diffuses along the Microtubule Lattice*, *Journal of Biological Chemistry* **287** (Nov., 2012) 38559–38568.

[40] B. J. Lopez and M. T. Valentine, *The +TIP coordinating protein EB1 is highly dynamic and diffusive on microtubules, sensitive to GTP analog, ionic strength, and EB1 concentration*, *Cytoskeleton* **73** (Jan., 2016) 23–34.

[41] D. Axelrod, *Chapter 7 Total Internal Reflection Fluorescence Microscopy*, in *Methods in Cell Biology*, vol. 89 of *Biophysical Tools for Biologists, Volume Two: In Vivo Techniques*, pp. 169–221. Academic Press, Jan., 2008. DOI: 10.1016/S0091-679X(08)00607-9.

[42] A. Yildiz and R. D. Vale, *Total Internal Reflection Fluorescence Microscopy*, *Cold Spring Harbor Protocols* **2015** (Sept., 2015) pdb.top086348.

[43] "iXon EMCCD Cameras | Andor, http://www.andor.com/cameras/ixon-emccd-camera-series."

[44] W. J. Greenleaf, M. T. Woodside, E. A. Abbondanzieri, and S. M. Block, *Passive All-Optical Force Clamp for High-Resolution Laser Trapping*, *Physical Review Letters* **95** (Nov., 2005) 208102.

[45] S. B. Smith, Y. Cui, and C. Bustamante, *Overstretching B-DNA: The Elastic Response of Individual Double-Stranded and Single-Stranded DNA Molecules*, *Science* **271** (Feb., 1996) 795–799.

[46] A. Ashkin and J. M. Dziedzic, *Optical trapping and manipulation of viruses and bacteria*, *Science* **235** (1987), no. 4795 1517–1520.

[47] K. C. Neuman and S. M. Block, *Optical trapping*, *The Review of scientific instruments* **75** (Sept., 2004) 2787–2809.

[48] A. Ashkin, J. M. Dziedzic, J. E. Bjorkholm, and S. Chu, *Observation of a single-beam gradient force optical trap for dielectric particles*, *Optics letters* **11** (1986), no. 5 288–290.

[49] R. M. Simmons, J. T. Finer, S. Chu, and J. A. Spudich, *Quantitative measurements of force and displacement using an optical trap*, *Biophysical Journal* **70** (Apr., 1996) 1813–1822.

[50] M. C. Williams, *Optical tweezers: measuring piconewton forces*, *Biophysics Textbook Online: http://www. biophysics. org/btol* (2002).

[51] K. C. Neuman and A. Nagy, *Single-molecule force spectroscopy: optical tweezers, magnetic tweezers and atomic force microscopy*, *Nature methods* **5** (2008), no. 6 491–505.

[52] *Low Pass Filter - Passive RC Filter Tutorial http://www.electronics-tutorials.ws/filter/filter_2.html*, Aug., 2013.

[53] D. Jovanovic, R. Radovic, L. Mares, M. Stankovic, and B. Markovic, *Nickel hydrogenation catalyst for tallow hydrogenation and for the selective hydrogenation of sunflower seed oil and soybean oil*, *Catalysis Today* **43** (Aug., 1998) 21–28.

[54] P. Schiebener, J. Straub, J. M. H. L. Sengers, and J. S. Gallagher, *Refractive index of water and steam as function of wavelength, temperature and density*, *Journal of Physical and Chemical Reference Data* **19** (May, 1990) 677–717.

[55] O. Campàs, T. Mammoto, S. Hasso, R. A. Sperling, D. O'Connell, A. G. Bischof, R. Maas, D. A. Weitz, L. Mahadevan, and D. E. Ingber, *Quantifying cell-generated mechanical forces within living embryonic tissues*, *Nature Methods* **11** (Feb., 2014) 183–189.

[56] M. Negishi, H. Seto, M. Hase, and K. Yoshikawa, *How Does the Mobility of Phospholipid Molecules at a Water/Oil Interface Reflect the Viscosity of the Surrounding Oil?*, *Langmuir* **24** (Aug., 2008) 8431–8434.

[57] B. Esteban, J.-R. Riba, G. Baquero, A. Rius, and R. Puig, *Temperature dependence of density and viscosity of vegetable oils*, *Biomass and Bioenergy* **42** (July, 2012) 164–171.

[58] L. M. Diamante and T. Lan, *Absolute Viscosities of Vegetable Oils at Different Temperatures and Shear Rate Range of 64.5 to 4835 s-1*, 2014. DOI: 10.1155/2014/234583.

[59] I. Niţă, A. Neagu, S. Geacai, A. Dumitru, and A. Sterpu, *Study of the behavior of some vegetable oils during the thermal treatment*, *Ovidius University Annals of Chemistry* **21** (2010), no. 1 5–8.

[60] Sigma-Aldrich, *Product Specification for Mineral oil BioReagent, for molecular biology, light oil, Product Number: M5804, CAS Number: 8042-47-5*, 2010.

[61] A. O. fisher scientific, "Mineral oil, pure, ACROS Organics - Chemicals, https://www.fishersci.com/shop/products/mineral-oil-pure-acros-organics-4/p-4323678."

[62] Sigma-Aldrich, "Mineral Oil PX0045, white, CAS Number 8042-47-5, https://www.sigmaaldrich.com/catalog/product/mm/px0045?lang=en&region=US."

[63] Sigma-Aldrich, "Mineral oil 330760, heavy, CAS Number 8042-47-5, https://www.sigmaaldrich.com/catalog/product/sial/330760?lang=en&region=US."

[64] A. O. fisher scientific, "Silicone oil, for melting point and boiling point apparatuses, ACROS Organics, https://www.fishersci.com/shop/products/silicone-oil-melting-point-boiling-point-apparatuses-acros-organics-3/p-3777044#?keyword=63148-62-9."

[65] A. O. fisher scientific, "Silicone oil, high temperature, ACROS Organics, https://www.fishersci.com/shop/products/silicone-oil-high-temperature-acros-organics-3/ac174661000."

[66] A. Organics, *Acros Organics Certificate of Analysis, Catalog Number 17466, Lot Number A0385668, CAS No 63148-58-3*, 2017.

[67] Sigma-Aldrich, "Silicone oil Product Comparison Guide, Sigma-Aldrich, https://www.sigmaaldrich.com/catalog/substance/siliconeoil1234563148629 11?lang=en&region=US&attrlist=Density|Refractive%20index|Viscosity."

[68] P. M. 3M, *Fluorinert Electronic Liquid FC-70 Product Information*, 2000.

[69] 3M, *Fluorinert Electronic Liquid FC-3283 Product Information, https://multimedia.3m.com/mws/media/64886o/fluorinert-electronic-liquid-fc-3283.pdf*, 2001.

[70] 3M, *Fluorinert Electronic Liquid FC-40 Product Information, https://multimedia.3m.com/mws/media/64888o/fluorinert-electronic-liquid-fc-40.pdf*, 2010.

[71] "PDMS membrane: thickness of a spin coated PDMS layer http://www.elveflow.com/microfluidic-tutorials/soft-lithography-reviews-and-tutorials/introduction-in-soft-lithography/pdms-membrane-thickness-of-a-spin-coated-pdms-layer/."

[72] C.-T. Hsu, C.-H. Chang, and S.-Y. Lin, *Comments on the Adsorption Isotherm and Determination of Adsorption Kinetics*, *Langmuir* **13** (Nov., 1997) 6204–6210.

[73] F. M. Menger and S. A. A. Rizvi, *Relationship between Surface Tension and Surface Coverage*, *Langmuir* **27** (Dec., 2011) 13975–13977.

[74] J. D. Berry, M. J. Neeson, R. R. Dagastine, D. Y. C. Chan, and R. F. Tabor, *Measurement of surface and interfacial tension using pendant drop tensiometry*, *Journal of Colloid and Interface Science* **454** (Sept., 2015) 226–237.

[75] J. M. Crane and L. K. Tamm, *Role of Cholesterol in the Formation and Nature of Lipid Rafts in Planar and Spherical Model Membranes*, *Biophysical Journal* **86** (Jan., 2004) 2965–2979.

[76] A. A. Bui, A. B. Stilgoe, T. A. Nieminen, and H. Rubinsztein-Dunlop, *Calibration of nonspherical particles in optical tweezers using only position measurement*, *Optics letters* **38** (2013), no. 8 1244–1246.

[77] M. Jahnel, M. Behrndt, A. Jannasch, E. Schäffer, and S. W. Grill, *Measuring the complete force field of an optical trap*, *Optics Letters* **36** (Mar., 2011) 1260.

[78] J. C. Wilcox, B. J. Lopez, O. Campàs, and M. T. Valentine, *Improved calibration of the nonlinear regime of a single-beam gradient optical trap*, *Optics Letters* **41** (May, 2016) 2386–2389.

[79] Z. Liu, J. L. Tan, D. M. Cohen, M. T. Yang, N. J. Sniadecki, S. A. Ruiz, C. M. Nelson, and C. S. Chen, *Mechanical tugging force regulates the size of cell–cell junctions*, *Proceedings of the National Academy of Sciences* **107** (June, 2010) 9944–9949.

[80] Y. Yang, M. Bai, W. S. Klug, A. J. Levine, and M. T. Valentine, *Microrheology of highly crosslinked microtubule networks is dominated by force-induced crosslinker unbinding*, *Soft Matter* **9** (2013), no. 2 383–393.

[81] A. Jannasch, A. F. Demirörs, P. D. J. van Oostrum, A. van Blaaderen, and E. Schäffer, *Nanonewton optical force trap employing anti-reflection coated, high-refractive-index titania microspheres*, *Nature Photonics* **6** (July, 2012) 469–473.

[82] D. C. Appleyard, K. Y. Vandermeulen, H. Lee, and M. J. Lang, *Optical trapping for undergraduates*, *American Journal of Physics* **75** (Jan., 2007) 5–14.

[83] M. J. Lang, C. L. Asbury, J. W. Shaevitz, and S. M. Block, *An Automated Two-Dimensional Optical Force Clamp for Single Molecule Studies*, *Biophysical Journal* **83** (July, 2002) 491–501.

[84] B. M. Lansdorp and O. A. Saleh, *Power spectrum and Allan variance methods for calibrating single-molecule video-tracking instruments*, *Review of Scientific Instruments* **83** (Feb., 2012) 025115.

[85] E. A. Abbondanzieri, J. W. Shaevitz, and S. M. Block, *Picocalorimetry of Transcription by RNA Polymerase*, *Biophysical Journal* **89** (Dec., 2005) L61–L63.

[86] T. Tlusty, A. Meller, and R. Bar-Ziv, *Optical gradient forces of strongly localized fields*, *Physical review letters* **81** (1998), no. 8 1738.

[87] P. Bartlett and S. Henderson, *Three-dimensional force calibration of a single-beam optical gradient trap*, *Journal of Physics: Condensed Matter* **14** (2002), no. 33 7757.

[88] M. Y. Ali, E. B. Krementsova, G. G. Kennedy, R. Mahaffy, T. D. Pollard, K. M. Trybus, and D. M. Warshaw, *Myosin Va maneuvers through actin intersections and diffuses along microtubules*, *Proceedings of the National Academy of Sciences of the United States of America* **104** (Mar., 2007) 4332–4336.

[89] I. Minoura, E. Katayama, K. Sekimoto, and E. Muto, *One-Dimensional Brownian Motion of Charged Nanoparticles along Microtubules: A Model System for Weak Binding Interactions*, *Biophysical Journal* **98** (Apr., 2010) 1589–1597.

[90] D. P. McVicker, G. J. Hoeprich, A. R. Thompson, and C. L. Berger, *Tau Interconverts Between Diffusive and Stable Populations on the Microtubule Surface in an Isoform and Lattice Specific Manner*, *Cytoskeleton (Hoboken, N.J.)* **71** (Mar., 2014) 184–194.

[91] E. L. Elson, *Fluorescence correlation spectroscopy and photobleaching recovery*, *Annual review of physical chemistry* **36** (1985), no. 1 379–406.

[92] H. Qian, M. P. Sheetz, and E. L. Elson, *Single particle tracking. Analysis of diffusion and flow in two-dimensional systems.*, *Biophysical Journal* **60** (Oct., 1991) 910–921.

[93] N. O. Petersen, *Scanning fluorescence correlation spectroscopy. I. Theory and simulation of aggregation measurements*, *Biophysical Journal* **49** (Apr., 1986) 809–815.

[94] H. Qian, *On the statistics of fluorescence correlation spectroscopy*, *Biophysical Chemistry* **38** (Oct., 1990) 49–57.

[95] M. J. Saxton, *Single-particle tracking: the distribution of diffusion coefficients.*, *Biophysical Journal* **72** (Apr., 1997) 1744–1753.

[96] W. F. Wade, J. H. Freed, and M. Edidin, *Translational diffusion of class II major histocompatibility complex molecules is constrained by their cytoplasmic domains.*, *The Journal of Cell Biology* **109** (Dec., 1989) 3325–3331.

[97] M. T. Valentine, P. D. Kaplan, D. Thota, J. C. Crocker, T. Gisler, R. K. Prud'homme, M. Beck, and D. A. Weitz, *Investigating the microenvironments of inhomogeneous soft materials with multiple particle tracking*, *Physical Review E* **64** (Nov., 2001) 061506.

[98] X. Michalet, *Mean Square Displacement Analysis of Single-Particle Trajectories with Localization Error: Brownian Motion in Isotropic Medium*, *Physical review. E, Statistical, nonlinear, and soft matter physics* **82** (Oct., 2010) 041914.

[99] N. Monnier, S.-M. Guo, M. Mori, J. He, P. Lénárt, and M. Bathe, *Bayesian Approach to MSD-Based Analysis of Particle Motion in Live Cells*, *Biophysical Journal* **103** (Aug., 2012) 616–626.